

UC Berkeley

UC Berkeley Electronic Theses and Dissertations

Title

Imaging and Control of Defects and Electronic Transport Pathways in Semiconductor Nanomaterials

Permalink

<https://escholarship.org/uc/item/5xk7119t>

Author

Zhang, Yingjie

Publication Date

2015

Peer reviewed|Thesis/dissertation

Imaging and Control of Defects and Electronic Transport Pathways in Semiconductor
Nanomaterials

By

Yingjie Zhang

A dissertation submitted in partial satisfaction of the

requirements for the degree of

Doctor of Philosophy

in

Applied Science and Technology

in the

Graduate Division

of the

University of California, Berkeley

Committee in charge:

Professor Miquel B. Salmeron, Co-Chair

Professor A. Paul Alivisatos, Co-Chair

Associate Professor Junqiao Wu

Professor Michael F. Crommie

Summer 2015

Abstract

Imaging and Control of Defects and Electronic Transport Pathways in Semiconductor Nanomaterials

by

Yingjie Zhang

Doctor of Philosophy in Applied Science and Technology

University of California, Berkeley

Professor Miquel B. Salmeron, Co-Chair

Professor A. Paul Alivisatos, Co-Chair

Solution processed materials, such as organic molecules and semiconductor quantum dots (QDs), have been widely explored for large area electronics and optoelectronics applications, such as field effect transistors (FETs), solar cells, photodetectors, LEDs, etc. Compared to the traditional crystalline/polycrystalline semiconductors (Si, GaAs, etc.), these novel devices have the advantage of being low-cost and flexible. However, a major limitation in device performance is the significant amount of unintentional defects that are believed to hinder charge transport and induce electron-hole recombination, detrimental to optoelectronic devices. The chemical origin of these defects is largely unknown, and is difficult to characterize. One major goal of my PhD research is to investigate the nature of the defects in solution processed semiconductor materials, and to control the defects and doping for improving the large area electronic/optoelectronic device performance.

Semiconductor QDs can be viewed as “artificial atoms” that can form “artificial solids” when assembled together. By controlling the QD size, shape, surface chemistry, and the way QDs are connected or fused together, we are able to design the artificial QD solids to have the desired electronic functionalities. These materials are typically viewed in a coarse-grained way as electronically homogeneous, for the ease of understanding the electrical properties using traditional semiconductor theory. However, in the presence of various possible defects, the electronic structure and charge distribution can be inherently heterogeneous, which may have a dominant effect on the transport properties. Therefore, the other important goal in this thesis is to microscopically image the charge transport pathways, and to control them for device applications.

Our technical approach is using scanning probe-based microscopy and spectroscopy, to characterize the materials and devices. With the obtained novel mechanisms, we go back to engineer the properties to achieve high efficiency devices. Specifically, we developed a technique to use Kelvin probe force microscopy to probe the surface potential of an FET channel, from which the density of in-gap states (IGS, electronic states inside the band gap) are extracted. Using this technique and other complimentary characterization tools, we probed the IGS in a thiophene-based organic FET and PbS quantum dots, and attribute their origin to hydroxyl and molecular oxygen species, respectively. We also imaged the charge percolation pathways of PbS

QD solids and CdTe polycrystalline films made by sintering CdTe nanocrystals, and found novel impurity conduction and grain boundary assisted conduction mechanisms. Mesoscale engineering of percolation pathways further lead to ultra-high gain CdTe photoconductors, where the high gain comes from the heterogeneous dopant distribution and high mobility in the grain boundary.

Acknowledgements

First of all, I would like to thank my co-advisors Prof. Miquel Salmeron and Prof. Paul Alivisatos. I am very grateful to Miquel who showed me how materials properties can be understood from the behavior of the individual constituent atoms. He provided me with a special pair of glasses to explore this world, to see how atoms interact with each other and arrange themselves on surfaces and interfaces, and how electrons interact with vacancies, impurities, surfaces, and interfaces while meandering in a disordered sea of atoms. I also owe a great thanks to Paul, who showed me how hundreds to thousands of atoms can happily pack and dance together in the form of nanocrystals, and how these nanoscale building blocks can assemble together forming functional artificial solids. With my special glasses I saw the surface structure of nanocrystals, the way charge carriers interact with surface defects, the pathways of charge percolation in an array of nanocrystals, and eventually the magic of converting one photon to billions of electrons in an artificial solid. Both advisors have always been inspiring and can always see the big picture, guiding me towards unexplored areas where we eventually found rich science. As I went deeper and deeper into projects, they also helped me tackle detailed challenges with their broad knowledge.

I took the journey of challenging independent projects beginning from the first year of my PhD study. Miquel had been very patient and encouraging, and guided me through the most difficult times in the first two years, when I was working mostly on instrumentation. After those two years of “thermal fluctuation” around zero, I began the “exponential growth”, which has not stopped even now.

I would like to thank members and visitors in the Salmeron group who provided me with enormous help, especially in the early stage of my PhD. Allard Katan, Carlos Escudero, Florent Martin, Xiaofeng Feng and Wei Bao helped me learned various kinds of scanning probe techniques in my first year. I want to especially thank Prof. Jaime Colchero, who visited the group several times and showed me everything about atomic force microscopy and electrostatic force microscopy. Sara Barja and Leonid Lichtenstein offered help with scanning tunneling microscopy measurements.

I also need to thank many members in the Alivisatos group. Jesse Engel and Marcus Scheele introduced me to the field of quantum dot solids, and helped me with field effect transistor measurements. Danny Hellebusch, Noah Bronstein, Qian Chen, Matt Lucas, Xingchen Ye, Jianbo Gao, Tae-Gon Kim, and Myounghwan Oh helped a lot with nanocrystal synthesis and/or various inspiring discussions. Noah also provided enormous help on optoelectronic measurements. Project discussions in the Alivisatos group meetings are always fruitful and illuminating.

I sincerely thank all the collaborators who contributed to my PhD work. Theory collaborators Danylo Zhrebetsky and Dr. Lin-Wang Wang offered significant help on several projects. Andrew Pun, David Hanifi, Bo He, Dr. Yi Liu, Peter Bai, Prof. Ting Xu provided organic molecules and engaged in various discussions. Prof. Olivier Pluchery initiated an exciting collaboration project on imaging and manipulating charges in single nanoparticles.

I appreciate the tremendous help from many people in the Molecular Foundry, including Dominik Ziegler, Paul Ashby, Ed Wong, D. Frank Ogletree, Virginia Altoe, Alex Weber-Bargioni, Adam Schwartzberg, Jim Schuck, Deirdre Olynick, Stefano Cabrini, Shaul Aloni, and Teresa Chen.

I want to thank all my family members for their support of me pursuing my PhD degree and an academic career. Words cannot express how grateful I am to my beloved wife, Qian Chen, who always appreciated the way I do science, who made me confident to keep pursuing a career in academia at times when I was lost, who motivated me by her own dedication to science, and who gave birth to our little angel, Angeline Zhang, during my graduate study.

Table of Contents

Chapter 1. Introduction

1.1 Colloidal Quantum Dot Solids.....	1
1.2 Analysis of Semiconductor Defect States.....	2
1.3 Imaging the Charge Transport Pathways.....	4
1.4 Organization of Thesis.....	8

Chapter 2. Atomic Ligand Passivation Structure of PbS Nanocrystals

2.1 Abstract.....	10
2.2 Atomic Model of PbS Nanocrystal Surface.....	10
2.3 Experimental Evidence of Nanocrystal Surface Hydroxylation.....	17
2.4 Conclusion.....	18

Chapter 3. Measuring the Charge State of Single Nanoparticles

3.1 Abstract.....	21
3.2 Work Function Measurement of Single Au Nanoparticles.....	21
3.3 Mechanism of Charge State Controlled Work Function.....	24
3.4 Chemical Sensing via Work Function Measurements.....	25
3.5 Conclusion.....	27

Chapter 4. Organic-Inorganic Interfacial Charge Trapping States

4.1 Abstract.....	29
4.2 Introduction.....	29
4.3 Imaging Charge Transport Pathways in Semiconductor Organic Monolayers.....	30
4.4 Charge Trapping States Probed by Surface Potential Spectroscopy.....	33
4.5 Time-Resolved Surface Potential Spectroscopy.....	35
4.6 Conclusion.....	38
4.7 Methods Summary.....	38

Chapter 5. Atomic Insight of Defects in PbS Nanocrystals

5.1 Abstract.....	42
5.2 Introduction.....	42
5.3 Experimental Observation of In-Gap States.....	43
5.4 Theoretical calculations on in-gap states.....	47
5.5 Spectroscopic evidence and further theoretical support on the origin of IGS.....	52
5.6 Discussion and Conclusion.....	55

5.7 Methods Summary.....	56
Chapter 6. Imaging Charge Percolation Pathways in Quantum Dot Solids	
6.1 Abstract.....	61
6.2 Introduction.....	61
6.3 Direct Imaging of Charge Transport in PbS Quantum Dots.....	62
6.4 In-Gap States and Charge Percolation Mechanism.....	64
6.5 Conduction Channel Switching and Intrinsic Quantum Dots.....	66
6.6 Discussion and Conclusion.....	69
Chapter 7. Time-Resolved Local Probe of Carrier Trapping Dynamics	
7.1 Abstract.....	72
7.2 Introduction.....	72
7.3 Experimental Setup.....	73
7.4 Charge Trapping Dynamics upon Injection.....	75
7.5 Charge Transport Dynamics upon Injection.....	78
7.6 Discussion and Conclusion.....	81
Chapter 8. Ultrasensitive Photodetectors Harnessing Defect Conduction	
8.1 Abstract.....	87
8.2 Device Fabrication, Operation Mechanism, and Performance.....	87
Chapter 9. Summary and Outlook.....	90

Chapter 1: Introduction

“There’s plenty of room at the bottom,” said Richard Feynman in 1959. During the last five decades, the world has seen tremendous scientific and technological advances from micron scale transistors to nano scale materials and all the way to the manipulation of single atoms and chemical bonds. Now that nanoscale fabrication and device integration became a routine task, new challenges emerge. With limited energy and resources throughout the world, low-cost, energy efficient large-area devices are in urgent need. To this end, there has been an emerging interest in bottom-up design of functional materials using nanoscale building blocks. By tuning the way in which the building blocks arrange and interact with each other, these artificial solids can exhibit novel properties not occurring in natural systems, in some cases leading to high-efficiency electronic/optoelectronic devices. Here we will tackle this mesoscale challenge, and systematically explore both the microscopic and mesoscopic behavior of electrons in individual nano building blocks and artificial solids.

1.1 Colloidal Quantum Dot Solids

In the field of semiconductor electronics, solution processing is a new approach with the goal of low-cost manufacturing and flexible device integration for large area applications, such as transistors, solar cells, LEDs and photodetectors. This revolution in electronics dates back to 1977, when Shirakawa, MacDiarmid and Heeger discovered conductive polymers¹. Later on more solution processable materials are discovered, including semiconducting organic small molecules², colloidal quantum dots³, and certain bulk inorganic polycrystals⁴. Among these materials, quantum dots (QDs) have the special feature of “artificial atoms”, where the electronic structure and band gap of individual dots can be tuned by their size and shape. Due to quantum confinement, QDs whose size is smaller than the electron/hole Bohr radius will have a larger bandgap compared to the bulk value, and the electronic states will become discrete, as predicted by the simple particle in a box model in quantum mechanics. The smaller the QD size, the larger the bandgap, and the larger the separation between individual discrete states. The individual semiconductor QDs can be assembled or sintered together to form an artificial QD solid. The electronic transport and optoelectronic properties of these QD solids can be tuned by the way these dots are connected, either with controlled short molecular linkers (typically less than 1 nm), with necked grains, or by sintering to form polycrystalline films (Figure 1.1).

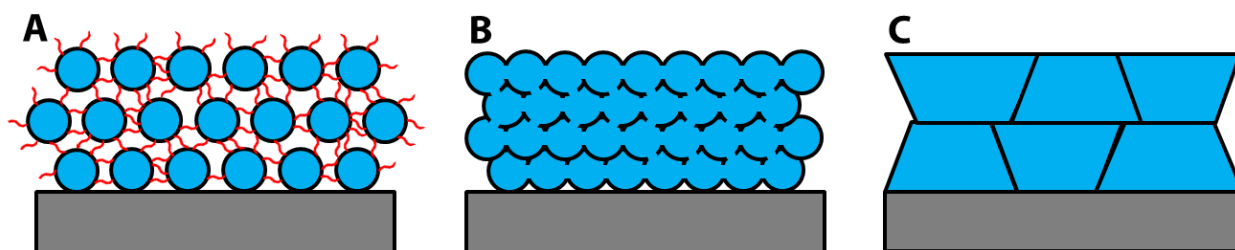


Figure 1.1. Schematic of three types of quantum dot solids. (A) QDs are connected by linker molecules; (B) QDs are touching, partially or fully fused together; (C) QDs are sintered and coalesced to form a polycrystalline film.

Colloidal quantum dots are synthesized from solution, and remain stable in the colloidal form due to the long organic ligands (typically ~ 2 nm) that passivate the QD surface⁵. One way to make a conductive QD solid is to replace these long, insulating ligands with short ones. For Pb chalcogenide (PbS, PbSe) QDs in particular, the original oleic acid or oleylamine ligands can be replaced with 1,2-ethanedithiol (EDT)⁶, 3-mercaptopropionic acid (MPA)⁷, iodide⁸, etc. In these ligand-linked QD solids (Fig. 1.1A), the charge carrier mobility is typically in the range of 10^{-3} – 10^{-1} $\text{cm}^2/(\text{V s})$. In comparison, the carrier mobility in crystalline silicon is $\sim 10^3$ $\text{cm}^2/(\text{V s})$. Despite this low mobility, the solar cells made using PbS QDs have reached a power conversion efficiency up to 8.6%⁸. This apparent controversy may be due to the good surface passivation of the QDs, which enables low carrier recombination rate and long carrier diffusion length⁹.

One way to improve the carrier mobility in QD solids is via mild annealing (usually between 150 °C – 250 °C) that can lead to partially or full necking/fusing. This strategy is widely used in Cd chalcogenide (CdS, CdSe, CdTe) QDs. In fact, one of the earliest work on QD solar cells employed necked CdTe/CdSe heterojunctions³. Later on, new techniques were developed to first exchange the original ligands of the QD to short ligands such as thiocyanate and various molecular metal chalcogenide complexes, and then anneal to enhance the coupling between neighboring QDs. These techniques lead to carrier mobility in the scale of 1–20 $\text{cm}^2/(\text{V s})$ ^{10,11}. Despite the fact that the QDs are touching and likely partially fused together, these high mobility QD solids still retain the quantum confined bandgap, a prominent feature for optoelectronic applications.

Another way to make a high mobility film is to sinter the QDs at higher temperature (250 °C – 400 °C) so that the QDs coalesce and form a polycrystalline film. Although the resulting material shows a bulk band gap and is no longer quantum confined, this bottom-up approach still enables design of the materials properties via the control of the surface ligands of the original QDs. High performance solar cells with a power conversion efficiency of 12.3% have been demonstrated by sintering CdTe QDs into a polycrystalline film¹². Another example is the CdSe films with an electron mobility of 25 $\text{cm}^2/(\text{V s})$ sintered from Cl capped CdSe QDs¹³, where the Cl both passivates the defects and act as a n-type dopant. Most recently, a remarkably high mobility polycrystalline CdSe film was achieved using composition-matched molecular ligands as “solders”¹⁴. The mobility reached 300 $\text{cm}^2/(\text{V s})$, about half of the single crystal value, indicating that the grain boundaries in these films are highly transparent to charge carriers.

These bottom-up tunable properties of quantum dot solids allow us to systematically explore the microscopic surface chemistry and electronic structure of the QD building blocks, the mesoscopic carrier transport pathways, and the overall electronic/optoelectronic device performance. At the mesoscale, new phenomena emerge, new mechanisms come into play, and new devices with high performance are on the way.

1.2 Analysis of Semiconductor Defect States

While controlled doping of impurity atoms into semiconductor crystals opened the way to engineer their charge transport properties, unwanted impurities or defects can hinder transport and limit device performance. The impact of surface impurities on the electronic properties of nanomaterials is more prominent due to the large surface-to-volume ratio and strong quantum

confinement effects. Certain defects/impurities can induce in-gap states (IGS), electronic states inside the band gap. However, until now the nature of the IGS is still unclear.

In order to resolve the energy level of IGS, and to analyze the distribution of IGS on individual QDs, we used scanning probe based spectroscopy techniques. One powerful local probe to measure the electronic density of states (DOS) is scanning tunneling spectroscopy (STS). This technique is based on scanning tunneling microscopy (STM), which enables atomic-resolution imaging¹⁵. A schematic setup of the system is shown in Figure 1.2. This technique was developed in 1980's. The tip is mounted on a piezoelectric scanner, which allows microscopic movements in three dimensions with voltage applied at its electrodes. When a metallic tip approaches a conductive surface at a distance of ~ 1 nm, a tunneling current from the tip to the sample starts to flow. The tip position is controlled using a feedback system to enable a constant tunneling current while the tip scans over the surface. The surface topography image is thus obtained from the trajectory of the tip. Although STM has been used to obtain atomic resolution images on various single crystal surfaces, quantum dots capped with ligands are usually considered "dirty" and present a challenge for STM imaging. As we will see later, in proper imaging conditions single QDs can be resolved, but atomic resolution is hard to achieve.

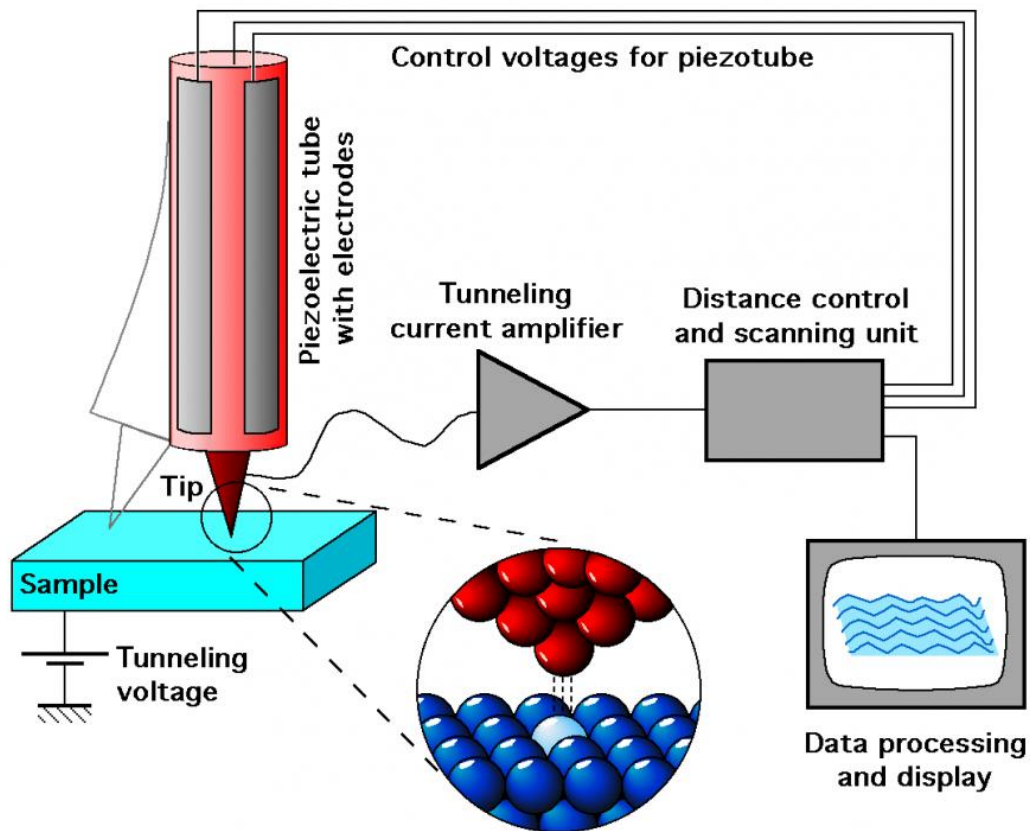


Figure 1.2. Schematic of the scanning tunneling microscopy (STM) setup. Image is adapted from the IAP/TU Wien STM Gallery:

http://www.iap.tuwien.ac.at/www/surface/stm_gallery/stm_schematic

With the tip parked on top of the center of one QD (within tunneling distance), we disconnect the feedback loop (so that the tip-sample distance is kept constant), modulate the sample bias with a small AC voltage and sweep the DC bias. In this way, dI/dV spectra can be obtained using a lock-in amplifier that measures the AC current component. The raw spectrum is a good approximation of the sample DOS at small bias. However, in certain cases at large bias dI/dV can deviate from the DOS due to the dependence of tunneling transmission probability (T) on the sample bias¹⁶. It has been shown that normalizing dI/dV by dividing by I/V can minimize the voltage dependence of T ¹⁶. We have performed this normalization to correct the exponential deviations of dI/dV in some cases.

1.3 Imaging the Charge Transport Pathways

At the mesoscale, new challenges emerge. In these solution processed materials, with quantum dot solids as a model and practical system, various heterogeneity and disorder widely exist, due to a myriad of intentional or unintentional defects and impurities. It is thus desirable to have a tool that can characterize how charge moves in a disordered material. Traditional methods of Transport measurements only deal with current-voltage (I-V) relationships, in a conductor, field effect transistor (FET), or Hall effect device¹⁷. While these bulk measurements reveal the charge carrier conductivity, mobility, and carrier concentration, the microscopic transport mechanisms cannot be directly determined.

We use Kelvin probe force microscopy (KPFM)¹⁸ to image the charge percolation pathways and determine the microscopic charge carrier trapping and hopping mechanism. KPFM measures the local surface potential (V_{st}) or contact potential difference (CPD) whose value (in the unit of volts) is the same as the difference in work function between the tip and the sample (in eV). The mechanism of the measurement is shown in Figure 1.3. For simplification a metallic sample is considered. When the sample and tip are not connected and are far away from each other, their vacuum level (E_{ψ}) aligns but their Fermi level (E_f) may not align due to the work function ($\phi = E_{\psi} - E_f$) difference (Figure 1.3a). When the sample and tip are brought close to each other and are electrically connected, charge flows from one to the other to balance their work function difference. In equilibrium the Fermi level aligns and charge is built up at the surface of the sample and tip, accompanied by an electric field and electrostatic force between them (Figure 1.3b). In KPFM measurements, a DC tip-sample bias (V_{DC}) is applied to nullify the electric field. This DC bias is recorded as the tip-sample CPD:

$$CPD = \frac{\phi_t - \phi_s}{e}, \quad (1.1)$$

where e is the absolute value of the elementary charge.

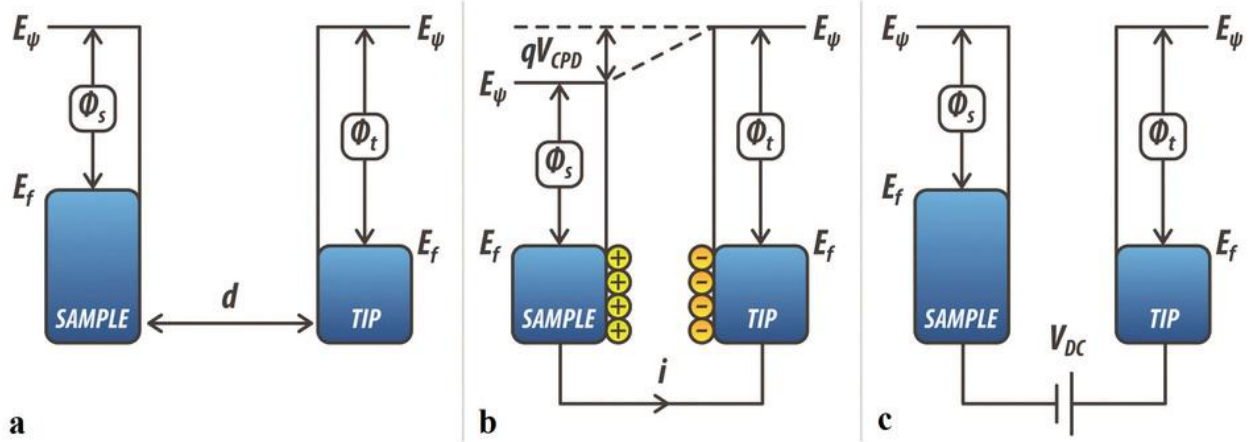


Figure 1.3. General mechanism of KPFM measurements. Image is adapted from *Scientific Reports* 4: 4203 (2014). doi:10.1038/srep04203

The schematic setup of our KPFM is shown in Figure 1.4, which I built during the early stage of my PhD. Based on a commercial atomic force microscope (AFM), we developed additional feedback circuits so that KPFM can be performed. Specifically, we used Agilent 5500 AFM and HF2LI lock-in amplifier (with a built-in PID controller) from Zurich Instruments. We used two types of metallicly coated AFM tips. The first one is Cr/Pt coated AFM tips with 3N/m force constant and 75 kHz resonance frequency, purchased from BudgetSensors; the second one is purchased from Asylum Research (model No. AC240TM, made by Olympus), which is silicon coated with Ti/Pt, with a typical tip radius of ~ 28 nm. The cantilever's spring constant is ~ 2 N/m, and its resonance frequency is ~ 70 kHz. The KPFM measurement was done in a single pass, frequency modulation mode, so that the topography and surface potential can be measured simultaneously. During the non-contact mode AFM imaging, a DC bias (V_{DC}) plus an AC modulation (peak amplitude: $V_{AC} = 2$ V, frequency: $\omega = 2$ kHz) was applied to the AFM tip. The phase shift signal (Δf) from the AFM controller serves as the input to the lock-in amplifier, which extracts the $\omega = 2$ kHz signal (Δf_{ω}). The output is then fed to the PID feedback controller that adjusts the DC bias to nullify Δf_{ω} . The DC tip bias is recorded as the raw CPD / V_{sf} signal. All the scanning probe images are analyzed using WSxM software¹⁹.

Besides the CPD measured from V_{DC} (controlled to nullify Δf_ω), we can simultaneously record the $\Delta f_{2\omega}$ signal. As can be seen from Eq. 1.7, $\Delta f_{2\omega}$ is proportional to $\frac{\partial^2 C}{\partial z^2}$, reflecting the tip-sample capacitance. For semiconductor samples, it is a good measure of mobile carrier density²³.

Our KPFM setup can achieve ~ 10 mV potential resolution and ~ 20 nm spatial resolution, using normal clean tips. As far as we know, this is among the best in all the KPFM systems around the world that operates at 1 atmosphere pressure. By functionalizing the tip with nanoparticles, we can achieve even higher resolution down to ~ 10 nm.

Besides simple, electrically grounded conductive samples, KPFM can be performed on the channel region of a thin film FET, with grounded source & drain and biased gate, to map out the charge percolation pathways and to determine the density of in-gap states. The mechanism of these measurements is shown in Figure 1.5. When a gate bias is applied, charges are injected into the channel region, filling the IGS or band edge states. The higher the DOS, the less the Fermi level moves. In regions where no states are available for charge carriers to be injected, the surface potential will follow the gate bias and change significantly. The exact magnitude of the surface potential change depends on the screening effect of the surrounding conductive areas. If there is no conductive area around, this change is the same as the change of gate bias.

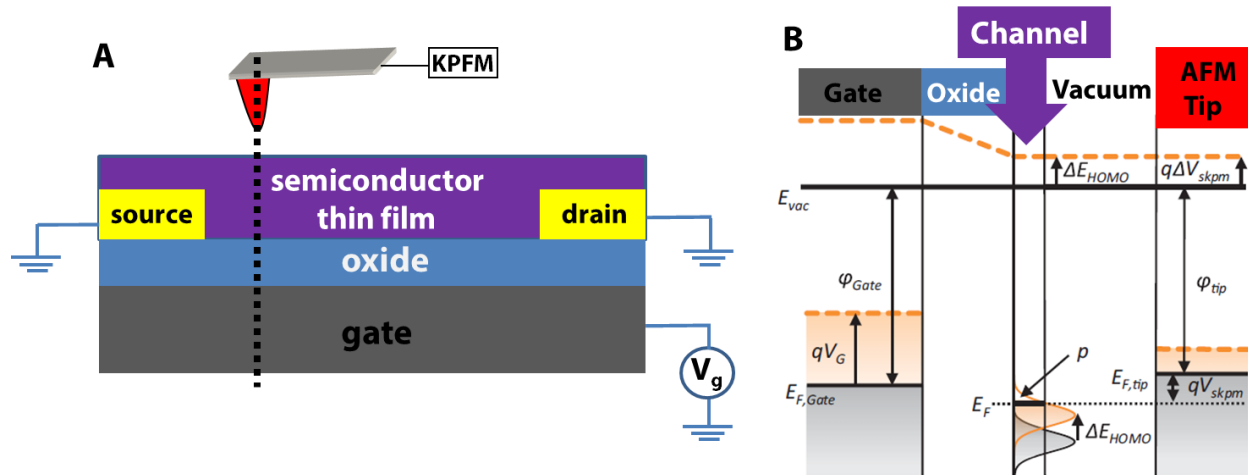


Figure 1.5. (A) Schematic of the KPFM measurement on the channel region of a field effect transistor (FET). (B) The energy level diagram of the cross sectional area of the system, marked by the black dashed line in (A). Part of the contents is reprinted with permission from Ref. 28. Copyright 2012 American Physical Society.

By sweeping the gate bias (V_g) and recording the surface potential (V_{sf}), we can extract the DOS of the IGS. The mechanism has been explained before²⁴⁻²⁸. Previous work have focused on extracting the valence band tail states and deep bandgap states of p-type organic FETs, except our recent work where we explore the QD ambipolar FETs with the goal of obtaining the band tail states and in-gap states²⁴. During the measurements, source and drain electrodes were always grounded. A gate bias was applied to inject charge carriers into the channel. We use a parallel plate capacitor model to extract the local carrier density from the measured V_{sf} :

$$N = \frac{C_{ox}}{t_c e} (V_g - V_{sf}), \quad (1.8)$$

where C_{ox} is the SiO_2 capacitance per unit area, and t_c is the channel thickness. When electrostatic charges are injected into the channel, the work function of the channel changes due to state filling, and the position of the Fermi level with respect to vacuum is $E = eV_{sf}$. The DOS is obtained as:

$$\frac{dN}{dE} = \frac{C_{ox}}{t_c e^2} \left(1 / \frac{dV_{sf}}{dV_g} - 1\right). \quad (1.9)$$

Using the above equation, we can extract the DOS from the V_{sf} - V_g spectrum.

1.4 Organization of Thesis

We will seek to first understand the surface physics and surface chemistry of nanocrystals and organic-inorganic interfaces (Chapter 2–4), and then probe the fundamental defect formation mechanisms and defect-induced in-gap states in QDs (Chapter 5). Furthermore we will study the effect of defects on charge transport in QD solids, highlighting the defect-induced charge percolation phenomena as a novel electronic transport mechanism (Chapter 6,7). We will then present optoelectronic applications utilizing the discovered percolation transport mechanisms (Chapter 8). Finally we will give a summary and outlook (Chapter 9).

References

1. H. Shirakawa, E.J. Louis, A.G. MacDiarmid, C.K. Chiang, and A.J. Heeger, *J. Chem. Soc. Chem. Comm.* 579 (1977).
2. J. R. Heath, *Annu. Rev. Mater. Res.* **39**, 1 (2009).
3. I. Gur, N. A. Fromer, M. L. Geier, and A. P. Alivisatos, *Science* **310**, 462 (2005).
4. D. Liu and T. L. Kelly, *Nature Photon.* **8**, 133 (2014).
5. M.A. Hines and G.D. Scholes, *Adv. Mater.* **15**, 1844 (2003).
6. J. M. Luther, M. Law, Q. Song, C. L. Perkins, M. C. Beard, and A. J. Nozik, *ACS Nano* **2**, 271 (2008).
7. J. Tang, K. W. Kemp, S. Hoogland, K. S. Jeong, H. Liu, L. Levina, M. Furukawa, X. Wang, R. Debnath, D. Cha, K. W. Chou, A. Fischer, A. Amassian, J. B. Asbury, and E. H. Sargent, *Nat. Mater.* **10**, 765 (2011).
8. C. M. Chuang, P. R. Brown, V. Bulović, and M. G. Bawendi, *Nat. Mater.* **13**, 786 (2014).
9. D. Zhitomirsky, O. Voznyy, L. Levina, S. Hoogland, K. W. Kemp, A. H. Ip, S. M. Thon, and E. H. Sargent, *Nat. Commun.* **5**, 3803 (2014).
10. A. T. Fafarman, W. Koh, B. T. Diroll, D. K. Kim, D.-K. Ko, S. J. Oh, X. Ye, V. Doan-Nguyen, M. R. Crump, D. C. Reifsnyder, C. B. Murray, and C. R. Kagan, *J. Am. Chem. Soc.* **133**, 15753 (2011).
11. J.-S. Lee, M. V. Kovalenko, J. Huang, D. S. Chung, and D. V. Talapin, *Nat. Nanotechnol.* **6**, 348 (2011).
12. M. G. Panthani, J. M. Kurley, R. W. Crisp, T. C. Dietz, T. Ezzyat, J. M. Luther, and D. V. Talapin, *Nano Lett.* **14**, 670 (2014).
13. Z. M. Norman, N. C. Anderson, and J. S. Owen, *ACS Nano* **8**, 7513 (2014).
14. D. S. Dolzhenkov, H. Zhang, J. Jang, J. S. Son, M. G. Panthani, T. Shibata, S. Chattopadhyay, and D. V. Talapin, *Science* **347**, 425 (2015).

15. G. Binnig, H. Rohrer, IBM J. Res. Develop. **30**, 355–369 (1986).
16. R. J. Hamers, STM on Semiconductors. In *Scanning Tunneling Microscopy I, Springer Series in Surface Sciences 20*; Güntherodt, H. -J., Wiesendanger, R., Eds.; Springer-Verlag: Berlin, 1992.
17. Y. Liu, J. Tolentino, M. Gibbs, R. Ihly, C. L. Perkins, Y. Liu, N. Crawford, J. C. Hemminger, and M. Law, Nano Lett. **13**, 1578 (2013).
18. M. Nonnenmacher, M. P. O'Boyle, and H. K. Wickramasinghe, Appl. Phys. Lett. **58**, 2921 (1991).
19. I. Horcas, R. Fernandez, J. M. Gomez-Rodriguez, J. Colchero, J. Gomez-Herrero, and A. M. Baro, Rev. Sci. Instrum. **78**, 013705 (2007).
20. J. Colchero, A. Gil, and A. M. Baro, Phys. Rev. B **64**, 245403 (2001).
21. D Ziegler and A Stemmer, Nanotechnology **22**, 075501 (2011).
22. G. Li, B. Mao, F. Lan, and L. Liu, Rev. Sci. Instrum. **83**, 113701 (2012).
23. W. R. Silveira and J. A. Marohn, Phys. Rev. Lett. **93**, 116104 (2004).
24. Y. Zhang, D. Zherebetsky, N. D. Bronstein, S. Barja, L. Lichtenstein, D. Schuppisser, L.-W. Wang, A. P. Alivisatos, and M. Salmeron, Nano Lett. **15**, 3249 (2015).
25. Y. Zhang, D. Ziegler, and M. Salmeron, ACS Nano **7**, 8258 (2013).
26. O. Tal, Y. Rosenwaks, Y. Preezant, N. Tessler, C. K. Chan, and A. Kahn, Phys. Rev. Lett. **95**, 256405 (2005).
27. K. Celebi, P. J. Jadhav, K. M. Milaninia, M. Bora, and M. A. Baldo, Appl. Phys. Lett. **93**, 083308 (2008).
28. W. S. C. Roelofs, S. G. J. Mathijssen, R. A. J. Janssen, D. M. de Leeuw, and M. Kemerink, Phys. Rev. B **85**, 085202 (2012).

Chapter 2: Atomic Ligand Passivation Structure of PbS Nanocrystals

Reproduced in part and adapted with permission from Science 2014, 344 (6190), 1380-1384. Copyright © 2014, American Association for the Advancement of Science.

2.1 Abstract

Controlling the structure of colloidal nanocrystals (NCs) is key to the generation of their complex functionality. This requires an understanding of the NC surface at the atomic level. The structure of colloidal PbS NCs passivated with oleic acid has been studied theoretically and experimentally. We show the existence of surface OH⁻ groups, which play a key role in stabilizing the PbS(111) facets, consistent with X-ray photoelectron spectroscopy as well as other spectroscopic and chemical experiments. The role of water in the synthesis process is also revealed. Our model, along with existing observations of NC surface termination and passivation by ligands, helps to explain and predict the properties of NCs and their assemblies.

The science of nanocrystals has advanced steadily in several directions towards a stage where it is possible to achieve a new atomic level understanding of their structures. A typical colloidal inorganic nanocrystal, such as a semiconductor quantum dot a few nanometers in diameter, is comprised of about as many atoms as a protein, with nearly half of them residing at the surface, which is capped by organic moieties that prevent aggregation and confer solubility. The synthesis of nanocrystals has reached a point where control of their size and shape is now routinely achieved (1-7). While it has been possible to determine the structure of the interior of nanocrystals quite accurately, the structure of their surfaces cannot be obtained from ensemble crystallography. Yet it is the surface structure that controls their growth, solubility, and strongly influences their physical and chemical properties. Here we take advantage of improved insights of the mechanisms of nanocrystal growth (3-7), combined with extensive ab initio total energy calculations, to create a testable model for the atomic structures of the exposed facets of a prototypical nanocrystal. The model makes specific and at first surprising predictions about the nature of the species bound to the surface, which we subsequently verified with a range of experimental probes. The detailed description of the surface atomic structure will not only enhance our understanding of the roles of the surface ligands, it also makes it possible for theoretical predictions of the properties of nanocrystals and their arrays at a new level with realistic descriptions of their surfaces and inter-nanocrystal connections (8-12).

This work focuses on PbS nanocrystals, of current interest as a model system for studies of electrical transport in artificial solids in the limit of extreme quantum confinement (2, 13-16). PbS is ideal for this study because of the high symmetry of its rocksalt structure and its propensity to yield nanocrystals with well-defined (111) and (001) facets (17, 18). Nanocrystals of PbS with controlled size and shape are produced routinely from a PbO lead precursor, bis-trimethyl-silyl sulfur as a sulfur precursor, and oleic acid that binds to exposed Pb atoms to stabilize the surface (1-7). Such nanocrystals form through a complex sequence of events in which kinetic and thermodynamic factors both play a critical role.

2.2 Atomic Model of PbS Nanocrystal Surface

We have performed ab initio electronic structure calculations on relevant sub-systems and reaction steps in the synthetic process, including: studies of the molecular species known to be immediate precursors to atom additions to the nanocrystal; calculations on the possible fate of by-products of the initial decomposition step; as well as nanocrystal-ligand interactions; and ligand-ligand and ligand-solvent interactions. Our calculations are based on density functional theory (DFT) in the generalized gradient approximation (GGA). While van der Waals interactions cannot be described accurately by such method, and entropy contribution in the solvent is too time-consuming to be calculated directly at this stage, we have taken the advantages of likely cancellations of these terms between different systems. Our theoretically derived model has the following features: (1) The Pb:S atomic ratio is roughly 1.2:1 ($\text{Pb}_{\text{excess}}:\text{S}\sim 0.2:1$) for ~ 5 nm NC; (2) The ratio between the number of surface oleate molecules and the number of excess Pb atoms is $\sim 1:1$; (3) The ligands can be more easily removed from the (001) surface; (4) The average (111)/(001) surface to center distance ratio of the truncated octahedral shape is about 0.82:1; (5) OH groups are present on the NC surface. These features are consistent with prior and current experimental studies including Rutherford Backscattering (RBS), transmission electron microscopy (TEM), X-ray photoemission spectroscopy (XPS), sum frequency generation (SFG) spectroscopy, nuclear magnetic resonance (NMR), and Fourier transform infrared spectroscopy (FTIR) (6, 7, 19-22). The presence of hydroxide on the surface is inferred based on the calculation due to the by-products of the precursor decomposition, and verified using XPS and SFG, and the existence of water in the precursor is supported with NMR and FTIR measurements.

The molecular mechanism of the two-step synthesis process of colloidal lead chalcogenide NC was proposed a few years ago (5, 6). In the first step lead oleate precursors are formed by dissolving lead oxide with oleic acid. In the second step the chalcogenide precursors are injected into a heated solution of the lead oleate precursors. One of the by-products in the first step is water. Initially it was proposed that the water molecules will form free water liquid in the precursor solution (5, 6). However, our DFT calculations show that it is energetically more favorable for them to bind to the lead precursor. The binding energy of water to the precursor is calculated to be 0.49 eV per molecule, while the water-water binding energy in liquid water is estimated to be 0.28 eV from our DFT calculations. Therefore, the first reaction step can be written as:



Here we use OAH to denote the oleic acid: $\text{CH}_3(\text{CH}_2)_7\text{CH}=\text{CH}(\text{CH}_2)_7\text{COOH}$, while OA is used to denote oleate ($-\text{COO}^-$ termination). The DFT optimized structure of the $\text{Pb}(\text{OA})_2\cdots\text{H}_2\text{O}$ is shown in Fig. 2.1A. The formation of this complex and the existence of water will play an important role in the subsequent reactions and passivation of the NC.

In the experiment, the reaction of Eq. (2.1) is followed by degassing the product at 110 °C under vacuum for 1 hour. It is thus important to know whether such degassing can remove all the water in the precursor as previously suggested (23). For this purpose, we have used NMR and FTIR to detect water in the precursor, and the possible change after degassing. NMR experiments demonstrate the absence of liquid water, but are unable to distinguish water molecule bound to the $\text{Pb}(\text{OA})_2$ complexes (Fig. 2.1A) (possibly due to coupling of H nuclei with Pb nuclei). Note that the addition of a small amount of $\text{Pb}(\text{OA})_2$ to NMR solvent results in a complete removal of a known peak in the original solvent which corresponds to water in the original solvent,

indicating the hygroscopic nature of the $\text{Pb}(\text{OA})_2$. Using FTIR measurements and deuterated oleic acid ($\text{d}_1\text{-OA}$), we were able to distinguish OH stretching modes associated with water bound to $\text{Pb}(\text{OA})_2$. The $\text{d}_1\text{-OA}$ was prepared so that only the acid proton was exchanged for deuterium. These experiments indicate that a major part of water remains after degassing, which should be sufficient to provide the required 20% of water in Eq.(2.1) for the surface passivation ($\text{Pb}_{\text{excess}}:\text{S}=0.2:1$, one OH per excess Pb, see our model below). Note that the existence of water is also consistent with the observation that the $\text{Pb}(\text{OA})_2$ precursor often forms clusters (24). It is difficult to imagine they will group together without the help of water complexes near the O-Pb-O head groups. As a further demonstration of the role of water, we added acetic anhydride as a drying agent during the reaction of Eq. (2.1) to remove its water (followed by evacuation to remove acetic acid and acetic anhydride). The subsequent formation of PbS NC (following the same procedure as described below) becomes much slower, the NCs are reduced in size from otherwise 8-10 nm (for that particular synthesis condition) to 4 nm, and the particle shapes became rather irregular with many possible (001) surfaces, consistent with our model discussed below. We also note that, there are other ways to prepare $\text{Pb}(\text{OA})_2$ precursor in literature besides Eq.(2.1), but they all provide water in the products although with different sources. For example, Lifshitz and co-workers applied $\text{Pb}(\text{acetate})_2 \cdot 3\text{H}_2\text{O}$ (instead of PbO in Eq.(2.1)) to produce $\text{Pb}(\text{OA})_2$ (25). In this case, the water can come from the original H_2O in the $\text{Pb}(\text{acetate})_2 \cdot 3\text{H}_2\text{O}$.

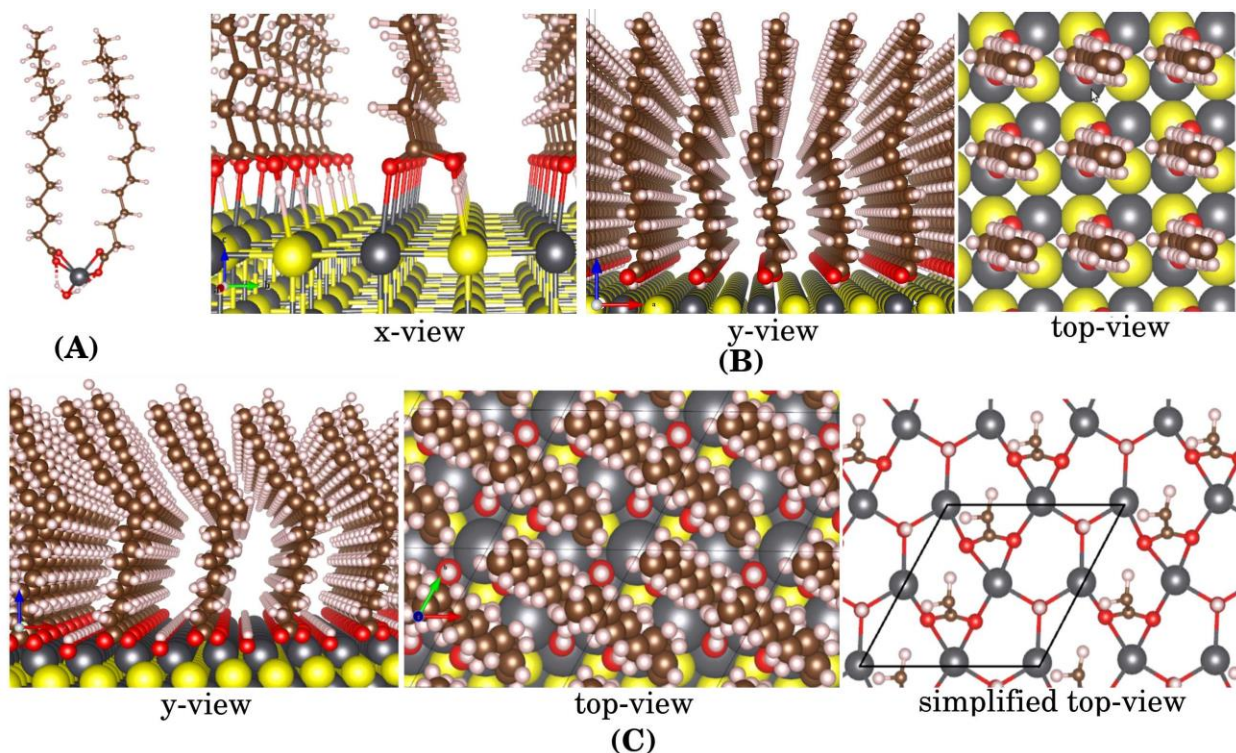
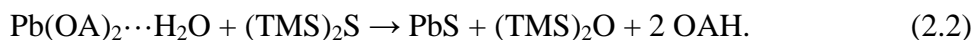


Figure 2.1. Optimized molecular configurations. (A) A water molecule formed during the NC synthesis is bound to the $\text{Pb}(\text{OA})_2$ molecule forming a $\text{Pb}(\text{OA})_2 \cdots \text{H}_2\text{O}$ complex. (B) Relaxed configuration of OAH molecules on the $\text{PbS}(001)$ surface: x-, y- and top-views. (C) Relaxed lowest energy configuration of $-\text{OA}$ and $-\text{OH}$ molecules on the $\text{PbS}(111)$ surface: y- and top-views. On the right a simplified top-view schematic is shown with the tail chains truncated. Pb(gray), S(yellow), O(red), H(white), C(brown).

In the second step, hexamethyldisilathiane ($[\text{TMS}]_2\text{S}$) dissolved in trioctylphosphine (TOP) is injected into the heated $\text{Pb}(\text{OA})_2 \cdots \text{H}_2\text{O}$ precursor solved in octadecene. The reaction can be written as:



The calculated ΔG from Eq.(2.2) is -2.13 eV. In the original article (5, 6), it was suggested that the end result for oleic acid is (oleyl-CO) $_2$ O. It is known and computationally confirmed, that a water molecule will react with (oleyl-CO) $_2$ O to form two equivalents of oleic acid. Thus, when the NC is synthesized, oleic acid, $\text{Pb}(\text{OA})_2 \cdots \text{H}_2\text{O}$ (due to excess $\text{Pb}(\text{OA})_2$ precursor), $(\text{TMS})_2\text{O}$, TOP and octadecene are present in the solution. Due to the excess oleic acid and $\text{Pb}(\text{OA})_2 \cdots \text{H}_2\text{O}$, the final surface is likely to be passivated by oleate. In the following, we will consider passivations on (001) and (111) surfaces separately.

Of all these species our calculation shows that oleic acid has the strongest binding energy to the (001) surface, due to its carboxyl functional group -COOH. Note that the (001) surface bind by an OA^- (12) has a much higher energy in our calculation since the -COO group can always bind with a cation in the solvent to yield a much lower energy. On a $\text{PbS}(001)$ surface, the -COOH groups form bidentate bridges between Pb and S atoms (e.g., with $-\text{C}=\text{O} \cdots \text{Pb}$ and $-\text{COH} \cdots \text{S}$ bonds as shown in Fig. 2.1B). This model contains one oleic acid molecule per two surface PbS -pairs, with one PbS pair bound to one oleic acid, and the other pair unbound. A high-density packing, with one oleic acid per one PbS -pair, is unfavorable due to the steric repulsion between the oleyl tails. The binding energy between oleic acid and the PbS (001) surface is calculated as:

$$E(\text{bind}) = E(\text{mol/surf}) - E(\text{surf}) - E(\text{mol}), \quad (2.3)$$

where $E(\text{mol/surf})$ is the energy of the whole system, $E(\text{surf})$ is the energy of the system slab with an un-passivated nonpolar $\text{PbS}(001)$ surface (after atomic relaxation), $E(\text{mol})$ is the free energy of the passivating molecule in the solvent, including solvent binding effects. There are two types of solvent binding effects. One is hydrogen-bonding between functional groups, another is van der Waals (vdW) interaction between alkene chains. While the first type can be described accurately by the GGA method, it is not possible for the second type. In addition, due to the flexibility of the alkene chain, the second type of binding needs also include an entropic contribution at room temperature. However, one can argue that the alkene chain vdW interactions for molecules on the surface and in the solvent should be approximately the same, as long as the chain volume density on the surface (with roughly vertically standup chains) is less than the alkene chain density in the solvent. As a result, either the flexible alkene chains at the surface tilt to optimize the chain-chain distance, or the solvent 1-octadecene (ODE) can intercalate into the surface layer to increase the alkene chain density. Thus, the tail chain vdW energy in $E(\text{mol/surf})$ should cancel out vdW energy in $E(\text{mol})$. Also it should be noted that on the surface the vdW interaction is mostly between the tail chains of the oleate, while in the solvent, it is mostly between the tail chain of oleate and solvent ODE molecules. Since the ODE chain is similar to that in the oleate, a similar vdW binding energy is expected. With these approximations we have removed the GGA alkyl chain-alkyl chain vdW interactions from $E(\text{mol/surf})$ in Eq.(2.3). Meanwhile, for $E(\text{mol})$ we included the -0.83 eV binding energy of the OAH-OAH dimer (due to hydrogen bond), which forms in the solvent. We assume there is an appreciable amount of OAH in the solvent, thus the concentration entropy term of OAH can be ignored. The final calculated (001) binding energy is -0.16 eV per oleic acid as listed in Table 2.1.

Table 2.1. Surface, passivation and binding energies for the (001) and (111) NC facets of PbS nanocrystals with lowest energy passivation configuration. The (001) and (111) surface area per OAH(OA⁻) molecule is 35.2 and 30.5 Å² respectively.

	(001)	(111)
Unpassivated Surface (meV/Å ²)	12.31	23.47*
Binding E per OAH(or OA ⁻) (eV)	-0.16	-0.52
Total surface Energy (meV/Å ²)	7.76	6.33

*-reconstructed surface

Capping of the polar (111) facets in the NC is more complicated due to the need for charge compensation (26-28) to satisfy the electron counting rule (29-32). It should be noted that the NC formed in Eq.(2.2) has equal numbers of Pb and S. As a result it will have nonpolar (111) facets with only half of the terminal Pb atoms (28, 33). We then consider whether the Pb(OA)₂·H₂O group in the solvent can fill-in the surface vacancies (missing Pb atoms). We found that, in agreement with Bealing et. al (12), it is sterically impossible to fill every missing Pb atom of the (111) surface with one Pb(OA)₂. However, one OA for each missing Pb is sterically possible. In order to satisfy the electron counting rule, an anionic species needs to be introduced. This is provided by H₂O, which can be dissociated into OH and H, with the H combining with the extra OA to form a stable OAH which is released into the solvent:



where (PbS)_N(111) denotes the reconstructed nonpolar surface and Pb_{N+1}S_N(111) the full Pb-terminated polar surface. This reaction is shown graphically in Fig. 2.2. The binding energy of this passivation in the minimum energy configuration is -0.52 eV per oleate as shown in Table 2.1, which is much larger than the (001) surface binding energy. This energy is the ΔG of reaction (4) (i.e., total energy difference between the right and left hand sides of Eq. (2.4)). The minimum energy configuration (after considering several possible configurations) of OA·Pb_{N+1}S_N(111)·OH is shown in Fig. 2.1C, where the OA group stabilizes the Pb ions via μ²-bidentate bridging bonds and the OH group stabilizes the Pb ions via μ³-Pb₃-OH bonds. The overall structure satisfies the electron counting rule. When we calculate E(OAH) in Eq. (2.4), we have included the OAH-OAH dimer interaction of -0.83 eV. As discussed before, we have removed the GGA vdW interaction of the oleyl tails in OA·Pb_{N+1}S_N(111)·OH of Eq. (2.4). We have also considered many other possible passivation stoichiometries and configurations, but found none of them is as stable as the ones considered above as shown in Table 2.2.

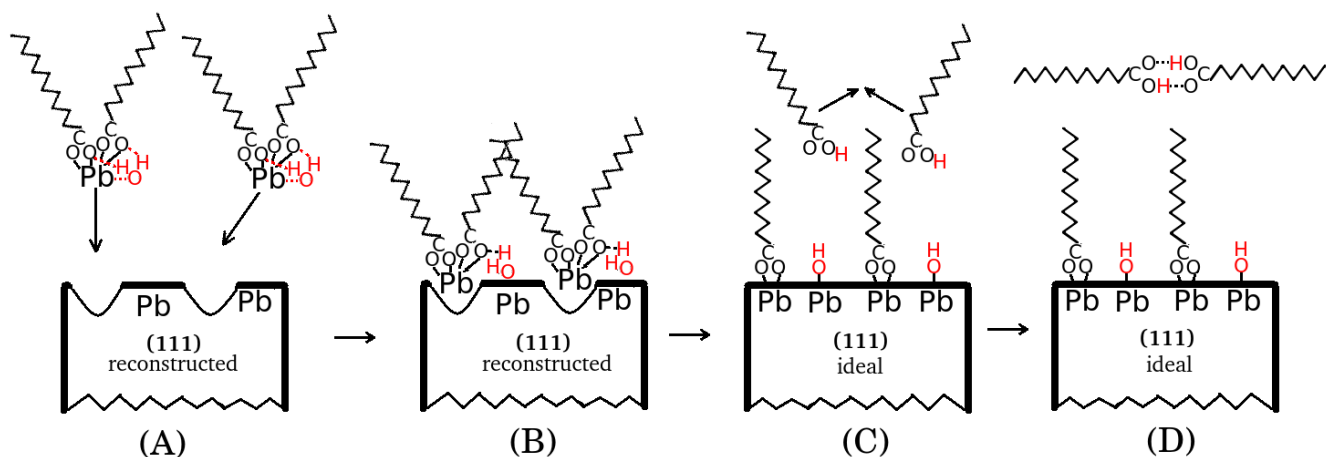


Figure 2.2. Multi-step process for building up the (111) facets of PbS-NC. (A) $\text{Pb(OA)}_2 \cdot \text{H}_2\text{O}$ complexes dissolved in the solution approaching the nonpolar and stoichiometric (111) facets. (B) The Pb ions bind to surface vacancies. (C) One of the two OA^- in each $\text{Pb(OA)}_2 \cdot \text{H}_2\text{O}$ complex is removed from the surface due to steric effects, and the water molecule dissociated into OH group binding to the surface and H^+ binding to the removed OA^- . (D) Finally, the desorbed OAH molecules dimerise in the solvent.

Table 2.2. Ligand binding energies (in eV) on the (111) PbS NC surfaces for a 4 Pb atoms area (counted from the full Pb termination case). For Pb(OA)_2 , we have taken into account the H_2O molecule binding with Pb(OA)_2 in the solvent, and binding as liquid water after Pb(OA)_2 is bind on the surface. The 2OA,2OH (our current model) value is twice that shown in Table I since the surface area considered here is twice as large. The OA, O^{2-} corresponds to the case where the 2OH form one O on the surface and one H_2O leaving the surface.

2OA,2OH	-1.04
2OA, O^{2-}	-0.60
Pb(OA)_2 half-filled	-0.03
2Pb(OA)_2 full-filled	+3.78

In order to predict the shape of the PbS NC, we have calculated the surface energies of (001) and (111) surfaces, which are equal to the unpassivated surface energies (nonpolar for (111)) plus the binding energies calculated above. The unpassivated surface energies can be calculated easily using energies of slabs minus their corresponding bulk values. The resulting surface energies, shown in Table 2.1, can be used in the Wulff reconstruction (34-38) to determine the shape of the NC in equilibrium. Our calculation gives a (001) to (111) Wulff ratio of 0.82, which agrees excellently with the average 0.82 ratio derived from TEM images (Fig. 2.3). With this procedure, it is now possible to construct a realistic NC with all the atomic scale surface passivation features. One example is shown in Fig. 2.4A with additional OH groups placed at the edge. To further study whether such a 3D passivation model can provide good passivation to the edge and corner

of the NC, we have truncated the alkyl chains of the oleic acids, making them acetic acids (which is not expected to change its surface electronic structures). After this simplification we are able to relax the atomic structures of a NC (2325 atoms, 4 nm diameter) using DFT/GGA calculations. The final system shows perfect surface passivation, with clean valence band minimum (VBM) and conduction band maximum (CBM) states, without any gap states (Fig. 2.4B). This result demonstrates that, under the current surface passivation pattern, it is possible to provide good edge and corner passivations. Thus we propose that the 3D bulk structure determines the 2D surface passivation structure, which in turn determines the 1D edge passivation structure.

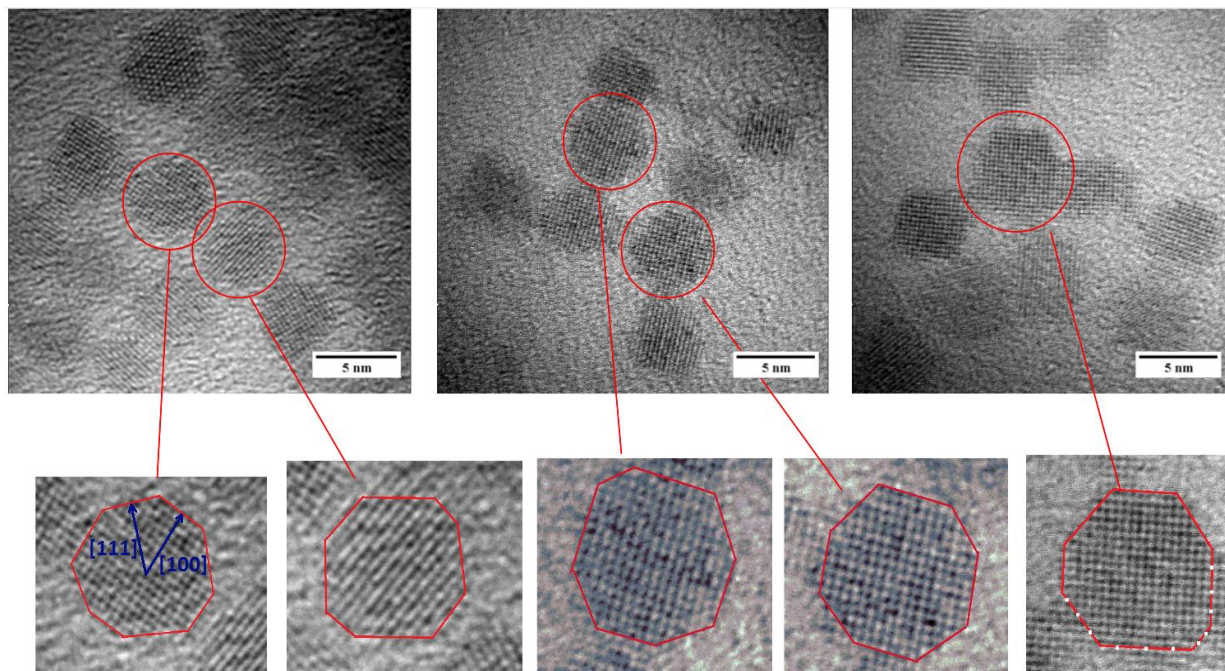


Figure 2.3. TEM images of PbS-NCs. High-resolution TEM images of the synthesized PbS-NC with enlarged views of selected NC shown below. The (111)/(001) center to surface Wulff ratios of the NCs are 0.820, 0.762, 0.866, 0.847, 0.792 from left to right, respectively, with an average ratio of 0.817, in good agreement with the calculated value based on the surface energies (see text).

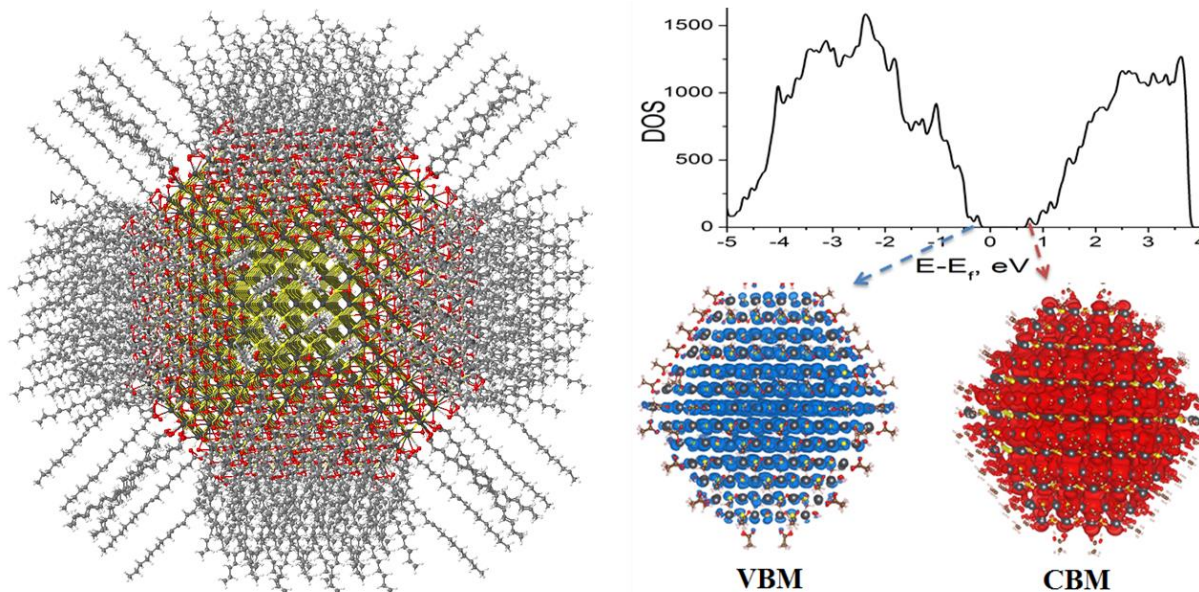


Figure. 2.4. Model of PbS-NC in colloidal solution. (A) The atomic structure of a 5 nm diameter NC passivated with OA^- and OH^- ligands. (B) The electron density of states, and VBM and CBM levels of a NC passivated with truncated oleic acid alkyl chains.

For a 5 nm NC, the above construction also provides the ratio between excess-Pb and S atoms, and between excess-Pb atoms and surface OA molecules. Our results for these two values for the model shown in Fig.4 are 0.19:1 and 1.18:1 respectively, which agree closely to our experimentally observed values of 0.21:1 (as measured by RBS) and 0.97:1 as reported in Ref. (7), respectively. In our model, the ligand surface binding energy in (001) is much smaller in amplitude than the value in (111). This is consistent with the following observations: (a) the NC in Fig. 3 all stand up on the (001) surface; (b) when lead chalcogenide NCs undergo oriented attachment to form a wire, they fuse via the (001) facets (38). Both observations indicate that it is easier to remove the ligand molecules from the (001) facets.

2.3 Experimental Evidence of Nanocrystal Surface Hydroxylation

One of the most interesting features of our passivation model is the existence of the OH groups on the (111) facet. It is well known that H_2O can be easily dissociated into OH and H on transition metal or oxide surfaces (40-43). The binding of H_2O to $\text{Pb}(\text{OA})_2$ in the solvent provides a natural kinetic pathway for this to happen (Fig. 2.2). We stress that this compact anion is also required to establish charge neutrality over the entire quantum dot which may not be achieved by OA molecules alone due to steric hindrance. This fact has previously been overlooked. We suggest that the co-existence of a steric demanding ligand like OA in conjunction with a smaller anion to fill the gaps and fulfill the electron counting rule could apply to other systems as well. To provide experimental evidence for this hypothesis, we carried out XPS and SFG measurements, with the XPS data shown in Fig. 2.5. Two NC samples are synthesized, one as described above (denoted as PbS-OH), another by following the procedure developed by Moreels *et al.* (44) which utilizes Cl^- and no water during the synthesis (denoted as PbS-Cl). In the PbS-Cl sample, the Cl^- anion has effectively replaced the OH^- anion. Both samples are spin coated on freshly cleaved graphite, followed by excessive washing with acetone

to remove unbound oleic acid ligands, and to achieve sub-monolayer coverage. The XPS data together with the two control samples, graphite and $\text{Pb}(\text{OH})_2$ powder, are taken and shown in Fig. 2.5. Although the graphite is freshly cleaved in Ar glove box (with less than 1ppm oxygen concentration), it is still slightly oxidized, possibly due to oxygen adsorption on various defects present on the graphite (45, 46), showing an O 1s peak at 534.0 eV. Due to the incomplete surface coverage, the PbS-Cl and PbS-OH nanoparticle sample also show the same 534.0 eV XPS peak, which comes from the graphite substrate. After subtracting this peak, the PbS-Cl shows only one additional peak at 532.1 eV, possibly due to oleate species. The PbS-OH sample contains three peaks at 534.0, 532.1 eV, and 531.2 eV. The new and clear 531.2 eV peak agrees with the $\text{Pb}(\text{OH})_2$ powder single peak at 531.2 eV, which also agrees with literature reported other metal-OH groups XPS peak values (47-50). This is thus a strong evidence that the 531.2 eV peak comes from the Pb-OH group at the surface of the PbS-OH NC sample. In the PbS-Cl sample, this feature is absent. However, we detected the existence of chlorine species by XPS, indicating the Cl^- anion has replaced the OH^- anion. Note the 534.0 eV and 532.1 eV peaks have the same widths in different samples in Fig. 2.5. This rigorous peak fitting procedure proves the existence of the 531.2 eV peak in the PbS-OH sample. We further performed SFG measurement which also indicates the existence of OH in the sample.

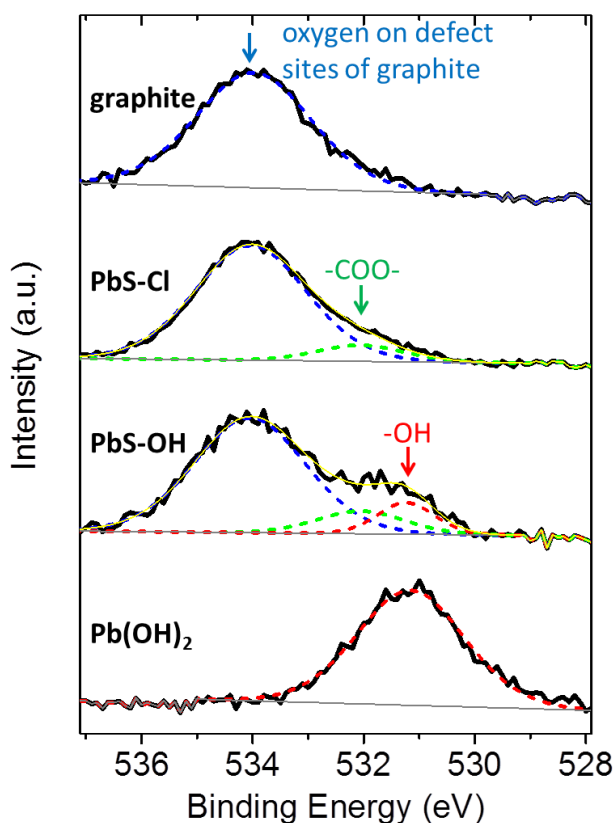


Fig. 5. The XPS spectra of PbS-NCs: O 1s XPS showing peaks at 531.2eV (red) from oxygen in OH groups, and at 532.1eV (green) from oxygen in carboxyl groups.

2.4 Conclusion

To conclude, through ab initio calculations and studies of the molecular mechanism of the

nanocrystal growth, we have constructed a detailed picture of the atomic structure and surface passivation of PbS NC by oleic acid that encompasses the whole synthetic process. This model predicts that the hydroxyl group, generated as a by-product of precursor decomposition, is also an important ingredient of the passivating layer on the (111) surface, an unexpected conclusion, which when taken into account yields consistency with multiple experiments. The model agrees with all the available experimental observations, including the exact shape of the NC. In particular, careful XPS measurements prove the existence of OH group on the surface of the NC, where FTIR measurements indicate the existence of water in the precursor. A 3D passivation model is provided with edges and corners passivated satisfactorily showing no gap states. We do note that what we proposed here might only apply to the samples prepared following the procedures described above. As there are many other possible procedures (e.g., the Cl passivated NC), the situations for other samples might be different. Nevertheless, a detailed understanding for even a single situation will be valuable in this field considering our current poor knowledge in the atomic details of ligand surface passivation.

References

1. A. P. Alivisatos, *Science* **271**, 933 (1996).
2. C. B. Murray, S. H. Sun, W. Gaschler, H. Doyle, T. A. Betley, C. R. Kagan, *IBM J. Res. Dev.* **45**, 47 (2001).
3. V. F. Puntès, K. M. Krishnan, P. A. Alivisatos, *Science* **291**, 2115 (2001).
4. Y. Yin, A. P. Alivisatos, *Nature* **437**, 664 (2005).
5. J. S. Steckel, B. K. H. Yen, D. C. Oertel, M. G. Bawendi, *J. Am. Chem. Soc.* **128**, 13032 (2006).
6. H. Liu, J. S. Owen, A. P. Alivisatos, *J. Am. Chem. Soc.* **129**, 305 (2007).
7. I. Moreels, B. Fritzinger, J. C. Martins, Z. Hens, *J. Am. Chem. Soc.* **130**, 15081 (2008).
8. J. Li, L.W. Wang, *Nano Lett.* **3**, 1357 (2003).
9. M. A. El-Sayed, *Acc. Chem. Res.* **37**, 326 (2004).
10. J. Schrier, L.W. Wang, *J. Phys. Chem. C* **112**, 11158 (2008).
11. M. Argeri, A. Fraccarollo, F. Grassi, L. Marchese, M. Cossi, *J. Phys. Chem. C* **115**, 11382 (2011).
12. C. R. Bealing, W. J. Baumgardner, J. J. Choi, T. Hanrath, R. G. Hennig, *ACS Nano* **6**, 2118 (2012).
13. D. L. Klein, R. Roth, A. K. L. Lim, A. P. Alivisatos, P. L. McEuen, *Nature* **389**, 699 (1997).
14. G. Markovich, C. P. Collier, S. E. Henrichs, F. Rémacle, R. D. Levine, J. R. Heath, *Acc. Chem. Res.* **32**, 415 (1999).
15. D. V. Talapin, J. S. Lee, M. V. Kovalenko, E. V. Shevchenko, *Chem. Rev.* **110**, 389 (2010).
16. A. Ip et al., *Nature Nanotech.* **7**, 577 (2012).
17. Y. Jun, J. Lee, J. Choi, J. Cheon, *J. Phys. Chem. B* **109**, 14795 (2005).
18. S.-M. Lee, Y. Jun, S.-N. Cho, J. Cheon, *J. Am. Chem. Soc.* **124**, 11244 (2002).
19. I. Moreels et al. *Chem. Mater.* **19**, 6101 (2007).
20. I. Moreels et al. *ACS Nano* **3**, 3023 (2009).
21. Q. Dai et al. *ACS Nano* **3**, 1518 (2009).
22. V. Petkov, I. Moreels, Z. Hens, Y. Ren, *Phys. Rev. B* **81**, 241304 (2010).
23. A. J. Houtepen, R. Koole, D.I. Vanmaekelbergh, J. Meeldijk, S. G. Hickey *J. Am. Chem. Soc.*

- 128**, 6792 (2006).
24. D. Britt et al., *Chem. Mater.* **25**, 2544 (2013).
 25. Yanover et al., *Chem. Mater.* **24**, 4417 (2012).
 26. Y. Gai, H. Peng, J. Li, *J. Phys. Chem. C* **113**, 21506 (2009).
 27. X. Huang, E. Lindgren, R. Chelokowsky, *Phys. Rev. B* **71**, 165328 (2005).
 28. K. Shiraishi, *J. Phys. Soc. Jpn.* **59**, 3455 (1990).
 29. C. B. Duke, *Chem. Rev.* **96**, 1237 (1996).
 30. G. P. Srivastava, *Rep. Prog. Phys.* **60**, 561 (1997).
 31. L. Manna, L. W. Wang, R. Cingolani, A. P. Alivisatos, *J. Phys. Chem. B* **109**, 6183 (2005).
 32. C. Fang, M. A. van Huis, D. Vanmaekelbergh, H. W. Zandbergen, *ACS Nano* **4**, 211 (2010).
 33. K. Kimura, K. Nakajima, Y. Fujii, M. Mannami, *Surf. Sci.* **318**, 363 (1994).
 34. G. Wulff, *Z. Krystallog.* **34**, 449 (1901).
 35. R. Shuttleworth, *Proc. Phys. Soc. A* **63**, 444 (1950).
 36. C. Herring, *Phys. Rev.* **82**, 87 (1951).
 37. E. Ringe, R.P. van Duyne, L. D. Marks, *Nano Lett.* **11**, 3399 (2011).
 38. S. Polarz, *Adv. Func. Mater.* **21**, 3214 (2011).
 39. C. Schliehe et al. *Science* **329**, 550 (2010).
 40. P. Eng et al. *Science* **288**, 1029 (2000).
 41. P. Feibelman, *Science* **295**, 99 (2002).
 42. S. Khan, M. Al-Shahry, W. Ingler, *Science* **297**, 2243 (2002).
 43. H. J. Shin et al., *Nat. Mater.* **9**, 442 (2010).
 44. I. Moreels et al., *ACS Nano*, **5**, 2004 (2011).
 45. W. -T. Pong, C. Durkan, *J. Phys. D: Appl. Phys.* **38**, R329 (2005).
 46. S. Wu, R. Yang, D. Shi, G. Zhang, *Nanoscale* **4**, 2005 (2012).
 47. X. Deng, A. Verdaguer, T. Herranz, C. Weis, M. Salmeron, *Langmuir* **24**, 9474 (2008).
 48. K. Anderson, A. Nikitin, L.G. Petterssen, A. Nilsson, H. Ogasawara, *Phys. Rev. Lett.* **93**, 196101 (2004).
 49. J.A.Th. Verhoeven, H. Van Doveren, *Surf. Sci.* **123**, 369 (1982).
 50. F. Ruedaa, J. Mendialdua, A. Rodriguez, R.Casanovaa, Y. Barbauxb, L. Gengembreb, L. Jalowiecki, *J. Electron Spectrosc. Relat. Phenom.* **82**, 135 (1996).

Chapter 3: Measuring the Charge State of Single Nanoparticles

Reproduced in part and adapted with permission from Nano Letters 2015, 15 (1), 51-55.
Copyright © 2015, American Chemical Society.

3.1 Abstract

Electrostatic interactions at the nanoscale can lead to novel properties and functionalities that bulk materials and devices do not have. In this chapter we used Kelvin probe force microscopy (KPFM) to study the work function (WF) of gold nanoparticles (NPs) deposited on a Si wafer covered by a monolayer of alkyl chains, which provided a tunnel junction. This presents a simple model system to understand the nontrivial nanoscale electrostatics. We found that the WF of Au NPs is size-dependent, and deviates strongly from that of the bulk Au. We attribute the WF change to the charging of the NPs, which is a consequence of the difference in WF between Au and the substrate. For a NP with 10 nm diameter charged with ~5 electrons, the WF was found to be only ~3.6 eV. A classical electrostatic model was derived that explains the observations in a quantitative way. We also demonstrate that the WF and charge state of Au NPs are influenced by chemical changes of the underlying substrate. Therefore, Au NPs could be used for chemical and biological sensing, whose environmentally sensitive charge state can be read out by work function measurements.

3.2 Work Function Measurement of Single Au Nanoparticles

When bulk materials are scaled down to the nanoscale, novel properties emerge, such as size-dependent bandgaps due to quantum confinement^{1,2}, enhanced catalytic properties due to the large surface area and rich surface structure,^{3,4} and plasmonic effects due to localized collective electron oscillation.^{5,6} Another property that is often overlooked is the electrostatic interactions that lead to changes in work function, which is defined as the minimum thermodynamic work needed to extract an electron from a material to a point in vacuum immediately outside the surface.⁷ As an example, Au nanoparticles from 3 nm to tens of nanometers are metallic,^{8,9} although their WF deviates from that of the bulk Au, due to electrostatic effects.^{10,11} For isolated neutral metal NPs this is due to image force and Coulomb interactions.¹⁰ However, when these NPs are interacting with the nearby environment, as is inevitable in device applications, their WF diverges from that of free particles.¹² In this case, the WF is no longer an intrinsic property of the NPs, but depends critically on the chemical composition and electronic properties of the adjacent materials. Although electrostatic charge transfer was assumed to be responsible for the environmental dependence of the WF of metal NPs,¹² there has been no evidence or explanation of this effect. Here we report measurements of the change in the WF of Au NPs as a function of their size, and explain the nature of the phenomenon by deriving a quantitative expression of the charge transfer. In contrast to atomic and molecular adsorbate systems that modify the WF of the substrate by the formation of electric dipole moments,^{13,14} metal NPs exhibit unique nanoscale Coulomb confinement effects determining their WF.

Au NPs were deposited on a heavily n-doped silicon substrate pre-covered with an insulating monolayer film of alkyl chain molecules that provide a tunnel junction coupling between the NPs and the substrate. We expect that electrons will transfer from the Si to Au (due to their WF

difference) by tunneling through the junction. The chemical inertness of Au and the ability to controllably oxidize the Si substrate make our sample an ideal platform to observe the effect of environmental factors on the charge state of Au NPs, and the consequent effect on WF change.

The gold nanoparticles were synthesized by reduction of a gold salt with ascorbic acid. Figure 3.1(a) shows transmission electron microscopy (TEM) images of three representative Au NPs. The NPs have a size distribution ranging from 3 nm to ~25 nm (Figure 3.1(b)), and are roughly spherical in shape. They were deposited on an amine-terminated C7 alkane monolayer grafted on heavily n-doped oxide-free Si(111) (phosphorus doped, $2 \times 10^{18} \text{ cm}^{-3}$).^{15,16} The amine group provides binding to the Au NPs. This grafted organic monolayer will be referred to as GOM. The ascorbic surfactants capping the NPs were removed prior to KPFM measurements with a 30 min annealing in vacuum at 150 °C. The GOM layer remained intact after this annealing process.¹⁶ The GOM surface was not modified after annealing and the NP surface coverage remained $\sim 1 \times 10^9 \text{ cm}^{-2}$ (10 NP/ μm^2) as evaluated with atomic force microscopy (AFM).

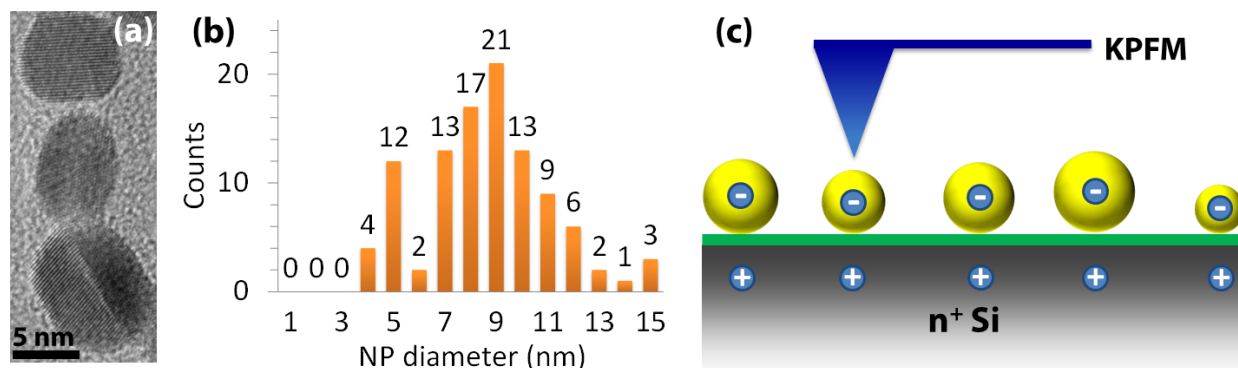


Figure 3.1. Au nanoparticles and work function measurements. (a) High resolution TEM image showing three Au NPs. (b) Size distribution histogram analyzed from TEM images of 103 particles. (c) Schematic diagram of the KPFM measurements of the Au NPs deposited on a Si substrate covered with a grafted organic monolayer (GOM).

The schematic setup of the KPFM measurement is shown in Figure 3.1(c). The home-built single pass, frequency modulation KPFM has a resolution of $\sim 10 \text{ mV}$.¹⁷ During KPFM measurements, the sample was grounded, while a bias $V_{DC} + V_{AC} \cos \omega t$ was applied to the conductive AFM tip, with $V_{AC} = 2 \text{ V}$, $\omega = 2 \text{ kHz}$. The electric field between the tip and surface, due to the contact potential difference and applied voltage, shifts the frequency and phase of the oscillating cantilever away from its free resonant value ($\omega_0 \approx 75 \text{ kHz}$). It can be shown that the cantilever phase shift at ω is:¹⁸

$$\Delta f_{\omega} \propto \frac{\partial^2 C}{\partial z^2} (V_{DC} - CPD_{tip-sample}) V_{AC}, \quad (3.1)$$

where $CPD_{tip-sample}$ is the contact potential difference between the tip and the sample. C is the tip-sample capacitance, and z is the tip-sample distance (typically $< 5 \text{ nm}$ during imaging). V_{DC} is adjusted by the feedback control to maintain $\Delta f_{\omega} = 0$, so that its value is equal to the tip-sample contact potential difference. This compensation of the CPD also minimizes tip-sample electrostatic forces, allowing determination of the true sample topography.¹⁸⁻²¹ For simplicity, in all the results shown here the CPD was calibrated by setting the average CPD of the GOM to

zero. The calibrated CPD signal of the NP is related with its work function via the following relation:

$$CPD(NP) = (W_{GOM} - W_{NP})/e, \quad (3.2)$$

where W_{GOM} and W_{NP} are the work functions of the GOM and the Au NPs, respectively. e is the absolute value of the elementary charge. This relation shows that the changes in CPD and work function are of opposite sign.

With our setup, we obtain the surface topography and CPD images simultaneously in non-contact mode, allowing for a direct determination of NP size and WF. In contrast to electrostatic force microscopy, which can be utilized to manipulate the amount of charge in a tunnel junction,²² KPFM can detect the WF of the NPs without changing their charge state, since the CPD is balanced by the tip bias to nullify the electric field.

Figure 3.2(a) and (b) shows topography and CPD images of one area. The height profile through 6 NPs shows a variation between 6 and 17 nm, in agreement with the NP size distribution measured by TEM. In the CPD image the NPs appear as depressions (negative CPD), revealing that their WF is higher than that of the GOM on the Si(111) substrate. The GOM layer is electrically homogeneous, with a CPD fluctuation of less than 40 mV over the scanned area. As we can see in the profiles (c) and (d), particle #5 has a size of 17 nm and a CPD of -310 mV, and particle #6, with a size of 7 nm, has a CPD of -160 mV. Except for particle #4, the larger the NP, the more negative its CPD. A systematic study was carried out on 27 different NPs with sizes varying from 5 to 18 nm. A plot of the CPD (left scale) as a function of NP diameter (Figure 3.2(e)) shows that the CPD increases (i.e. WF decreases) when the NP diameter decreases. The work function of the GOM, found to be 3.4 eV by ultraviolet photoelectron spectroscopy (UPS), was used to obtain the WF of Au NPs (Equation (3.2)), as shown in the right scale in Figure 3.2(e). We can see that the WF of Au NPs deviates substantially from that of the bulk Au ($W_{Au} \approx 5.1$ V).²³ We note that our KPFM setup can only accurately measure the WF of NPs larger than 5 nm due to the limited spatial resolution imposed by our tip radius and imaging distance. For this reason the values for NPs smaller than 5 nm are not included. The data points for NPs larger than 20 nm are not included either, due to their irregular shape. The observed 0.1 – 0.2 eV WF fluctuation of NPs with the same size can be due to the variation in particle shape, and the orientation of the exposed facets,²⁴ as well as from the presence of steps and kinks.²⁵

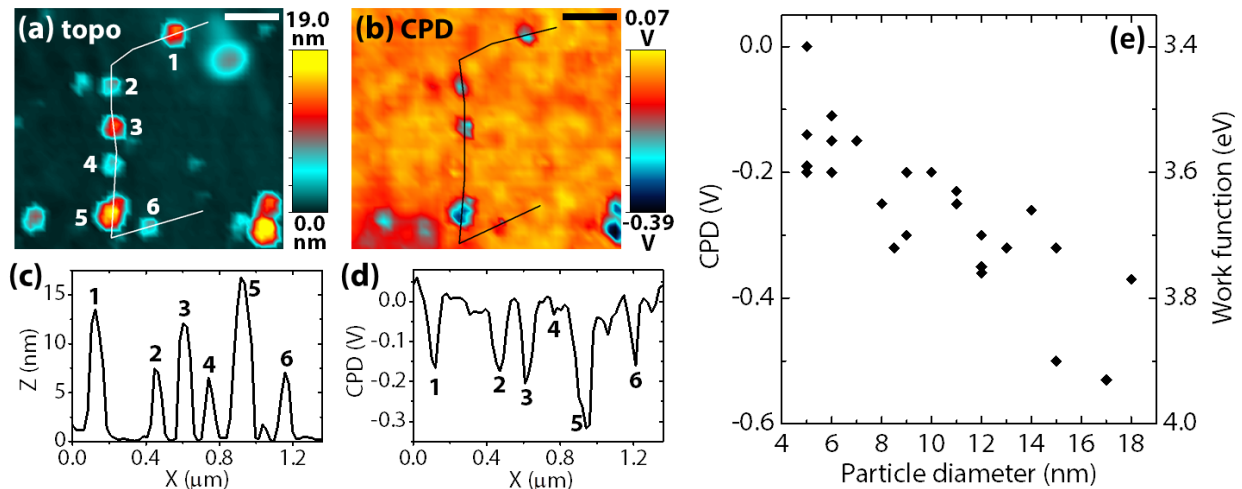


Figure 3.2. Nanoparticle work function vs. size. (a) and (b) are simultaneously obtained topography and CPD images of NPs on the GOM covered Si substrate. Six NPs are labeled 1 to 6. Scale bar: 200 nm. The cross section profiles of topography (c) and CPD (d) indicate that in general the CPD is more negative when the NP size is larger. (e) CPD as a function of NP diameter (left scale). The right scale is the corresponding WF calibrated with the value determined by UPS on the GOM covered Si surface.

3.3 Mechanism of Charge State Controlled Work Function

Our results can be explained by the charge transferred between the substrate and the Au NP as a result of the mismatch between their work functions. The value of this charge is determined by the capacitance between the NP and the substrate. The charge produces an electrostatic field that leads to a change in the WF of the NPs. If instead of the NPs we had a metal film over the GOM, the Coulomb field would be zero above it (the field is confined between the film and the substrate). However in the case of isolated nanoparticles the field extends outside with a value that depends on its size.

To calculate the Coulomb potential and to extract the charge state we start with Wood's formula¹⁰ for neutral isolated metal nanospheres, and modify it to derive the WF change of grounded charged metal nanospheres. The WF difference between a metal NP and the corresponding bulk metal (ΔW) arises from a difference in image force fields (ΔW_{im}) and from the Coulomb field near the surface of the NP due to the stored charges inside (ΔW_C):

$$\Delta W = \Delta W_{im} + \Delta W_C. \quad (3.3)$$

The first term is the difference between the image potential energy at the surface of a sphere and that of a flat metal plane:

$$\Delta W_{im} = -\frac{1}{8} \frac{1}{4\pi\epsilon_0} \frac{e^2}{R}. \quad (3.4)$$

where ϵ_0 is the vacuum permittivity, and R is the radius of the sphere. The charges inside the metal nanosphere, considered to reside at its center,²⁶ induce a Coulomb potential energy at the surface:

$$\Delta W_C = N \frac{1}{4\pi\epsilon_0} \frac{e^2}{R}, \quad (3.5)$$

where N is the charge state of the NP, which can be either positive or negative. The contribution to N of the image charges from the depletion region in the Si substrate is negligible. Combining ΔW_{im} and ΔW_C we get:

$$\Delta W = \left(2N - \frac{1}{4}\right) \frac{1}{4\pi\epsilon_0} \frac{e^2}{D}, \quad (3.6)$$

$$N = \frac{2\pi\epsilon_0}{e^2} D \cdot \Delta W + \frac{1}{8} = \frac{D}{2.88 \text{ nm}\cdot\text{eV}} \cdot \Delta W + \frac{1}{8}, \quad (3.7)$$

where D is the diameter of the sphere.

Using Equation (3.7), we can extract the charge state of the Au NPs as a function of their diameter. The results are shown in Figure 3.3(a). We can see that all the Au NPs are negatively charged, and the number of charges increases with the NP diameter.

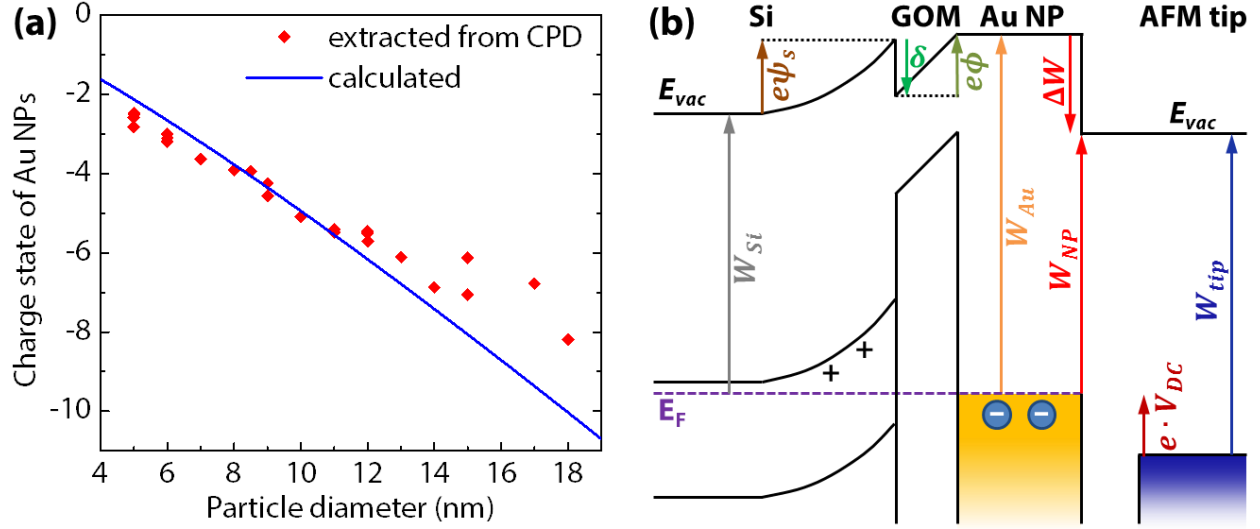


Figure 3.3. Charge state sensing and its mechanism. (a) Charge state of the Au NPs as extracted from the measured CPD, and from calculations based on band diagram and capacitance analysis. (b) Band alignment diagram of the Au NP-GOM-Si junctions. The WF difference between charged Au NP and bulk Au (ΔW) arises mainly due to the Coulomb field produced by the charges inside the NP. The KPFM tip senses the WF of the NPs by applying a DC tip bias (V_{DC}) to align their vacuum level with that of the tip (Equation 3.1). E_F : Fermi level; E_{vac} : vacuum level. ψ_s : band bending inside Si.

To understand the mechanism of the charge storage we consider the band diagram shown in Figure 3.3(b). The bulk work function of the n-doped Si is $W_{Si}=4.15$ eV. There is a depletion region near the surface of the Si which contains positive charge as a result of electron transfer to the Au NP. In the region containing the GOM there is a potential energy drop of $\delta \approx -0.6$ eV due to the dipole moment at the Si-GOM interface and inside the GOM.²⁷⁻²⁹ Since our NPs are larger than 3 nm, their electronic properties are similar to those of bulk Au.^{8,9} Therefore the energy separation between vacuum level and Fermi level in the NP is nearly the same as that in bulk Au. Using a Poisson solver, we calculated the built-in potential between the Au and the Si surface to be $\phi = 0.67$ V.

To calculate the value of the charge in the Au NP (eN) for comparison with the measured results, we calculate the capacitance (C) of a gold sphere separated from a Si surface by a thin dielectric using a semi-analytical formula.³⁰ The charge state of the Au NPs was then calculated using $N = -\phi C/e$, shown in Figure 3.3(a) (blue line). The calculated values matches with those obtained from the CPD measurements. The small discrepancies for NPs larger than 15 nm may arise from the deviation of the NP shape from a sphere, as we have seen in TEM images.

3.4 Chemical Sensing via Work Function Measurements

Since the charge state of metal NPs depends on the local electronic environment, their WF will also reflect local chemical changes. According to Equation (3.6), the sensitivity of the WF on the charge state is $\frac{2.88 \text{ nm}\cdot\text{eV}}{D}$ per charge, which for a 5 nm NP amounts to ~ 0.6 eV. To demonstrate this effect we modified the surface chemistry of the Si substrate by oxidizing the sample by

exposure to oxygen, and measured the resulting change of WF of the Au NPs. We observed by X-ray photoelectron spectroscopy (XPS) and UPS that the Si(111) surface was fully oxidized after 3 days exposure to air, while the Au NPs remain intact. UPS also showed that the WF of the GOM-covered surface increased by 0.3 eV. With KPFM we imaged the CPD of the sample at different oxidation stages, and observed that the CPD of the GOM surface becomes inhomogeneous when partially oxidized (Figure 3.4(a)), and homogeneous again when the surface oxidation is complete (Figure 3.4(b)). The height distribution and shape of the Au NPs did not change with substrate oxidation.

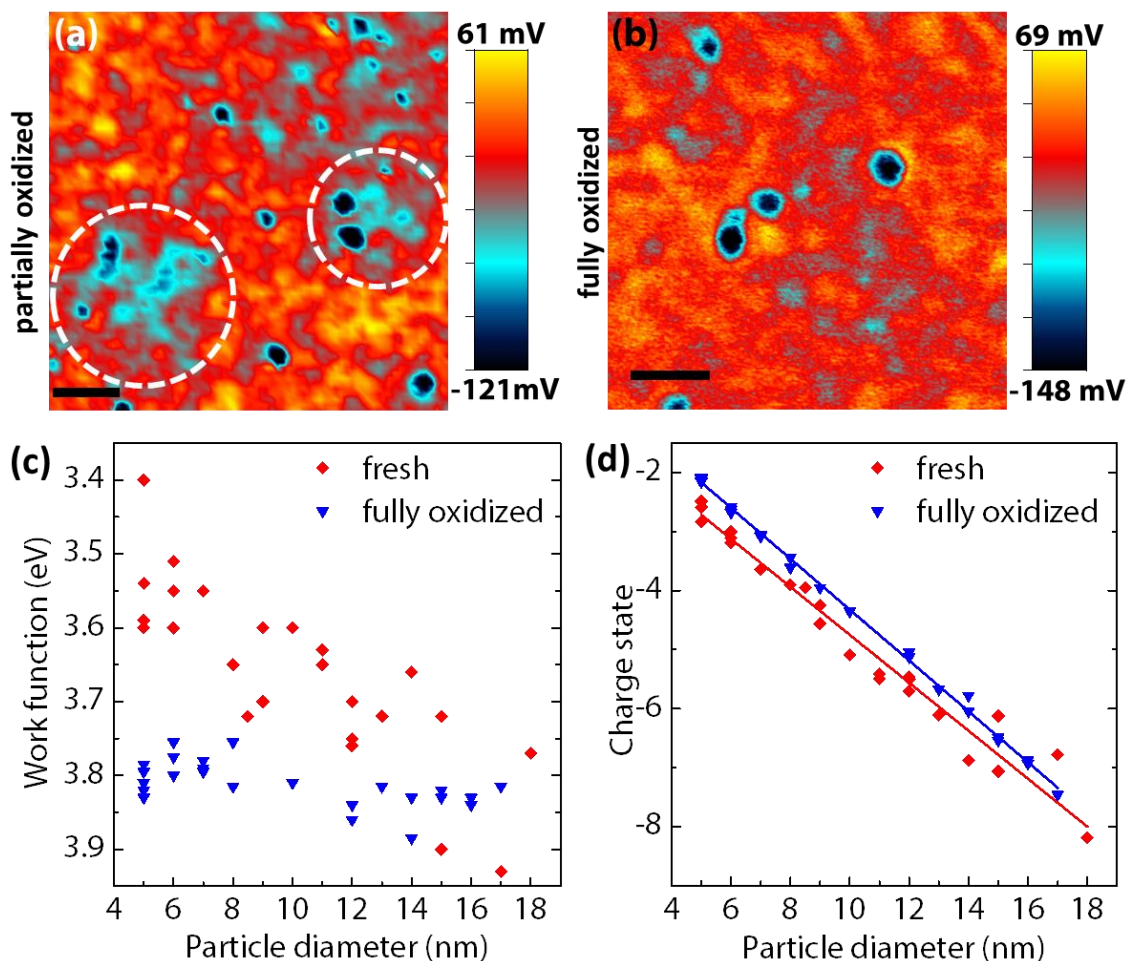


Figure 3.4. Effect of Si oxidation on the charge state and WF of the Au NPs. (a) and (b) are CPD images of the sample after exposure in AFM chamber for 2 days (nitrogen purged, relative humidity below 0.5%) (a) and 3 days in air (b). Scale bar: 200 nm. In (a), the areas circled by white dashed lines and several other low CPD areas (blue/cyan areas) correspond to local oxidation spots. In (b) the surface is uniformly oxidized. (c) WF vs. NP size for the fresh sample (same as Figure 3.2(e)) and for the fully oxidized sample (3 days exposure to air). (d) Charge state extracted from the WF in (c), with linear fits.

We analyzed the WF and the extracted charge state of the fully oxidized sample as shown in Figure 3.4(c) and 3.4(d). We observed an increase of WF for small NPs (5 nm – 15 nm), corresponding to a slight decrease in the amount of stored electrons. This can be explained by the

decrease of capacitance between the Au NPs and the Si surface, as a result of the increased tunnel barrier thickness after Si surface oxidation. The WF is weakly dependent on the size of the NPs after substrate oxidation, while the charge state is more linearly dependent on the particle diameter (as shown by Equation (3.7), a size-independent ΔW leads to $(N - \frac{1}{8}) \propto D$). This is a result of the linear dependence of C on NP size, which approaches the self-capacitance of the NP, as a result of the decreased coupling between the NP and substrate when the dielectric thickness increases. The change of the size-dependence of WF is more pronounced than that of the charge state, indicating that WF is very sensitive to changes of charge state. We therefore expect sensing applications where the chemical environment induces charge state changes of the metal NPs, which is amplified and detected by WF measurements.

3.5 Conclusion

In summary, we found that the work function of Au NPs is dominantly determined by their charge state and can deviate strongly from that of bulk Au. We can envision sensing applications based on this novel phenomenon, where scalable devices can be made using metal NPs, and the change of their WF can be detected via nanomechanical or capacitive measurements. Compared to the previously demonstrated single electron transistor devices³¹ which require three terminals (source and drain need to be within tunneling range) and low temperature operation, the WF-based charge sensing device only requires two terminals (source is within tunneling range to the NP, while sensing electrode can be a few nm away) and can operate at room temperature, opening up potential in-situ chemical and biological sensing applications.

References

1. Talapin, D. V.; Lee, J.; Kovalenko, M. V.; Shevchenko, E. V. *Chem. Rev.* **2010**, 110, 389–458.
2. Li, L.; Hu, J.; Yang, W.; Alivisatos, A. P. *Nano Lett.* **2001**, 1, 349–351.
3. Bell, A. T. *Science* **2003**, 299, 1688–1691.
4. Cargnello, M.; Doan-Nguyen, V. V. T.; Gordon, T. R.; Diaz, R. E.; Stach, E. A.; Gorte, R. J.; Fornasiero, P.; Murray, C. B. *Science* **2013**, 341, 771–773.
5. Novotny, L.; van Hulst, N. *Nat. Photonics* **2011**, 5, 83–90.
6. Wang, H.; Brandl, D. W.; Le F.; Nordlander, P.; Halas, N. J. *Nano Lett.* **2006**, 6, 827–832.
7. Kittel, C. *Introduction to Solid State Physics*, 7th Edition; Wiley: New York, 1995.
8. Valdenm, M.; Lai X.; Goodman D. W. *Science* **1998**, 281, 1647–1650.
9. Häkkinen, H. Theoretical Studies of gold nanoclusters in various chemical environments: when the size matters. In *Gold nanoparticles for physics, chemistry and biology*; Louis, C., Pluchery, O., Eds.; Imperial College Press, 2013.
10. Wood, D. M. *Phys. Rev. Lett.* **1981**, 46, 749.
11. Zhou, L.; Zachariah, M. R. *Chem. Phys. Lett.* **2012**, 525–526, 77–81.
12. Stehlik, S.; Petit, T.; Girard, H. A.; Arnault, J.; Kromka, A.; Rezek, B. *Langmuir* **2013**, 29, 1634–1641.
13. Sasahara, A.; Pang, C. L.; Onishi, H. *J. Phys. Chem. B* **2006**, 110, 17584–17588.
14. de Boer, B.; Hadipour, A.; Mandoc, M. M.; van Woudenberg, T.; Blom, P. W. M. *Adv. Mater.* **2005**, 17, 621–625.

15. Aureau, D.; Varin, Y.; Roodenko, K.; Seitz, O.; Pluchery, O.; Chabal, Y. J. *J. Phys. Chem. C* **2010**, *114*, 14180–14186.
16. Caillard, L.; Seitz, O.; Campbell, P.; Doherty, R. P.; Lamic-Humblot, A.; Lacaze, E.; Chabel, Y. J.; Pluchery, O. *Langmuir* **2013**, *29*, 5066–5073.
17. Zhang, Y.; Ziegler, D.; Salmeron, M. *ACS Nano* **2013**, *7*, 8258–8265.
18. Li, G.; Mao, B.; Lan, F.; Liu, L. *Rev. Sci. Instrum.* **2012**, *83*, 113701.
19. Sadewasser, S.; Carl, P.; Glatzel, T.; Lux-Steiner, M. -Ch. *Nanotechnology* **2004**, *15*, S14–S18.
20. Ziegler, D.; Rychen, J.; Naujoks, N.; Stemmer, A. *Nanotechnology* **2007**, *18*, 225505.
21. Ziegler, D.; Naujoks, N.; Stemmer A. *Rev. Sci. Instrum.* **2008**, *79*, 063704.
22. Tekiel, A.; Miyahara, Y.; Topple, J. M.; Grutter, P. *ACS Nano* **2013**, *7*, 4683–4690.
23. Haynes, W. M. *CRC Handbook of Chemistry and Physics*, 93rd Edition; Taylor & Francis, 2012.
24. Michaelson, H. B. *J. Appl. Phys.* **1977**, *48*, 4729–4733.
25. Besocke, K.; Krahl-Urban, B.; Wagner, H. *Surf. Sci.* **1977**, *68*, 39–46.
26. Jackson, J. D. *Classical Electrodynamics*, 2nd Edition; Wiley: New York, 1975.
27. Magid, I.; Burstein, L.; Seitz, O.; Segev, L.; Kronik, L.; Rosenwaks, Y. *J. Phys. Chem. C* **2008**, *112*, 7145–7150.
28. Hacker, C. A. *Solid-State Electron.* **2010**, *54*, 1657–1664.
29. Yaffe, O.; Scheres, L.; Segev, L.; Biller, A.; Ron, I.; Salomon, E.; Giesbers, M.; Kahn, A.; Kronik, L.; Zuilhof, H.; Vilan, A.; Cahen, D. *J. Phys. Chem. C* **2010**, *114*, 10270–10279.
30. Gomila, G.; Toset, J., Fumagalli, L. *J. Appl. Phys.* **2008**, *104*, 024315.
31. Yoo, M. J.; Fulton, T. A.; Hess, H. F.; Willett, R. L.; Dunkleberger, L. N.; Chichester, R. J.; Pfeiffer, L. N.; West, K. W. *Science* **1997**, *276*, 579–582.

Chapter 4: Organic-Inorganic Interfacial Charge Trapping States

Reproduced in part and adapted with permission from ACS Nano 2013, 7 (9), 8258–8265.
Copyright © 2013, American Chemical Society.

4.1 Abstract

Using Kelvin probe force microscopy (KPFM) we studied the local charge trapping states at the SiO₂ – oligothiophene interface in a field effect transistor (FET), where SiO₂ is the gate dielectric. KPFM reveals surface potential inhomogeneities within the oligothiophene monolayer, which correlate with its structure. A large peak of trap states with energies in the oligothiophene's bandgap due to hydroxyl groups is present at the oxide surface. We show that these states are successfully eliminated by pre-adsorption of a layer of (3-Aminopropyl) triethoxysilane (APTES). Time resolved surface potential transient measurements further show that the charge carrier injection in the non-passivated FET contains two exponential transients, due to the charge trapping on the oxide surface and in the bulk oxide, while the APTES passivated FET only has a single exponential transient due to the bulk oxide. The results demonstrate that APTES is a good SiO₂ surface passivation layer to reduce trap states while maintaining a hydrophilic surface, pointing out the importance of dielectric surface passivation to bridge the gap between soft materials and electronic devices.

4.2 Introduction

Organic Electronics is an emerging area both for fundamental research and industrial applications.¹⁻⁴ Compared to their inorganic counterparts, organic semiconductors are often low cost, solution processable and environmentally friendly, with applications in large area electronics including FETs, solar cells, light emitting diodes, and radio frequency identification tags.¹⁻⁷ More recently, organic semiconductors have found applications in biosensors and bioelectronics.^{8,9}

The bottleneck in the performance of most organic electronic devices is the relatively low charge carrier mobility, due to both the intrinsic charge carrier localization and hopping transport mechanism, and various defect-induced charge trapping effects.^{1-3,10-14} For FETs, the dielectric-organic semiconductor interface is crucial since the charge carriers are within a few nanometers of this interface. Unfortunately, one of the most widely used dielectric, SiO₂, is notorious for electron trapping, possibly due to bulk defects and surface hydroxyl groups.^{10,11} To reduce this charge trapping effect, various siloxane self-assembled monolayers (SAMs) (*e.g.* hexamethyldisilazane (HMDS) and octadecyltrichlorosilane (OTS)) have been used to passivate the SiO₂ surface.¹⁰⁻¹⁴ This approach, though effective in alleviating charge trapping and increasing conductivity, always results in a hydrophobic surface which is not compatible with some self-assembly (*e.g.* Langmuir Blodgett (LB) deposition) and biosensing techniques.¹⁵

To quantitatively characterize charge trapping effects and understand the trapping mechanism, the density of electronic states (DOS), which reveals the charge carrier's energy dispersion, is fundamentally important. The localized trap states are often in the HOMO-LUMO gap of the organic semiconductors, which has been measured by various techniques including ultraviolet

photoelectron spectroscopy,¹⁶ transient photovoltage spectroscopy,¹⁷ and KPFM.¹⁸ Among these techniques, KPFM allows for a quantitative direct determination of DOS with spatial resolution down to 20 nm. Moreover, it's suitable for measuring the DOS of the organic semiconductor channel on top of the dielectric surface on an FET, which is directly relevant to device performance.

Here we present results obtained using KPFM to study the charge trapping behavior of an oligothiophene monolayer FET. The schematic setup of the measurement is shown in Figure 4.1a,b, where the only difference between 1b and 1a being the pre-adsorption of an APTES self-assembled monolayer on the SiO₂. The FET channel is a submonolayer of an oligothiophene derivative, named 4-(5-decyl-2,2',5',2'',5'',2''',5''',2''''-pentathiophen-5-yl)butyric acid (Figure 4.1c), abbreviated as D5TBA.¹⁹⁻²² This molecule has a semiconducting core consisting of five thiophene rings, which is widely used for molecular electronics.²³⁻²⁵ Moreover, it is amphiphilic with a hydrophilic carboxylic acid group at one end and a hydrophobic alkyl chain at the other end, thus is a good model system for self-assembly at air-water interface. KPFM reveals spatial inhomogeneity of the D5TBA surface potential distribution, which correlates with the structure of the monolayer film. Our spectroscopic measurements show that the HOMO edge level of the D5TBA is 0.2 eV below the Au Fermi level, and that the D5TBA FET is p-type, in agreement with previous conductive AFM measurements in our group.^{19,22} For the non-passivated FET, we observe mid-gap trap states with a Gaussian peak at 1.07 eV above the HOMO edge present at D5TBA-SiO₂ interface. After APTES passivation, these states are greatly reduced, resulting in an exponentially decaying DOS in the bandgap. Furthermore, we performed time-resolved local surface potential measurements on D5TBA crystalline domains on top of the non-passivated and APTES-passivated FET, revealing that the non-passivated FET has a larger hysteresis. To the best of our knowledge, this is the first report on SiO₂ surface passivation with hydrophilic SAM that successfully reduces charge traps. These results could be interesting for the interdisciplinary areas of soft materials and electronics, such as self-assembled organic electronics and bio-electronic interfaces.

4.3 Imaging Charge Transport Pathways in Semiconductor Organic Monolayers

The FET substrate was fabricated using a standard photolithography process, with a thermal oxide thickness $t_{ox} = 300 \text{ nm}$, channel length $L = 20 \mu\text{m}$, and width $W = 1 \text{ mm}$. The D5TBA monolayers deposited from the Langmuir-Blodgett trough attach to both the oxide and the Au surface *via* the carboxylic acid end group, while the C10 alkyl chain stays on top, rendering the surface completely hydrophobic (as confirmed by water contact angle measurements). The D5TBA FET was stored in an Ar glove box for at least 24 hours before KPFM measurements, so as to remove most of the water. KPFM was performed using an Agilent 5500 AFM with a home-built Kelvin probe setup. In order to achieve high spatial and energetic resolution, we implemented single pass frequency modulation method for the Kelvin probe feedback loop²⁶. With this setup we can measure the surface potential V_{sf} with 20 nm spatial resolution and 20 mV potential resolution. The KPFM measurements were performed at room temperature in a Nitrogen chamber with relative humidity < 0.5% (the detection limit of our hygrometer). During the surface potential measurements the Au source and drain electrodes (shown in Figure 4.1a,b) were grounded, while the gate bias V_g is varied within the range of -100 V to 100 V. It should be noted that we operated the FET in the static field effect capacitor regime, since no source-drain

bias was applied. Assuming that the channel potential is uniform across the vertical cross section of the FET channel, and the thermal broadening of the Fermi-Dirac distribution at room temperature is negligible compared to the energy scale of the measurement,^{27,28} we can use a simple parallel plate capacitor model to extract the carrier density in the channel:

$$N = \frac{C_{ox}}{t_c q} [(V_g - V_t) - V_{sf}], \quad (4.1)$$

where C_{ox} is the oxide capacitance per unit area, t_c is the channel thickness, q is the elementary charge, and V_t is the threshold gate voltage for charge carrier injection into channel (the origin of the x-axis in Figure 4.3a,d). We can write the energy level of the channel as the difference between the vacuum level and Fermi level, which is simply:

$$E = qV_{sf}. \quad (4.2)$$

The DOS can be obtained as:

$$\frac{dN}{dE} = \frac{C_{ox}}{t_c q^2} \left(\frac{1}{\frac{dV_{sf}}{dV_g}} - 1 \right). \quad (4.3)$$

It should be noted that the D5TBA monolayer channel in our FETs is only 1.5nm thick, as determined by AFM measurements. This ultrathin monolayer channel ensures minimum band bending in the vertical cross section of the channel, allowing the technique to reach its limit in terms of the accuracy and range of the extracted DOS.^{27,28}

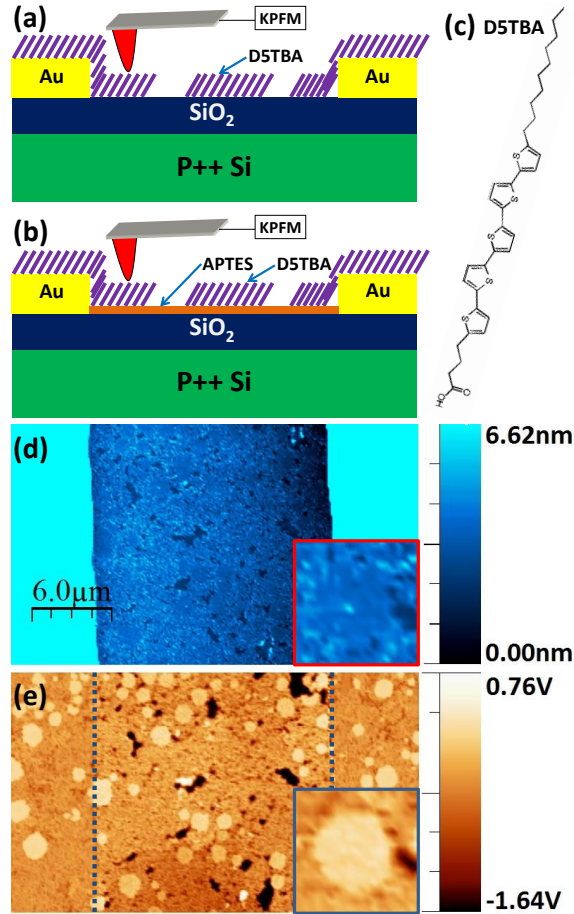


Figure 4.1. Schematic setup of the KPFM measurement, with the tip above a D5TBA monolayer domain on a FET (a) without oxide surface passivation (b) with APTES passivation. (c) Molecular structure of 4-(5-decyl-2,2',5',2'',5'',2''',5''',2''''-pentathiophen-5-yl) butyric acid (D5TBA). Simultaneous (d) topography and (e) surface potential images of a non-passivated D5TBA FET. The gate bias is -13V. The blue dotted lines in (e) mark the position of the Au-SiO₂ interface. Note that the Au electrodes in (d) (cyan colored) are actually 50nm above the oxide in the middle with the height color scale saturated, while in (e) the crystalline domains of D5TBA monolayer are clearly distinguishable both on Au and on oxide. The insets in the bottom right corners of (d) and (e) are expanded images of one area on the oxide.

Figure 4.1d,e show the simultaneous topography and surface potential images of the non-passivated D5TBA submonolayer FET, with no oxide surface passivation and a gate bias of -13 V. The Au source/drain electrodes are 50 nm thick, and the contrast of the topography image is adjusted to show the D5TBA monolayer structure on oxide. Note that the color scale is saturated over the electrodes. Since the surface of the oxide has a roughness of about half nm, the topography of the D5TBA on the oxide, though resolvable, is not very clear. On the other hand, the surface potential image clearly resolves different structures of the D5TBA monolayer film on both Au electrodes and the oxide surface. The D5TBA forms both crystalline domains (brighter, smooth islands) and amorphous domains, consistent with previous studies in our group.²² Expanded topographic and surface potential images of an island on the SiO₂ are shown in the insets of Figure 4.1d,e. A detailed analysis of more than 20 surface potential images on different areas and different samples show that the D5TBA monolayer always has a higher surface potential (lower work function) than the substrate. This is due to the fact that the negatively charged carboxylic end of the D5TBA is down in contact with the surface, while the positively charged alkyl chain end is on top. On the Au electrodes, the average surface potential of the crystalline domains is 250 mV above that of Au, while the amorphous domains have an average surface potential 200 mV above that of Au. We suspect that the amorphous domains could be less densely packed than the crystalline domains, resulting in a smaller electric dipole moment. This could also be an explanation to the fact that no lateral charge transport through the amorphous domains has been observed by previous Conductive AFM studies in our group.^{19,22} In this study we focus on the crystalline domains.

To understand the surface potential contrast shown in Figure 4.1e, we zoom in to the Au-SiO₂ interface to analyze the correlation between topographic structure and surface potential, and the dependence of surface potential distribution on gate bias. Figure 4.2 shows the simultaneous topography (Figure 4.2a, c) and surface potential (Figure 4.2b, d) measurements with negative and positive gate biases, respectively. In Figure 4.2b we can see that there is a D5TBA monolayer island straddling the Au and the SiO₂. When $V_g = -13$ V, the surface potential of the D5TBA on SiO₂ is only slightly (100 mV) below the surface potential of D5TBA on Au electrode (Figure 2b). But when $V_g = 6$ V, the surface potential of the D5TBA on SiO₂ is 1.1 V above that of the D5TBA on Au (Figure 4.2d). This indicates that with negative gate bias, hole carriers can be injected into the D5TBA channel (*i.e.* the part of the D5TBA island on SiO₂ in electrical contact with the Au). The injected hole carriers effectively screen the gate bias, so that the surface potential of the channel remains close to the surface potential of the source/drain electrodes. When positive gate bias is applied, the hole carriers in the channel are depleted while no electrons are injected, so that the channel becomes insulating and follows the gate bias. These

results lead to the conclusion that the D5TBA FET is p-type. Note that the surface potential is noisy within about 100 nm of the SiO₂-Au interface, due to a sharp transition of the topography which perturbs the feedback loop of the KPFM, when the AFM tip scans across the interface.²⁶ But the KPFM feedback is stable farther away from the interface. Also, the topography images in Figure 4.2a and 4.2c are identical, indicating that the KPFM technique successfully eliminates the contribution of electrostatic tip-sample interaction to the topography defects, which exists for normal tapping mode and non-contact AFMs without Kelvin probe feedback.²⁹⁻³¹ Moreover, as indicated before, we can see that the surface potential of the D5TBA crystalline island on Au is 250 mV above that of the Au, in both Figure 4.2b and 4.2d.

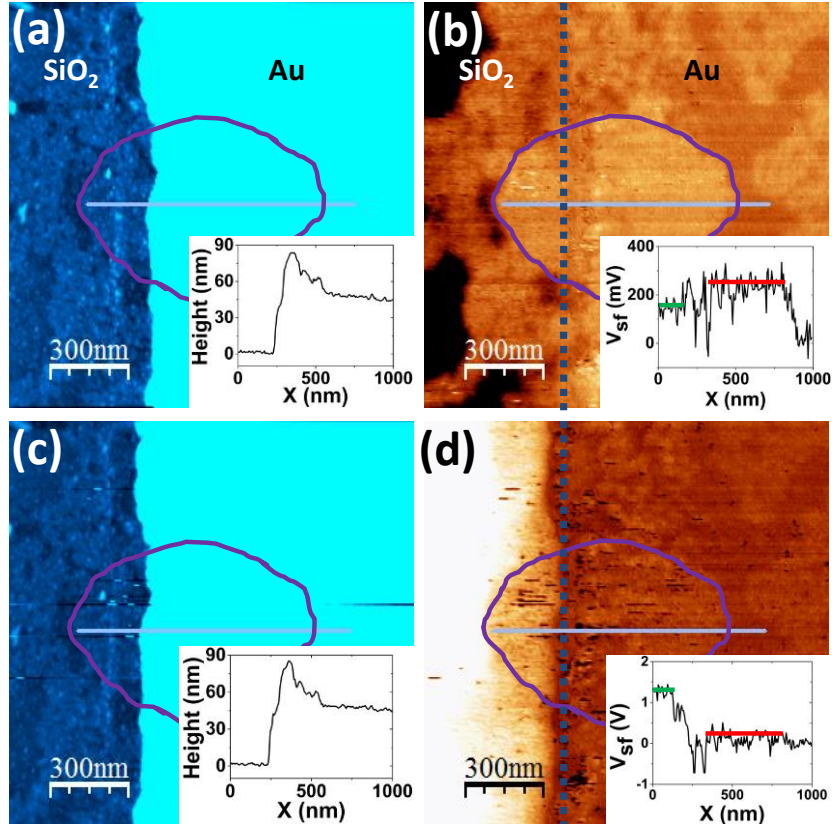


Figure 4.2. Simultaneous topography (left) and surface potential images (right) of non-passivated D5TBA FET. The top images correspond to a gate voltage of $V_g = -13$ V, while the bottom images correspond to $V_g = 6$ V. The crystalline monolayer island across the oxide-Au interface is outlined in all the images. The insets show the height and surface potential distributions across the line on this island. The green and red lines in the inset images mark the surface potential level of the D5TBA on SiO₂ and D5TBA on Au, respectively. The blue dotted lines in (b) and (d) show the SiO₂-Au interface, as guidance to the eye.

4.4 Charge Trapping States Probed by Surface Potential Spectroscopy

To quantitatively characterize the dependence of surface potential on gate bias and extract the bandgap DOS, we perform $V_{sf} - V_g$ spectroscopy on the crystalline channel region of the non-passivated D5TBA FET, as shown in Figure 4.3a. After acquiring each $V_{sf} - V_g$ spectra the gate

bias was set to 0 V for a few minutes to allow the threshold voltage to equilibrate, before taking the next spectrum or image. During the gate bias sweep (at a speed of 10 – 20 mV/s for all the $V_{sf} - V_g$ spectroscopy measurements), the tip is within 10nm above the point at the D5TBA island on the oxide, marked by the cross in the inset of Figure 3a. It can be seen that the surface potential linearly follows the gate bias when $V_g - V_t > 0$, confirming that the D5TBA is not electron-conducting. In the linear region the slope is 0.6, a value less than 1 due possibly to charge trapping hysteresis. When $V_g - V_t$ is below 0, the surface potential remains stable until $V_g - V_t$ reaches -18V, at which point V_{sf} decreases further until reaching a constant value at $V_{sf} = -0.4$ V. This clearly shows that the hole carriers are injected into the channel, which screen the gate bias. Using Equation 3 we can extract the DOS, as plotted in Figure 4.3b. We can see that the valence band edge DOS is exponential ($DOS \propto \exp(-E/E_0)$) with a characteristic energy $E_0 = 0.12$ eV, in agreement with previous studies of organic FETs.^{18,27} However, the DOS does not decay exponentially all the way into the bandgap region. Instead, we observe additional DOS with a Gaussian peak centered at 0.87 eV with a DOS of $3.4 \times 10^{19} \text{eV}^{-1} \text{cm}^{-3}$ and a FWHM of 0.15 eV. The bandgap of D5TBA can be estimated from the UV-Vis absorption edge to be 2.5 eV. If we take the Au work function to be 5.1 eV, then the HOMO and LUMO edge of the D5TBA is 5.3 eV and 2.8 eV below vacuum level, respectively. The peak of the midgap trap states is very deep at about 4.2 eV below vacuum level which is unlikely due to the electrochemically induced impurities in the D5TBA.³² We suspect that the hydroxyl groups on the SiO_2 surface are the origin of the deep electron traps (Figure 4.3c).

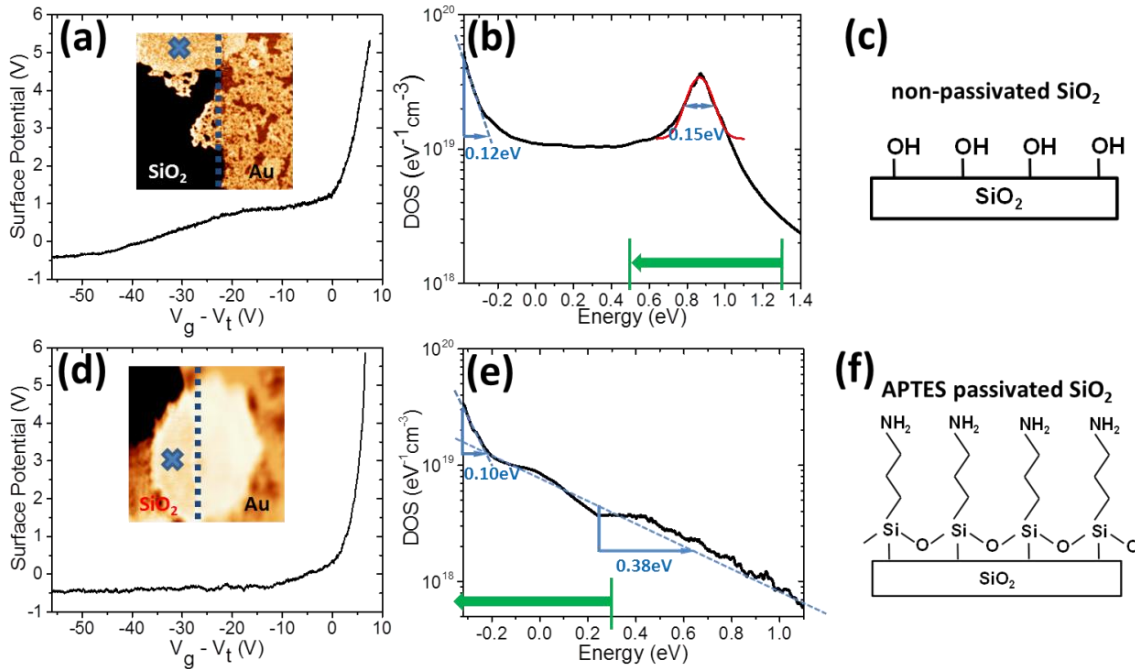


Figure 4.3. Surface potential – gate bias spectroscopy of D5TBA FET (a) without oxide surface passivation and (d) with APTES passivation of SiO_2 . V_{sf} is calibrated by setting the Au surface potential to zero. The insets in (a) and (d) are $3 \mu\text{m} \times 3 \mu\text{m}$ surface potential images with $V_g - V_t = -13\text{V}$, where the Au-oxide interface is marked with blue dotted lines, and the point at which the $V_{sf} - V_g$ spectroscopy is performed is marked by crosses. The gate bias is swept from positive to negative, with a speed of 10 – 20 mV/s. (b) and (e) show the corresponding DOS of the D5TBA FET without and with APTES passivation of the SiO_2 . (c) and (f): schematic surface

structure of the SiO₂ before D5TBA deposition. While the non-passivated SiO₂ surface has OH groups (c), the APTES passivation eliminates the OH groups leaving a surface terminated with NH₂ groups (f). The red curve in (b) is a Gaussian fit of the DOS peak between 0.64 eV – 1.10 eV, centered at 0.87 eV with a FWHM of 0.15 eV. The exponentially decaying parts of the DOS in (b) and (e) are marked with dashed lines, with their characteristic energy indicated. The green lines and arrows in (b) and (e) show the start and end positions of the surface energy level (corresponding to $V_g = V_t$ and $V_t - 26V$, respectively) in the transient surface potential measurements shown in Figure 4.4b and 4.4c, respectively.

With the goal of understanding the nature of the midgap traps and eliminating them, we deposited a monolayer of APTES on the FET substrate, after which D5TBA was deposited. The ethoxy groups of the APTES react with the hydroxyl groups on the oxide to form covalent -Si-O-Si- bonds (Figure 4.3f). To confirm the successful deposition of APTES, we deposited APTES on pure SiO₂, and measured a water contact angle to be 62°. Furthermore, with X-ray photoelectron spectroscopy (XPS) we found a Nitrogen 1s peak at 400.1 eV. AFM measurements confirm that the surface is smooth with a uniform APTES coverage. The same $V_{sf} - V_g$ spectroscopy is performed on the APTES passivated D5TBA FET and the DOS is extracted in the same manner as before. The results are shown in Figure 4.3d,e. Again the point at which the tip is located is marked by the cross in the inset of Figure 4.3d. The slope of the $V_{sf} - V_g$ curve in the linear region $V_g - V_t > 0$ is 1.0, indicating negligible hysteresis effect in this case. When $V_g - V_t < 0$, the surface potential decreases slowly until reaching the valence band at $V_{sf} = -0.4$ V. The DOS curve in Figure 3e clearly reveals that the midgap DOS peak in the non-passivated FET is eliminated. With the APTES passivation, the valence band edge DOS contains an exponential short tail up to -0.2 eV with a characteristic energy of 0.10 eV, while the bandgap DOS is a long exponential tail with a characteristic energy of 0.38 eV. Since there is an exponential DOS tail with similar characteristic energy from -0.4 eV to -0.2 eV for both non-passivated and APTES passivated FET, we can infer that these states could be attributed to the intrinsic HOMO level broadening due to defects of the D5TBA monolayer or to inter-molecular electronic coupling effects. The mid-gap states around 0.9 eV in the Gaussian peak of the non-passivated FET can be attributed to the -OH groups on the SiO₂ surface, while the 0.38 eV exponential decay of the passivated FET can be attributed to charge trapping in the bulk oxide. This was proposed to be due to proton migration.³³⁻³⁵

4.5 Time-Resolved Surface Potential Spectroscopy

In addition to the quasi-static DOS measurements with very slow gate bias sweeping, we further performed dynamic transient surface potential measurements. The time constant of our KPFM feedback loop is about 5 ms, which sets the resolution of the time scale for the transient measurements. The schematic of the measurement is shown in Figure 4.4a. At time zero, the gate bias is suddenly switched from V_t to $V_t - 26V$. This corresponds to a depletion of electrons in the spectral region from 1.3 eV to 0.5 eV for the non-passivated D5TBA FET, which covers the Gaussian trap states, as shown by the green lines and arrows in Figure 4.3b; While for the APTES passivated FET, it corresponds to electron depletion from 0.3 eV to -0.4 eV (which is inside the HOMO band), as shown by the green line and arrow in Figure 4.3e. Using Equation 1, we can estimate that the amount of depleted electron density (with gate bias sweep from V_t to $V_t - 26$ V) for the non-passivated and passivated FETs are $2.1 \times 10^{19} \text{ cm}^{-3}$ and $2.0 \times 10^{19} \text{ cm}^{-3}$

correspondingly, which are very close. The surface potential transients are recorded at the same location as marked by the crosses in Figure 4.3a,d. The results for non-passivated and APTES passivated FET are shown in Figure 4.4b,c. At $t = 0$ s the surface potential is usually saturated to -10 V (the lower limit of our KPFM surface potential measurements), so we choose to start recording the surface potential beginning at $t = 0.2$ s for all the transient measurements. We can see that the initial surface potential at $t = 0.2$ s is around 6 V below the steady state surface potential for the non-passivated FET. After APTES passivation, the initial surface potential is about 1 V below the steady state surface potential, almost 6 times smaller. Moreover, we can see that the surface potential transient of the APTES passivated FET fits well with a single exponential decay ($V_{sf} = V_{sf0} + Ae^{-t/\tau}$) with a time constant $\tau = 0.8$ s, while the transient of the non-passivated FET contains a fast decay in the beginning followed by a slow tail that does not fit with a single exponential. Instead, it fits well with a sum of two exponentials ($V_{sf} = V_{sf0} + A_1e^{-t/\tau_1} + A_2e^{-t/\tau_2}$). If we fix the time constant of one exponential to be $\tau_1 = 0.8$ s, then the time constant of the other exponential is fitted to be $\tau_2 = 6.2$ s. Compared with the DOS results shown before, we can attribute the 0.8 s decay in both the non-passivated and passivated FETs to the charge trapping in the bulk oxide, while attributing the 6.2 s slow decay to the surface -OH group related trap states on the non-passivated FET.

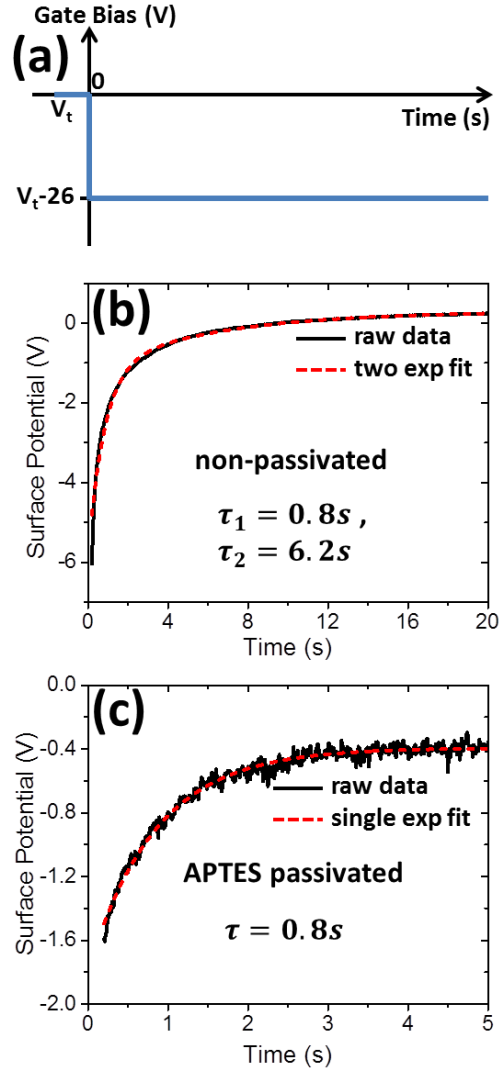


Figure 4.4. Transient surface potential spectra. (a) Schematic showing the gate bias step function from V_t to $V_t - 26$ V at time 0. For the non-passivated D5TBA FET, $V_g = V_t$ and $V_t - 26$ V correspond to $V_{sf} = 1.3$ V and 0.5 V, respectively, as shown by the green lines in Figure 4.3b. For the APTES passivated D5TBA FET, it corresponds to $V_{sf} = 0.3$ V and -0.4 V, respectively, as shown by the green line and arrow in Figure 4.3e. The surface potential is recorded from $t = 0.2$ s until it becomes stable, as shown in (b) for non-passivated FET and (c) for APTES passivated FET. The black and red-dashed curves are raw data and exponential fits, respectively. While the transient surface potential curve for the APTES passivated FET can be fitted well with a single exponential decay with amplitude $A = -1.4$ V and time constant $\tau = 0.8$ s, the transient of the non-passivated FET requires a fit with a sum of two exponentials, with amplitudes $A_1 = -4.7$ V, and $A_2 = -1.5$ V, and time constants $\tau_1 = 0.8$ s, and $\tau_2 = 6.2$ s.

The transient surface potential measurements were performed at different spots on the channel region of several different D5TBA crystalline islands on both the non-passivated and APTES passivated FETs, with reproducible results, regardless of the distance from the measurement spot to the source/drain electrode. This means that the surface potential transients are due to the local capacitive charge trapping behavior instead of the contact resistance (which varies for different

D5TBA islands²⁰) or the resistance due to the domain boundaries of the D5TBA, and that the charge traps are uniformly distributed in the D5TBA crystalline islands (on the oxide). Furthermore, our previous study shows that the contact resistance of a non-planar D5TBA FET is of the order of $100\text{ G}\Omega$.²⁰ If we estimate that the area of a D5TBA island is $1\ \mu\text{m}^2$, the corresponding oxide capacitance would be around $1 \times 10^{-16}\text{ F}$, and the RC time constant would be in the scale of $10\ \mu\text{s}$. This again indicates that the contact resistance is not causing the observed surface potential hysteresis which is in the scale of seconds.

4.6 Conclusion

In conclusion, we have used Kelvin probe force microscopy to measure the surface potential distribution across D5TBA submonolayer FET. Surface potential – gate bias spectroscopy is performed at local spots on the D5TBA channel of the non-passivated and APTES passivated FET, from which the density of bandgap electronic states is extracted. Our results show that the non-passivated FET has a large density of trap states with a Gaussian distribution peaking at 4.2 eV below the vacuum level. This Gaussian peak is eliminated after APTES passivation. Furthermore, we performed transient surface potential measurements showing that the non-passivated FET has a much larger charge trapping hysteresis than the APTES passivated FET. These results demonstrate that the gate oxide contains charge trap states located in the bulk and states located at the surface, likely in the –OH groups. We further demonstrate that the surface states can be eliminated by suitable passivation with APTES while the bulk states remain unmodified. Our results also demonstrate that KPFM is a promising tool to characterize local charge trapping behavior of weakly conducting semiconductor thin films with strong charge carrier localization.

4.7 Methods Summary

Fabrication of FET: Heavily doped p++ Si(100) wafer with 300 nm thermal oxide is purchased from Addison Engineering, Inc. The p++ silicon is used as gate. Subsequent source/drain electrode fabrication is done in the nanolab at UC Berkeley. Specifically, UV photolithography is used to pattern the substrate, after which 5 nm Ti and 50 nm Au is deposited and photoresist lift-off is done using acetone. The fabricated wafer is cleaved into $1\text{ cm} \times 1\text{ cm}$ pieces, each containing about 50 FETs. Afterwards these pieces are sonicated in Acetone (10 min) and IPA (10 min), and oxygen plasma cleaned for 1 min. These clean FET substrates are used for either direct Langmuir-Blodgett deposition of D5TBA or APTES deposition and subsequent LB deposition of D5TBA.

APTES deposition: The cleaned FET substrates are immersed in a solution of APTES in toluene (10 mM) for 2 hours within a closed jar in a nitrogen glove box at room temperature. Subsequently, they are washed by sonication in toluene three times (2 min each). The dried APTES-modified substrates are then stored for 2 hours in an oven at $130\text{ }^\circ\text{C}$ before being stored under vacuum to remove residual solvent.

References

1. Horowitz G. Organic Field-Effect Transistors. *Adv. Mater.* **1998**, *10*, 365–377.

2. Liscio F.; Albonetti C.; Broch K.; Shehu A.; Quiroga S. D.; Ferlauto L.; Frank C.; Kowarik S.; Nervo R.; Gerlach A.; *et al.* Molecular Reorganization in Organic Field-Effect Transistors and Its Effect on Two-Dimensional Charge Transport Pathways. *ACS Nano* **2013**, *7*, 1257–1264.
3. Sirringhaus H. Device Physics of Solution-Processed Organic Field-Effect Transistors. *Adv. Mater.* **2005**, *17*, 2411–2425.
4. Liu W.; Jackson B. L.; Zhu J.; Miao C. –Q.; Chung C. –H.; Park Y. –J.; Sun K.; Woo J.; Xie Y. –H. Large Scale Pattern Graphene Electrode for High Performance in Transparent Organic Single Crystal Field-Effect Transistors. *ACS Nano*, **2010**, *4*, 3927–3932.
5. Jiang Y.; Qiong Q.; Wang R.; Zhang J.; Xue Q.; Wang C.; Jiang C.; Qiu X. Direct Observation and Measurement of Mobile Charge Carriers in a Monolayer Organic Semiconductor on a Dielectric Substrate. *ACS Nano*, **2011**, *5*, 6195–6201.
6. Forrest S. R. The Path to Ubiquitous and Low-Cost Organic Electronic Appliances on Plastic. *Nature* **2004**, *428*, 911–918.
7. Guilbert A. A. Y.; Reynolds L. X.; Bruno A.; MacLachlan A.; King S. P.; Faist M. A.; Pires E.; Macdonald J. E.; Stingelin N.; Haque S. A.; *et al.* Effect of Multiple Adduct Fullerenes on Microstructure and Phase Behavior of P3HT: Fullerene Blend Films for Organic Solar Cells. *ACS Nano*, **2012**, *6*, 3868–3875.
8. Berggren M.; Richter-Dahlfors A. Organic Bioelectronics. *Adv. Mater.* **2007**, *19*, 3201–3213.
9. Hammock M. L.; Knopfmacher O.; Naab B. D.; Tok J. B.-H.; Bao Z. Investigation of Protein Detection Parameters Using Nanofunctionalized Organic Field-Effect Transistors. *ACS Nano*, **2013**, *7*, 3970–3980.
10. Chua L. –L.; Zaumseil J.; Chang J. –F.; Ou E. C. –W.; Ho P. K. –H.; Sirringhaus H.; Friend R. H. General Observation of N-Type Field-Effect Behaviour in Organic Semiconductors. *Nature* **2005**, *434*, 194–199.
11. Mathijssen S. G. J.; Kemerink M.; Sharma A.; Cölle M.; Bobbert P. A.; Janssen R. A. J.; de Leeuw D. M. Charge Trapping at the Dielectric of Organic Transistors Visualized in Real Time and Space. *Adv. Mater.* **2008**, *20*, 975–979.
12. Bolsée J. –C.; Manca J. Effects of Hole and Electron Trapping on Organic Field-Effect Transistor Transfer Characteristic. *Synth. Met.* **2011**, *161*, 789–793.
13. Tanidaa S.; Noda K.; Kawabata H.; Matsushige K. Investigation of Electron Trapping Behavior in N-Channel Organic Thin-Film Transistors with Ultrathin Polymer Passivation on SiO₂ Gate Insulator. *Synth. Met.* **2010**, *160*, 1574–1578.
14. Mathijssen S. G. J.; Spijkman M. –J.; Andringa A. –M.; van Hal P. A.; McCulloch I.; Kemerink M.; Janssen R. A. J.; de Leeuw D. M. Revealing Buried Interfaces to Understand the Origins of Threshold Voltage Shifts in Organic Field-Effect Transistors. *Adv. Mater.* **2010**, *22*, 5105–5109.
15. Chaki N. K.; Vijayamohanan K. Self-Assembled Monolayers as a Tunable Platform for Biosensor Applications. *Biosens. Bioelectron.* **2002**, *17*, 1–12.
16. Sueyoshi T.; Fukagawa H.; Ono M.; Kera S.; Ueno N. Low-Density Band-Gap States in Pentacene Thin Films Probed with Ultrahigh-Sensitivity Ultraviolet Photoelectron Spectroscopy. *Appl. Phys. Lett.* **2009**, *95*, 183303.
17. O'Regan B. C.; Scully S.; Mayer A. C.; Palomares E.; Durrant J. The Effect of Al₂O₃ Barrier Layers in TiO₂/Dye/CuSCN Photovoltaic Cells Explored by Recombination and DOS Characterization Using Transient Photovoltage Measurements. *J. Phys. Chem. B* **2005**, *109*, 4616–4623.

18. Tal O.; Rosenwaks Y.; Preezant Y.; Tessler N.; Chan C. K.; Kahn A. Direct Determination of the Hole Density of States in Undoped and Doped Amorphous Organic Films with High Lateral Resolution. *Phys. Rev. Lett.* **2005**, *95*, 256405.
19. Hendriksen B. L. M.; Martin F.; Qi Y.; Mauldin C.; Vukmirovic N.; Ren J.; Wormeester H.; Katan A. J.; Altoe V.; Aloni S.; *et al.* Electrical Transport Properties of Oligothiophene-Based Molecular Films Studied by Current Sensing Atomic Force Microscopy. *Nano Lett.* **2011**, *11*, 4107–4112.
20. Martin F.; Hendriksen B.; Katan A.; Ratera I.; Qi Y.; Harteneck B.; Liddle J. A.; Salmeron M. Ultra-Flat Coplanar Electrodes for Controlled Electrical Contact of Molecular Films. *Rev. Sci. Instrum.* **2011**, *82*, 123901.
21. Altoe V.; Martin F.; Katan A.; Salmeron M.; Aloni S. Electron Microscopy Reveals Structure and Morphology of One Molecule Thin Organic Films. *Nano Lett.* **2012**, *12*, 1295–1299.
22. Martin F.; Hendriksen B. L. M.; Katan A. J.; Qi Y.; Mauldin C.; Fréchet J. M. J.; Salmeron M. Sensitivity to Molecular Order of the Electrical Conductivity in Oligothiophene Monolayer Films. *Langmuir* **2013**, *29*, 1206–1210.
23. Smits E. C. P.; Mathijssen S. G. J.; van Hal P. A.; Setayesh S.; Geuns T. C. T.; Mutsaers K. A. H. A.; Cantatore E.; Wondergem H. J.; Werzer O.; Resel R.; *et al.* Bottom-Up Organic Integrated Circuits. *Nature* **2008**, *455*, 956–959.
24. Garnier F.; Yassar A.; Hajlaoui R.; Horowitz G.; Deloffre F.; Servet B.; Ries S.; Alnot P. Molecular Engineering of Organic Semiconductors: Design of Self-Assembly Properties in Conjugated Thiophene Oligomers. *J. Am. Chem. Soc.* **1993**, *115*, 8716–8721.
25. Halik M.; Klauk H.; Zschieschang U.; Schmid G.; Ponomarenko S.; Kirchmeyer S.; Weber W. Relationship Between Molecular Structure and Electrical Performance of Oligothiophene Organic Thin Film Transistors. *Adv. Mater.* **2003**, *15*, 917–922.
26. Li G.; Mao B.; Lan F.; Liu L. Practical Aspects of Single-Pass Scan Kelvin Probe Force Microscopy. *Rev. Sci. Instrum.* **2012**, *83*, 113701.
27. Celebi K.; Jadhav P. J.; Milaninia K. M.; Bora M.; Baldo M. A. The Density of States in Thin Film Copper Phthalocyanine Measured by Kelvin Probe Force Microscopy. *Appl. Phys. Lett.* **2008**, *93*, 083308.
28. Roelofs W. S. C.; Mathijssen S. G. J.; Janssen R. A. J.; de Leeuw D. M.; Kemerink M. Accurate Description of Charge Transport in Organic Field Effect Transistors Using an Experimentally Extracted Density of States. *Phys. Rev. B* **2012**, *85*, 085202.
29. Sadewasser S.; Carl P.; Glatzel; T.; Lux-Steiner M. C. Influence of Uncompensated Electrostatic Force on Height Measurements in Non-Contact Atomic Force Microscopy. *Nanotechnology* **2004**, *15*, S14–S18.
30. Ziegler D.; Naujoks N.; Stemmer A. Feed-Forward Compensation of Surface Potential in Atomic Force Microscopy. *Rev. Sci. Instrum.* **2008**, *79*, 063704.
31. Ziegler D.; Rychen J.; Naujoks N.; Stemmer A. Compensating Electrostatic Forces by Single-Scan Kelvin Probe Force Microscopy. *Nanotechnology* **2007**, *18*, 225505.
32. Nicolai H. T.; Kuik M.; Wetzelaer G. A. H.; de Boer B.; Campbell C.; Risko C.; Brédas J. L.; Blom P. W. M. Unification of Trap-Limited Electron Transport in Semiconducting Polymers. *Nat. Mater.* **2012**, *11*, 882–887.
33. Sharma A.; Mathijssen S. G. J.; Smits E. C. P.; Kemerink M.; de Leeuw D. M.; Bobbert P. A. Proton Migration Mechanism for Operational Instabilities in Organic Field-Effect Transistors. *Phys. Rev. B* **2010**, *82*, 075322.

34. Bobbert P. A.; Sharma A.; Mathijssen S. G. J.; Kemerink M.; de Leeuw D. M. Operational Stability of Organic Field-Effect Transistors. *Adv. Mater.*, **2012**, *24*, 1146–1158.
35. Ausserlechner S. J.; Gruber M.; Hetzel R.; Flesch H. –G.; Ladinig L.; Hauser L.; Haase A.; Buchner M.; Resel R.; Schürer F.; *et al.* Mechanism of Surface Proton Transfer Doping in Pentacene Based Organic Thin-Film Transistors. *Phys. Status Solidi A* **2012**, *209*, 181.
36. Horcas I.; Fernandez R.; Gomez-Rodriguez J. M.; Colchero J.; Gomez-Herrero J.; Baro A. M. WSXM: A Software for Scanning Probe Microscopy and a Tool for Nanotechnology. *Rev. Sci. Instrum.* **2007**, *78*, 013705.

Chapter 5: Atomic Insight of Defects in PbS Nanocrystals

Reproduced in part and adapted from a manuscript under review by Science Advances.

5.1 Abstract

Artificial solids composed of semiconductor quantum dots (QDs) are being developed for large area electronic and optoelectronic applications, but these materials often have defect-induced in-gap states (IGS) of unknown chemical origin. Here we performed scanning probe based spectroscopic analysis and density functional theory (DFT) calculations, to determine the nature of such states and their electronic structure. We found that IGS near the valence band occur frequently in the QDs except when treated with reducing agents. Calculations on various possible defects and chemical spectroscopy revealed that molecular oxygen is most likely at the origin of these IGS. We expect this impurity-induced deep IGS mechanism to be generally applicable to ionic semiconductors, where the intrinsic vacancy defects either do not produce IGS or produce shallow states near band edges. Ionic QDs with surface passivation to block impurity adsorption are thus ideal for high efficiency optoelectronic device applications.

5.2 Introduction

The evolution of semiconductor electronics and optoelectronics began with the controlled doping of impurity atoms into semiconductor crystals, which opened the way to engineer their charge transport properties (1). On the other hand, unwanted impurities or defects can hinder transport and limit device performance (2). The development of nanomaterials of controlled size made it possible to engineer the band gap and tune the electronic properties from the bottom up. As a trade-off, the impact of surface impurities on the electronic properties of nanomaterials is more prominent due to the large surface-to-volume ratio and strong quantum confinement effects (3–5). For colloiddally synthesized nanocrystals or quantum dots in particular, surface-related IGS are believed to assist the recombination of photoexcited charge carriers (6), which limits the optoelectronic device efficiency (7, 8). However, until now the nature of the IGS is still unclear. Tentative explanations include: non-stoichiometry of the constituent atoms (9), incomplete ligand passivation (7, 8, 10), surface oxidation (5), and charge-induced surface reconstruction (11). Despite all these efforts, there is still a lack of accurate measurements on the energy level of IGS and a lack of comprehensive theoretical calculation on the effect of various possible defects on the electronic structure of QDs. A consistent, thorough investigation on IGS involving both experiment and theory is thus urgently needed for the advancement of QDs in electronic applications.

We took a multi-scale approach to determine the chemical origin of IGS in PbS QDs, which is the active material in state of the art colloidal quantum dot solar cells (12, 13). Scanning tunneling spectroscopy (STS) and Kelvin probe force microscopy (KPFM) based surface potential spectroscopy (SPS) revealed the energetic position of IGS, whose chemical origin was explained by DFT calculations and further confirmed by X-ray photoelectron spectroscopy (XPS). This methodology for studying defects in QDs, with more degrees of complication than bulk single crystals explored by traditional surface science, is generally applicable to solution processed materials, such as organic thin films and perovskite materials. DFT calculations on the

QD systems consisting of as many as ~ 1000 atoms show good agreement with experimental results, paving the way for rational bottom-up design of functional materials.

5.3 Experimental Observation of In-Gap States

The PbS QDs studied here have an average diameter of 5.5 nm with ~ 0.9 eV band gap. Transmission electron microscopy and UV-Vis absorption spectroscopy results are shown in Figs. 5.1 & 5.2. As-synthesized colloidal QDs are typically capped with long insulating ligands (14). For lead chalcogenide (PbX, X=S, Se) QDs, various ligand exchange processes have been explored to reduce inter-particle distance and enable electron conduction in a QD solid. Here we explore treatments with 1,2-ethanedithiol (EDT), 3-mercaptopropionic acid (MPA) and hydrazine (HYD) that have been reported to produce ambipolar QD field effect transistors (FETs). The resulting QDs are labeled PbS-EDT, PbS-MPA and PbS-HYD, respectively. Infrared absorption reveals successful removal of the original oleate ligands, as shown in Fig. 5.3.

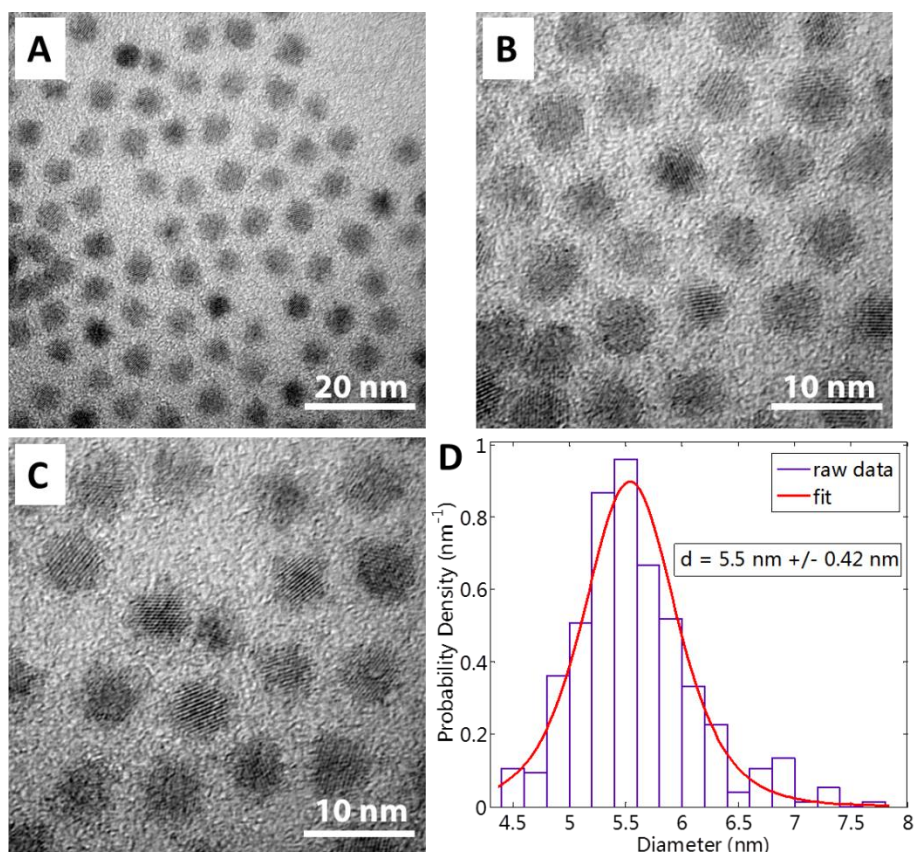


Figure 5.1. Size of the quantum dots. (A to C) TEM images of the PbS QDs capped with oleate. (D) Size distribution histogram of the QDs extracted from TEM images.

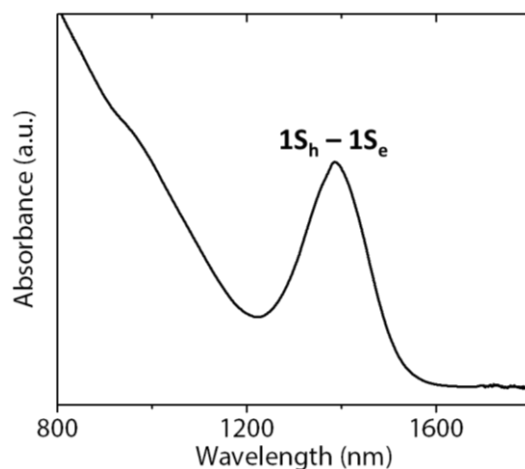


Figure 5.2. Optical absorption. UV-Vis absorption spectrum of PbS QDs capped with oleate. The peak at 1386 nm corresponds to $1S_h - 1S_e$ exciton transition, which reveals that the bandgap is ~ 0.9 eV.

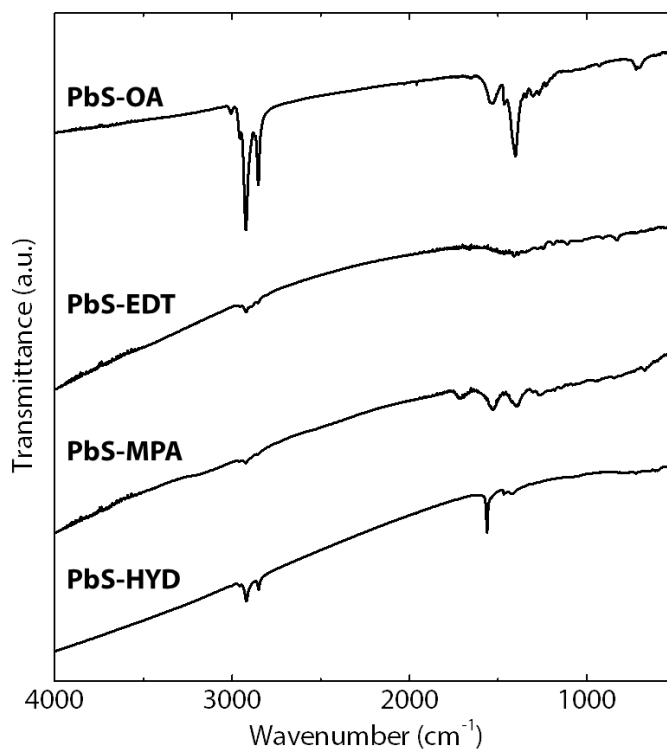


Figure 5.3. Infrared vibration. FTIR spectra of PbS QDs with different chemical treatments. PbS-OA denotes the untreated PbS QDs with oleate ligand, while PbS-EDT, PbS-MPA, PbS-HYD are EDT, MPA, and HYD treated PbS QDs, respectively.

Traditional methods to analyze IGS in semiconductor devices include transient photovoltage measurements, thermal admittance spectroscopy, and deep level transient spectroscopy (8, 15, 16). These techniques provide quantitative information on the concentration of IGS, but cannot determine the energy of the levels. Transient absorption and photocurrent spectroscopies can probe the optical transitions in QD solids (4, 7, 10, 16), but the correlation of the various transitions with IGS is not straightforward, considering the presence of multiple intra-band

transitions and vibrational absorption of the organic ligands (17). X-ray spectroscopy techniques can probe the energy level of electronic states, but the resolution is not high enough to resolve individual IGS peaks (18, 19). In order to directly resolve the energy level of IGS, we performed scanning tunneling spectroscopy (20–22) on individual PbS-EDT QDs deposited on indium tin oxide (ITO) substrate to obtain their electronic density of states (DOS). The QDs have submonolayer coverage (Fig. 5.4), convenient for performing control spectroscopy measurements on the metallic ITO substrate. STS results are shown in Fig. 5.5A. A heterogeneous distribution of DOS was observed on measurements over tens of QDs, with about half of them showing IGS. These states are 0.05–0.1 eV above the Fermi level and 0.15–0.3 eV above the $1S_h$ states (valence band). The actual percentage of QDs with IGS can be higher since STS is only sensitive to states localized on the top surface of the QD, or with wave functions that extend all the way to the surface. The position of the $1S_h$ states were found to have large fluctuations, but compared to the $1S_e$ states (conduction band) they are always closer to the Fermi level. This is in agreement with the previously observed p-type doping of EDT treated lead chalcogenide QDs (23, 24).

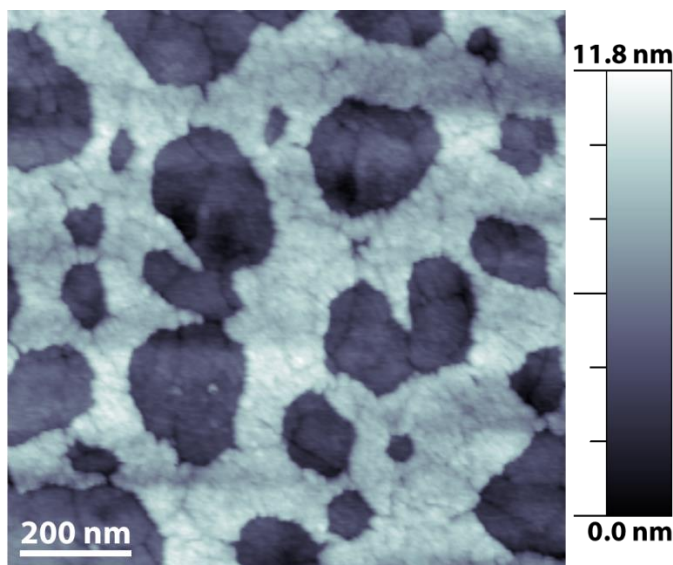


Figure 5.4. AFM image of the submonolayer PbS-EDT QDs on ITO substrate.

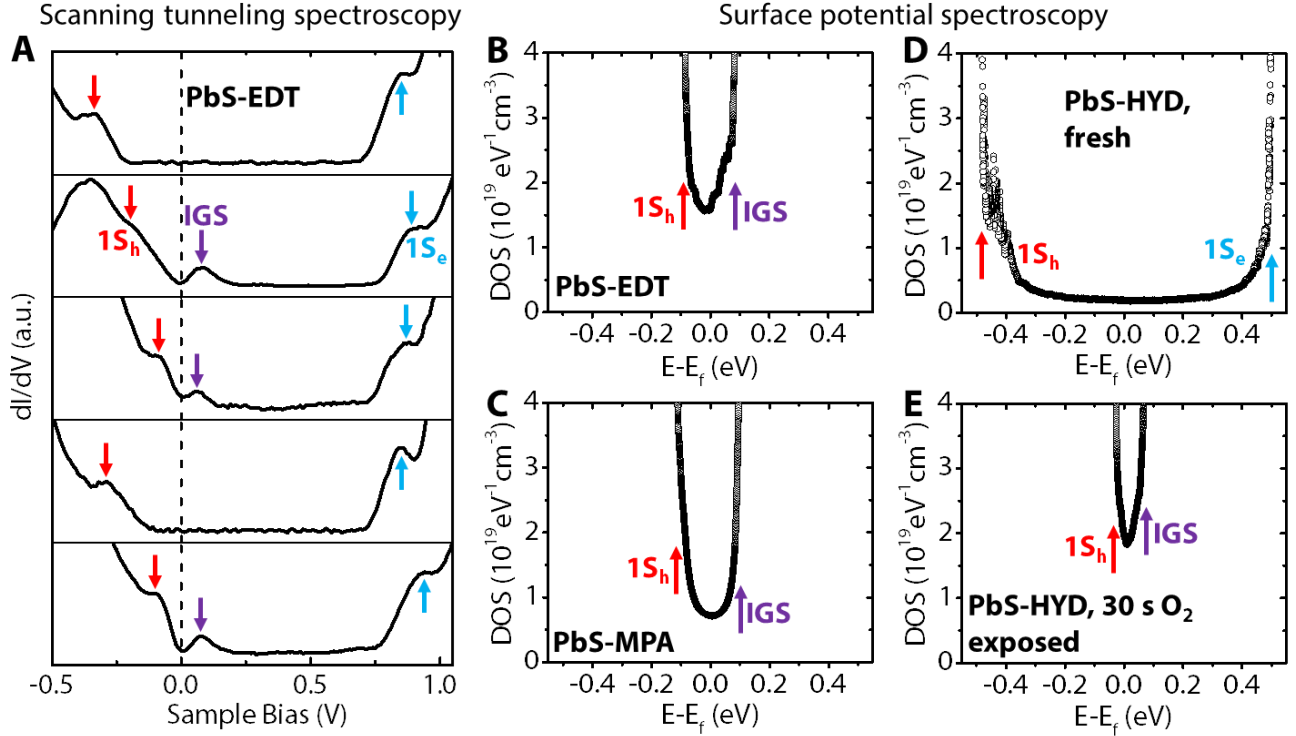


Figure 5.5. Experimental observation of IGS near the valence band. (A) Scanning tunneling spectroscopy (STS) curves of individual PbS-EDT QDs. The sample bias (in volts) corresponds to the energy level position with respect to the Fermi level (in eV). (B–E) Density of states (DOS) measured by surface potential spectroscopy of PbS QDs with different chemical treatments as labeled. E_f : Fermi level. All the observed IGS are empty states above the Fermi level.

Another technique we used to measure the energy level of IGS is KPFM, which probes the change of surface potential as a function of gate bias in a QD monolayer FET. Since the occupation of states is electrostatically tuned by the gate bias in an FET, we can use KPFM to extract the density of states. In a simple electrostatic model based on the planar capacitor geometry made by the gate and the QD monolayer, the charge density in the QDs can be obtained from the measured surface potential relative to the gate voltage (Fig. 5.6). This spectroscopy method (SPS) has previously been used to analyze the IGS in organic thin films (25–27). Since the lateral resolution of our KPFM setup is 20–50 nm, the measured DOS is an average over tens of QDs and thus represents the ensemble properties of the QD solid, in contrast with STS that measures individual QDs. We can see that the DOS obtained by SPS accurately resolves the band edge of the $1S_h$ states and IGS of PbS-EDT (Fig. 5.5B). The IGS is ~ 0.2 eV higher than the $1S_h$ states, in agreement with the STS results. We are unable to probe the DOS beyond the band edge due to the limited charge injection capability of the FET setup.

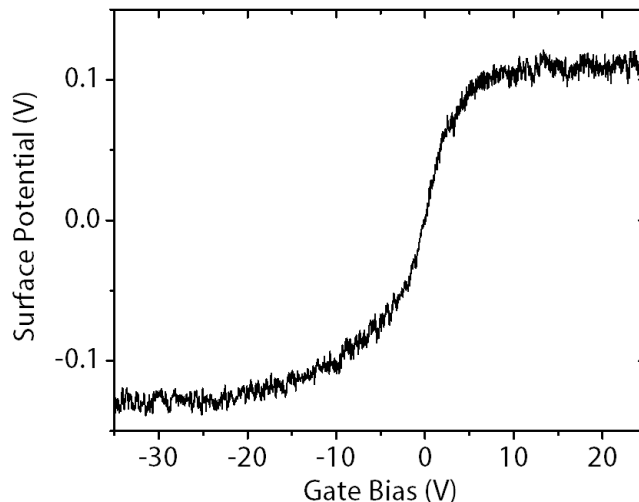


Figure 5.6. SPS of PbS-MPA QDs. Surface potential – gate bias spectrum of PbS-MPA, from which the DOS was extracted and plotted in Fig. 5.5C.

It has been reported that MPA passivates the QD surface more completely than EDT (7, 8, 10). Our SPS results on PbS-MPA (Fig. 5.5C), however, reveals the presence of IGS at nearly the same level as those in the PbS-EDT, indicating that the IGS are not due to incomplete ligand passivation. We further performed SPS on PbS-HYD (Fig. 5.5D), where the hydrazine acts as a reducing agent that was previously assumed to be able to repair surface defects of lead chalcogenide QDs (28, 29). We found that PbS-HYD has a clean band gap with no observable IGS. This result suggests that the previously observed IGS may be related with adsorbed species from the environment that are removed after hydrazine treatment. To test this assumption, we exposed the PbS-HYD QDs to air for 30 seconds and found that IGS reappeared at ~ 0.1 eV above the $1S_h$ states (Fig. 5.5E). We thus suspect that either oxygen or water is at the origin of the observed IGS. As we show next by theoretical analysis and chemical spectroscopy, O_2 is the responsible species. Note that the energy level of $1S_h$ states of all the samples (Fig. 5.5, B to E) are measured to be around 5.1 eV (calibrated with the nearby Au electrode in the FET), in agreement with previously measured results for 5.5 nm PbS QDs (30), further confirming the assignment of all the band edge states.

5.4 Theoretical calculations on in-gap states

In our DFT calculations we used PbS QD of 4 nm diameter, for which we obtained a bandgap of 0.94 eV (Fig. 5.7). This value is slightly smaller than the experimentally observed 1.1 eV bandgap for 4 nm PbS QDs (30), due to the well-known bandgap underestimation in DFT theory (31). Nevertheless, the calculated bandgap matches with that of the 5.5 nm PbS QD used in our experiments. We thus expect the calculated DOS to also match with our experimental observations. We subsequently calculated the formation energy and electronic structure of QDs with various possible vacancies and impurities. Since the QDs are synthesized in solution, we need to consider both neutral vacancies and charged ionic vacancies (with organic counter ions in the nearby solution environment). We found that neutral atomic vacancies (Pb, S, L, where L refers to ligand), neutral divacancies (PbS, PbL_2) and charged ion vacancies (Pb^{2+} , S^{2-} , L) have formation energies in the range of 1.6–2.3 eV, 0.8–1.8 eV and -0.8–1 eV, respectively. Thus the formation of neutral atomic vacancies during QD growth in solution is very unlikely, while

charged ion vacancies are most likely to form. Our calculations show that PbS and S^{2-} vacancies produce IGS near the conduction band, while all other charged ion vacancies and neutral divacancies do not induce IGS (Fig. 5.8). This leads us to conclude that external molecules adsorbed on the QD surface are at the origin of the observed IGS. These molecules need to be small and reactive in order to adsorb on the QD surface after diffusing through the ligands. Prime candidates are water and oxygen because they are present (in trace amounts) during synthesis and during glovebox storage.

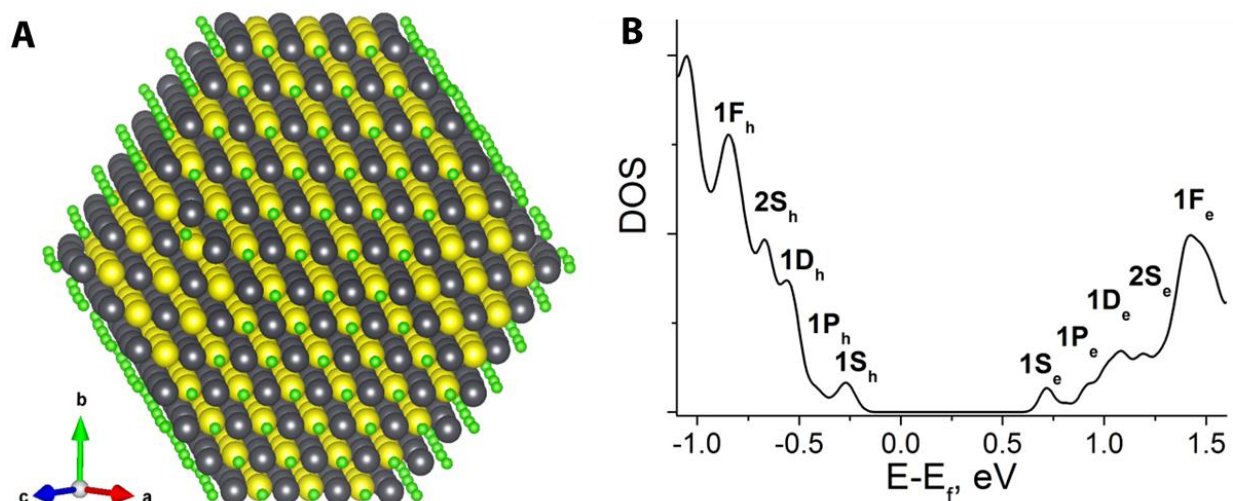


Figure 5.7. Computational model of ideal QDs. (A) Structure of the constructed Cl-passivated PbS QD after relaxation (diameter: 4 nm, Wulff ratio: 0.87). (B) Calculated total density of states of the QD, with a band gap of 0.94 eV.

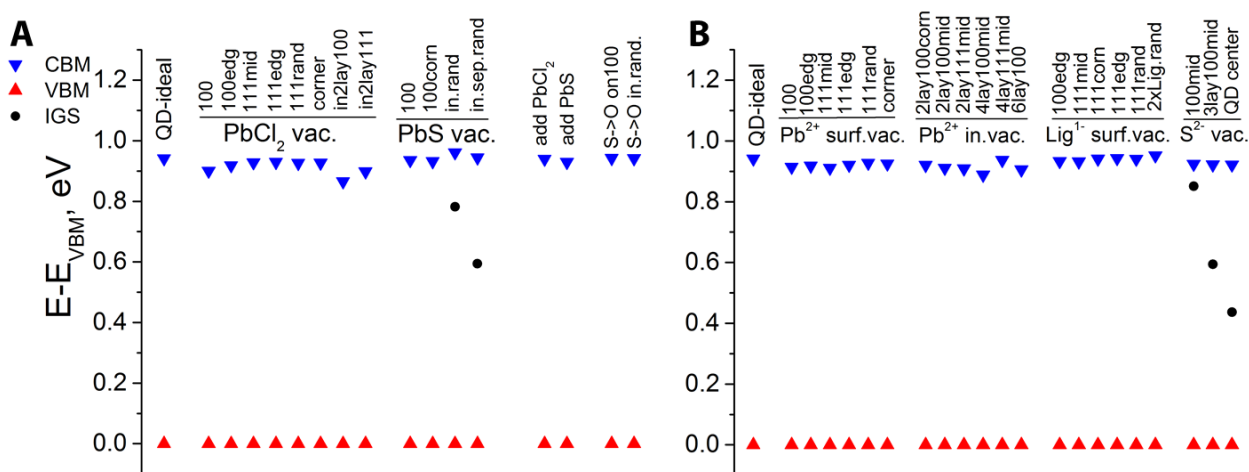


Figure 5.8. In-gap electronic structure of QDs with different defects. (A) single-vacancy ionic defects. (B) Charge balanced vacancy defects, adsorption of additional species PbCl₂ and PbS, and oxygen-substitution defects. Notation: **vac.**-vacancy, **surf.**-surface, **in.**- QD interior, **lig.**-ligand, **100-** on {100} facet, **111-** on {111} facet, **edg-** on a facet edge, **mid-** in a middle of a facet, **rand-** chosen randomly, **2lay100corn-** second layer under {100} facet close to a corner,

4lay111mid - fourth layer under a middle of {111} facet (others accordingly), **QD center**- in the center of QD, **S->O** - substitution of S^{2-} with O^{2-} , **sep.**- separated/not nearest neighbors, **add**- add a molecule on the surface. All of them either produce no IGS, or produce IGS in the upper half of the band gap.

The calculations show that adsorbed water does not produce IGS (Fig. 5.9), while adsorbed molecular oxygen produces IGS slightly above the valence band. Using the spin-polarized generalized gradient approximation (GGA), we found two unoccupied states at 0.07 eV and 0.18 eV above the $1S_h$ state (Fig. 5.10). Higher level hybrid functional imposes a 0.13 eV correction on these states, shifting them up to 0.20 eV and 0.31 eV above $1S_h$ (Fig. 5.11). The energies of these states match those of the experimentally observed IGS in PbS-EDT, PbS-MPA, and the 30 s air exposed PbS-HYD. The two empty O_2 -derived IGS are formed by coupling of the two unoccupied π^* orbitals of molecular oxygen with the $1S_h$ state of the QD. The wave function density of the two IGS extend deep into the QD (Fig. 5.10A). At the center, the wave function density still has a finite value that is 1.07% of the maximum density inside the QD. Accordingly to the Bader charge analysis of the total charge density, a partial electron transfer of $0.33 e^-$ occurs from the QD to the oxygen molecule. The O-O distance in the adsorbed O_2 is 1.278 Å, a slight increase compared to the case of a free molecule (1.241 Å). These results indicate that the oxygen molecule is chemisorbed on the surface of the PbS QD. The calculated formation energy of the oxygen on the QD surface is -0.32 eV (Table 5.1), in contrast with the positive formation energies of various vacancy defects. Since the van der Waals interaction was not taken into account in the calculation, the actual formation energy can be lower (larger in absolute value) than -0.32 eV.

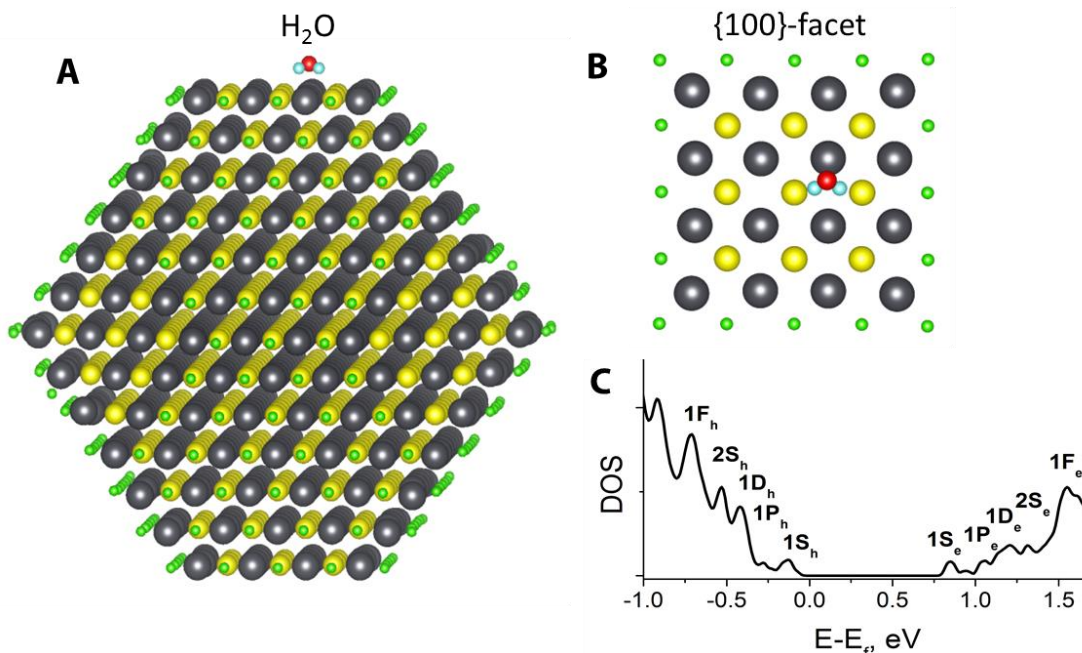


Figure 5.9. Electronic structure of QD with an adsorbed H₂O molecule. (A) Relaxed atomic structure. (B) Top view on {100} facet with the adsorbed H₂O. (C) Calculated DOS for the QD with adsorbed H₂O has a clean band gap of 0.94 eV.

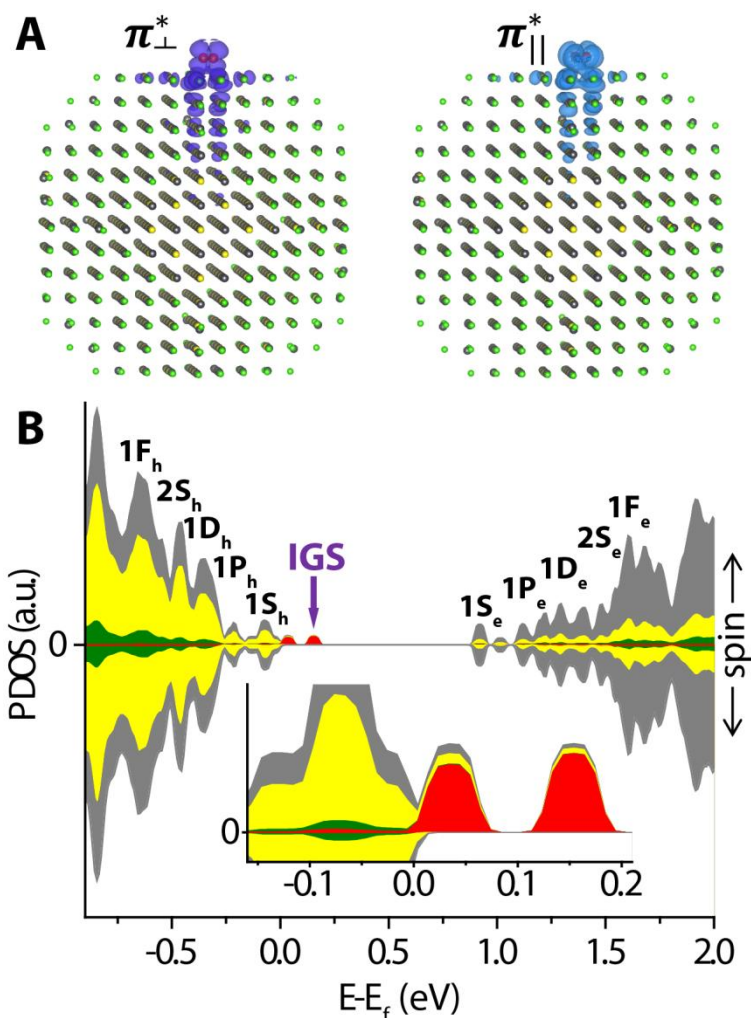


Figure 5.10. DFT calculation reveals molecular oxygen as the origin of IGS. (A) DFT calculated probability density distribution from the wave function of the two unoccupied IGS derived from O₂ adsorbed on a 4 nm PbS QD surface. These states are formed by hybridization of oxygen π_{\perp}^* and π_{\parallel}^* orbitals with the 1S_h state of the QD. (B) DFT calculated spin-polarized partial density of states (PDOS) for PbS QD with one adsorbed O₂ molecule in the GGA approximation. The contributions from different elements are shown in color (Pb: grey, S: yellow, Cl: green, O: red). E_f refers to the Fermi level. There are two empty IGS at 0.07 eV (π_{\perp}^*) and 0.18 eV (π_{\parallel}^*) above the 1S_h state due to triplet states of O₂. Inset: expanded view of the IGS and 1S_h states.

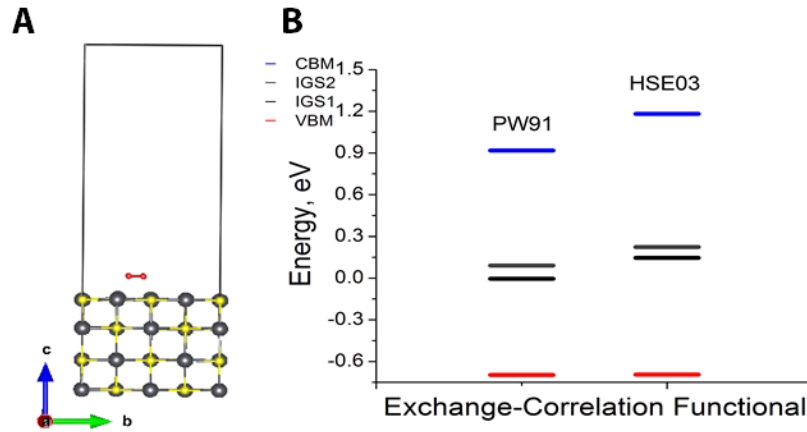


Figure 5.11. Comparison of energy levels of adsorbed O_2 molecule on a PbS (100) slab calculated using the GGA functional (PW91) and from the more accurate hybrid functional (HSE03). (A) Atomic structure of the calculated geometry. (B) Comparison of the calculated energy levels using PW91 and HSE03 functionals (IGS levels from HSE03 are shifted up by ~ 0.13 eV relative to that from PW91).

Table 5.1. Formation energy and presence of IGS of possible adsorbed molecules on a PbS QD

Adsorbate	Formation energy (eV)	Presence of IGS
O_2	-0.32	Yes
$2 O_2$	-0.22	Yes
$2 O$ (dissociated)	-2.36	No
$S \rightarrow O$ (surf)*	-1.08	No
H_2O	-0.78	No

*Substitutional atomic defect where an oxygen atom replaces a sulfur atom on the QD surface.

We calculated also the DOS when oxygen molecules are dissociated on the QD surface (in minimum energy configuration), and found that no IGS are created in that case (Fig. 5.12). Furthermore, substitutional atomic oxygen defects (where an oxygen atom replaces a sulfur atom, both at the surface and interior) were found to not produce IGS either. Therefore, among the theoretically calculated intrinsic and external defects, only molecular oxygen produces IGS with energy levels matching that of the experimental results.

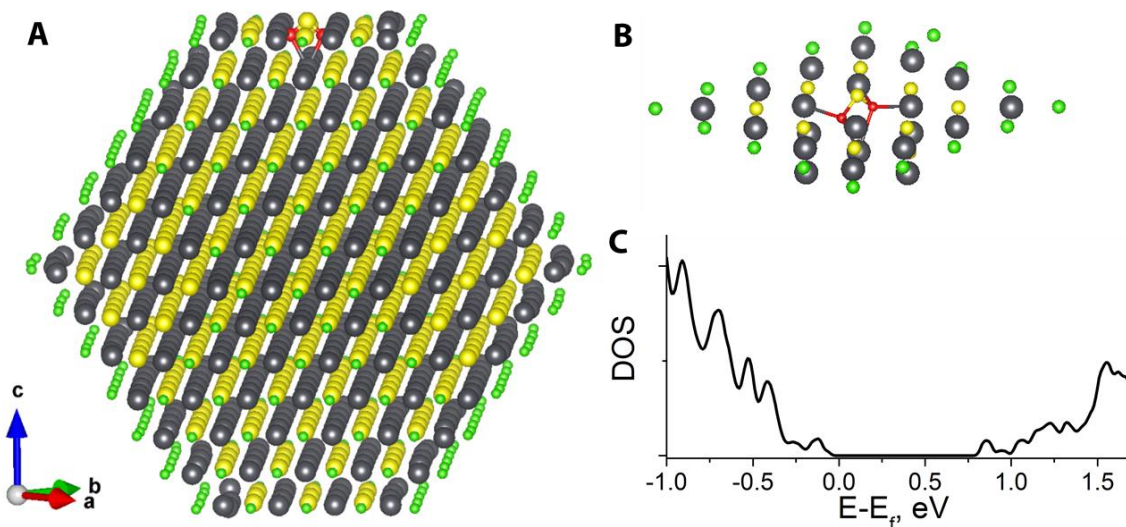


Figure 5.12. Electronic structure of QD with a dissociated oxygen molecule. (A) Relaxed atomic structure. (B) Expanded view of the {100} facet. (C) Calculated DOS for the QD with a dissociated oxygen molecule.

5.5 Spectroscopic evidence and further theoretical support on the origin of IGS

To confirm the existence and analyze the concentration of molecular oxygen, we performed X-ray photoelectron spectroscopy, targeting the O 1s emission peak (Fig. 5.13). All the samples shown in Fig. 5.5 were measured except PbS-MPA where the ligand contains oxygen (thus complicating the spectra). XPS confirms the existence of O₂ (533.9 eV) on PbS-EDT (32). Another peak at 532.1 eV corresponds to the -COO- groups, likely rising from the residual unexchanged oleate ligands (14). In PbS-HYD QDs, in contrast, O₂ species are absent. When exposed to 1 atm of 25% O₂ / 75% Ar gas mixture for 30 s, the 533.9 eV O₂ peak appeared on the PbS-HYD. The 531.3 eV peak corresponds to -OH groups that were present on the oleate passivated QDs (14) and were not fully removed after HYD treatment. Peak area analysis shows that the concentration of O₂ on PbS-EDT and on the 30 s exposed PbS-HYD is roughly similar, approximately 10 molecules per QD on average. The amount of O₂ on PbS-HYD remained constant after 10 min exposure (although the amount of atomic oxygen species increased) (Fig. 5.14). The correlation of the existence/absence of O₂ with that of the IGS, together with the theoretical results on the effect of O₂ in producing the IGS, lends strong support to our conclusion on the origin of the IGS. It should be noted that the XPS spectral resolution is limited by the small amount of oxygen species present on the QDs, and the resolution on the PbS-EDT sample is slightly worse than on the PbS-HYD due to the presence of ligands in the former. Also note that the existence of ~10 O₂ per QD is not contradictory to the STS results where IGS was observed on only ~half of the QDs, since the O₂ not located right under the STM tip may not be sensed by STS, as explained before.

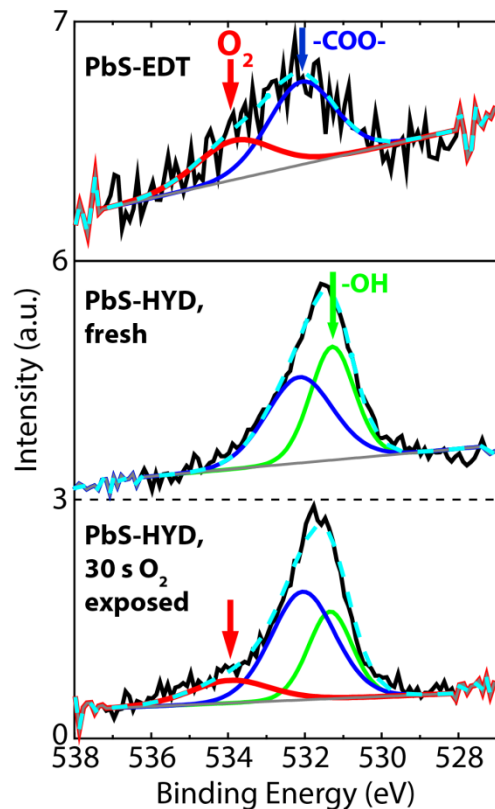


Figure 5.13. X-ray photoelectron spectroscopy shows the existence/absence of O_2 on QDs with/without IGS. O 1s XPS peaks from PbS-EDT (intensity is 3 times expanded), PbS-HYD, and PbS-HYD exposed for 30 s to 1 atm 25% O_2 / 75% Ar gas mixture. Three components are used for the fit. Each component has the same peak position and width for the three samples. The red peak component at 533.9 eV corresponds to O_2 , while the component at 532.1 eV (blue) and that at 531.3 eV (green) are assigned to $-COO-$ and $-OH$ species, respectively.

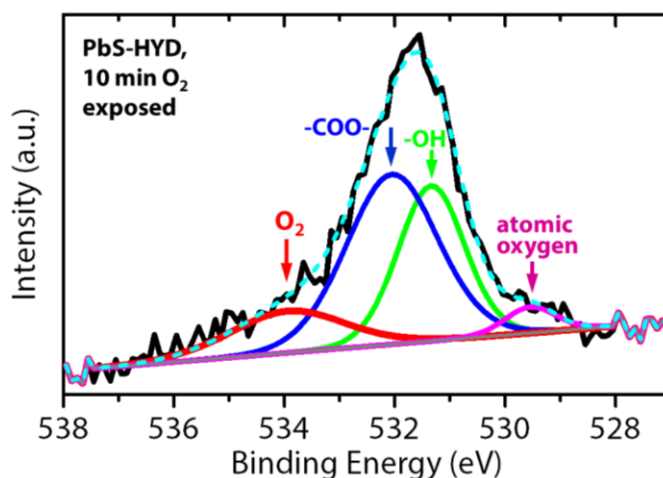


Figure 5.14. O 1s XPS of PbS-HYD after 10 min exposure to O_2/Ar . The atomic oxygen peak at 529.5 eV has a FWHM of 1.1 eV.

Since more than one O_2 molecule can be present on each QD, we further performed calculations on the effect of two O_2 molecules absorbed on two opposite $\{100\}$ facets. The wave functions of the IGS induced by the two molecules are symmetric and have a very small coupling between them (Fig. 5.15A). The IGS wave function density at the center of the QD is 1.24% of the maximum density inside the QD, slightly larger than the case of single O_2 . Using GGA approximation we obtained the DOS shown in Fig. 5.15B. Four states appear inside the band gap, with two spin-up states (0.05 eV and 0.16 eV above the $1S_h$ state) and two spin-down states (0.06 eV and 0.18 eV above the $1S_h$ state). We can see that in the case of two O_2 , the IGS induced by each O_2 resembles that of the IGS of single O_2 on the QD. Similar with the single O_2 case, using the higher level hybrid functional we expect the same 0.13 eV upshift in energy in the two O_2 case, resulting in four states between 0.18–0.31 eV above the $1S_h$ state. We thus expect that the energy level of the IGS in the case of multiple O_2 on one QD will not change significantly as long as these states are not strongly coupled.

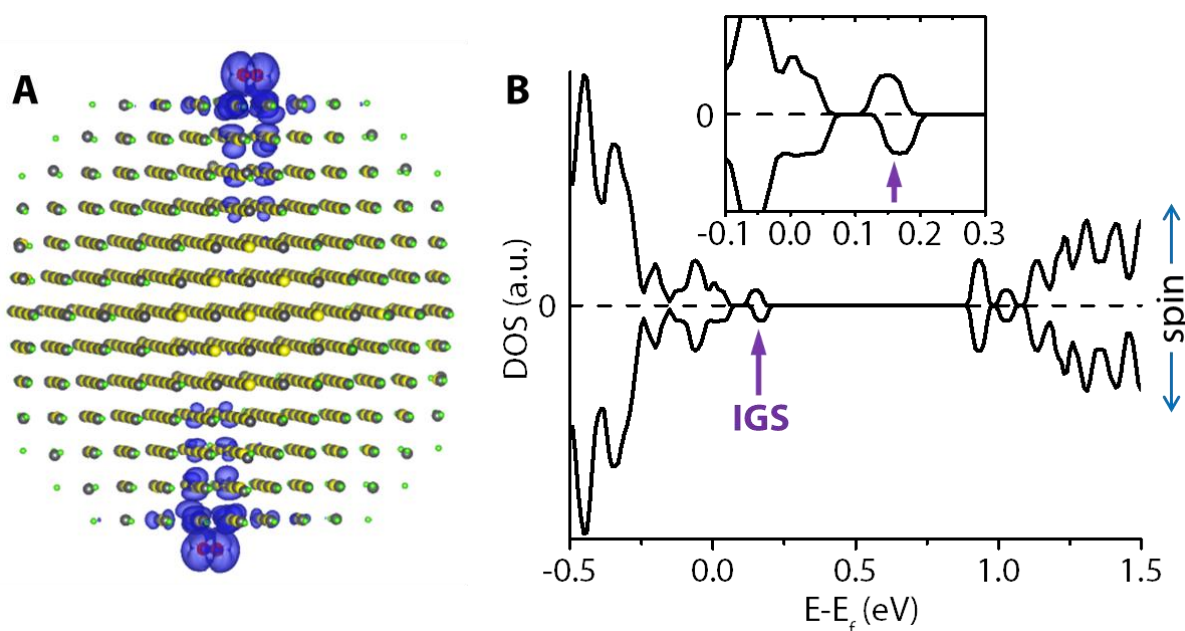


Fig. 5.15. DFT calculations of two O_2 molecules on a PbS quantum dot. (A) Integrated probability density distribution of the states between E_f and $E_f + 0.25$ eV. (B) Calculated spin-polarized DOS in the GGA approximation. The inset is an expanded view of the IGS. Four IGS are present at 0.05 eV (π_{\perp}^*) and 0.16 eV (π_{\parallel}^*) above the $1S_h$ state (spin-up), and 0.06 eV (π_{\perp}^*) and 0.18 eV (π_{\parallel}^*) above the $1S_h$ state (spin-down).

With two O_2 on the QD, charge transfer from QD to each of the O_2 molecule estimated from Bader charge analysis decreases to $0.30 e^-$ per molecule. This is because the QD is resistant to more electron withdrawal. As a result the formation energy increases to -0.22 eV per molecule. With more O_2 on the QD, we expect a further increase of formation energy. This might be the reason why the amount of O_2 saturates after the PbS-HYD was exposed to oxygen for only 30 s (as shown by XPS). The formation energy of various possible impurity defects are shown in Table 5.1. Molecular oxygen has the largest formation energy (smallest in absolute value) among the considered impurities, and is the only one that produces IGS. We need to note that prolonged oxidation of PbS QDs results in the formation of various oxide species such as $PbSO_3$ and $PbSO_4$.

(33). In that case the simple vacancy and impurity defect picture is not sufficient to describe the electronic structure of the QD, since the composition is significantly modified.

5.6 Discussion and Conclusion

We have considered various possible defects that can form during the solution phase synthesis process, which is the first step of all the device fabrication based on colloidal QDs. Among these defects, molecular oxygen, an unintentional impurity that is hard to avoid, is found to be the source of IGS near the valence band. Various post-synthetic treatments, on the other hand, can modify the amount and/or type of defects, thus changing the IGS. The hydrazine treatment shown here is one example of removing O₂ and eliminating IGS. Another post-synthesis approach of electronic modification is stoichiometry control via deposition of excess lead or chalcogen (34, 35). Although neutral atomic vacancies are unlikely to form during solution synthesis (as discussed before), this post-synthesis control can produce QDs with excess Pb or S (*i.e.*, QD with neutral S or Pb vacancies). According to previous calculations (8, 9) and our own DFT results (not shown here), neutral Pb vacancies produce IGS near the valence band, while neutral S or L (ligand) vacancies produce IGS near the conduction band.

The intrinsic defect physics of lead chalcogenide QDs can be understood in the general scheme of ionic semiconductors. Similar to methylammonium lead iodide perovskite systems (36), charge balanced (surface fully passivated by ligands) PbS QDs do not show IGS. This has been demonstrated by DFT calculations on PbS QDs passivated with oleic acid and hydroxyl groups (14), with EDT (9), and with MPA + Cl (8). All the above ligands form ionic bonds with the surface Pb²⁺, thus maintaining the overall stoichiometry of the Pb-rich QD (37–39). In our work, to make DFT calculations possible on a QD as large as 4 nm, we used Cl as the passivation ligand and found a clean band gap after complete passivation. As long as the ligands form ionic bonds with Pb, different ligand species are expected to have similar effects on IGS properties. This is in agreement with our experimental results where similar IGS were found on QDs with three different chemical treatments (EDT, MPA, and HYD+O₂).

As explained before, as-synthesized QDs in solution tend to have no neutral defects due to their large formation energy. To fabricate electronically active devices, however, the QD solids typically need to go through ligand exchange process (7, 8) which can result in a loss of ligands leading to QDs with excess cation atoms (Pb in our case). These neutral vacancy defects, if present, will induce IGS near the conduction band. However, the fact that we observed no n-type IGS indicates that either our QDs are well passivated by ligands (*i.e.* there is no ligand vacancy) or the IGS induced by ligand vacancies are too close (within ~50 meV) to the conduction band to be observed. In either case, O₂ remains the only experimentally observable deep IGS in typical ligand exchanged QD solids that can be detrimental to optoelectronic devices.

It has previously been found that oxygen exposure can induce p-type doping in lead chalcogenide QDs (40–42), supporting the O₂-induced IGS mechanism. Moreover, these QD solids with various ligand treatments (*e.g.* EDT, n-butylamine, MPA, *etc.*) exhibit unintentional p-type doping even in inert atmosphere, with a carrier density of 10¹⁶ – 10¹⁷ cm⁻³ for QDs between 5–6 nm (34, 43, 44). This doping effect is also mainly due to the IGS produced by O₂, whose surface concentration on the QD is limited by the energy cost of the charge transfer from

the QD to the adsorbed O₂ (as explained above). From our STS results on the PbS-EDT we obtain an average Fermi level (E_f) – 1S_h state (E_v) separation of 0.15 eV (averaged over the QDs with observable IGS, since those without IGS tend to have 1S_h states far from the Fermi level and are thus electronically inactive). The estimated effective density of valence band states for our 5.5 nm PbS QD solids is $n_v = 2.1 \times 10^{19} \text{ cm}^{-3}$ (see Methods). Thus at room temperature the hole carrier density can be calculated as (Sze 1981): $p = n_v \exp\left(-\frac{E_f - E_v}{kT}\right) = 6.4 \times 10^{16} \text{ cm}^{-3}$, in good agreement with previously measured results. This quantitative agreement reveals that our proposed IGS mechanism is generally applicable to lead chalcogenide QDs, where unintentional doping can be induced by surface-saturated O₂.

In conclusion, we have identified molecular oxygen as the dominant source of IGS for the colloidal PbS quantum dots. The in-gap electronic structure of the QDs is immune to most of the charged ion vacancies that may form during the synthesis process. To engineer IGS-free QDs for optoelectronic applications, we need to first reduce the surface oxygen during the post-synthesis treatment process, and ideally also fully passivate the surface with ligands that can block the re-adsorption of O₂ on QDs (12, 13).

5.7 Methods Summary

Synthesis of PbS quantum dots (QDs) was done following a previously reported procedure (45). QD size and morphology were measured by transmission electron microscopy, while their band gap is determined by UV-Vis absorption spectroscopy. QD monolayers were prepared by spin-coating colloidal QDs on a substrate followed by chemical treatments and solvent washing to obtain a monolayer with different ligands or different surface chemistry. The species of the surface ligands were characterized by Fourier transform infrared spectroscopy measurements. All of the sample preparation procedures were done in Ar glovebox with <1 ppm oxygen. Sample transfer to the measurement chambers of KPFM, STM, and XPS were done using a nitrogen glove bag or portable vacuum chamber. During the whole sample preparation, transfer, and measurement process the sample was never exposed to air.

STM measurements were performed with a home-built system operated at 77 K in ultra high vacuum. The differential conductance (dI/dV) spectra were measured using lock-in technique with fixed tip to sample distance. The electronic structure of the tip was checked by recording background spectra on the bare ITO substrate, before and after measuring the STS spectra of each QD.

DFT calculations were carried out using the Vienna Ab initio Simulation Package (VASP), using the generalized gradient approximation (GGA) functional (PW91) and a hybrid functional (HSE03).

XPS was done on thin film samples deposited on Au. The O 1s peak energy was calibrated by the Pb 4f peak. Gaussian-Lorentzian peak fitting was performed by fixing the peak energy and width of each component to be the same, for all the four samples (PbS-EDT, PbS-HYD, 30 s exposed PbS-HYD, 10 min exposed PbS-HYD). Concentration of the O₂ species was estimated by comparing the O 1s and the Pb 4f peak areas, and considering the atomic sensitivity factor and geometric factors.

The effective density of hole states is estimated using: $n_v = 8/V_{eff}$, considering that the valence band of PbS QDs is 8-fold degenerate (46). V_{eff} is the effective average volume occupied by each QD. Assuming that the QDs have spherical shape, with volume fill fraction of 0.5, and an inter-QD distance of 1.6 nm for PbS-EDT (43), we have $V_{eff} = 3.75 \times 10^{-19} \text{cm}^3$. Thus $n_v = 2.1 \times 10^{19} \text{cm}^{-3}$.

References

1. S. M. Sze, *Physics of Semiconductor Devices* (2nd Edition; Wiley, New York, ed. 2, 1981).
2. H. J. Queisser, E. E. Haller, Defects in semiconductors: some fatal, some vital. *Science* **281**, 945–950 (1998).
3. R. Ruruli, Colloquium: Structural, electronic, and transport properties of silicon nanowires. *Rev. Mod. Phys.* **82**, 427–449 (2010).
4. P. Nagpal, V. I. Klimov, Role of mid-gap states in charge transport and photoconductivity in semiconductor nanocrystal films. *Nat. Commun.* **2**, 486 (2011).
5. M. V. Wolkin, J. Jorne, P.M. Fauchet, G. Allan, C. Delerue, Electronic states and luminescence in porous silicon quantum dots: the role of oxygen. *Phys. Rev. Lett.* **82**, 197 (1999).
6. A. A. Cordones, M. Scheele, A. P. Alivisatos, S. R. Leone, Probing the interaction of single nanocrystals with inorganic capping ligands: time-resolved fluorescence from CdSe-CdS quantum dots capped with chalcogenidometalates. *J. Am. Chem. Soc.* **134**, 18366–18373 (2012).
7. J. Tang, K. W. Kemp, S. Hoogland, K. S. Jeong, H. Liu, L. Levina, M. Furukawa, X. Wang, R. Debnath, D. Cha, K. W. Chou, A. Fischer, A. Amassian, J. B. Asbury, E. H. Sargent, Colloidal-quantum-dot photovoltaics using atomic-ligand passivation. *Nat. Mater.* **10**, 765–771 (2011).
8. A. H. Ip, S. M. Thon, S. Hoogland, O. Voznyy, D. Zhitomirsky, R. Debnath, L. Levina, L. R. Rollny, G. H. Carey, A. Fischer, K. W. Kemp, I. J. Kramer, Z. Ning, A. J. Labelle, K. W. Chou, A. Amassian, E. H. Sargent, Hybrid passivated colloidal quantum dot solids. *Nat. Nanotechnol.* **7**, 577–582 (2012).
9. D. Kim, D.-H. Kim, J.-H. Lee, J. C. Grossman, Impact of stoichiometry on the electronic structure of PbS quantum dots. *Phys. Rev. Lett.* **110**, 196802 (2013).
10. K. S. Jeong, J. Tang, H. Liu, J. Kim, A. W. Schaefer, K. Kemp, L. Levina, X. Wang, S. Hoogland, R. Debnath, L. Brzozowski, E. H. Sargent, J. B. Asbury, Enhanced mobility-lifetime products in PbS colloidal quantum dot photovoltaics. *ACS Nano* **6**, 89–99 (2012).
11. O. Voznyy, S. M. Thon, A. H. Ip, E. H. Sargent, Dynamic trap formation and elimination in colloidal quantum dots. *J. Phys. Chem. Lett.* **4**, 987–992 (2013).
12. Z. Ning, O. Voznyy, J. Pan, S. Hoogland, V. Adinolfi, J. Xu, M. Li, A. R. Kirmani, J.-P. Sun, J. Minor, K. W. Kemp, H. Dong, L. Rollny, A. Labelle, G. Carey, B. Sutherland, I. Hill, A. Amassian, H. Liu, J. Tang, O. M. Bakr, E. H. Sargent, Air-stable n-type colloidal quantum dot solids. *Nat. Mater.* **13**, 822–828 (2014).

13. C. M. Chuang, P. R. Brown, V. Bulović, M. G. Bawendi, Improved performance and stability in quantum dot solar cells through band alignment engineering. *Nat. Mater.* **13**, 786–801 (2014).
14. D. Zherebetsky, M. Scheele, Y. Zhang, N. Bronstein, C. Thompson, D. Britt, M. Salmeron, P. Alivisatos, L.-W. Wang, Hydroxylation of the surface of PbS nanocrystals passivated with oleic acid. *Science* **344**, 1380–1384 (2014).
15. D. Bozyigit, M. Jakob, O. Yarema, V. Wood, Deep level transient spectroscopy (DLTS) on colloidal-synthesized nanocrystal solids. *ACS Appl. Mater. Interfaces* **5**, 2915–2919 (2013).
16. D. Bozyigit, S. Volk, O. Yarema, V. Wood, Quantification of deep traps in nanocrystal solids, their electronic properties, and their influence on device behavior. *Nano Lett.* **13**, 5284–5288 (2013).
17. A. Pandey, P. Guyot-Sionnest, Slow electron cooling in colloidal quantum dots. *Science* **322**, 929–932 (2008).
18. K. Katsiev, A. H. Ip, A. Fischer, I. Tanabe, X. Zhang, A. R. Kirmani, O. Voznyy, L. R. Rollny, K. W. Chou, S. M. Thon, G. H. Carey, X. Cui, A. Amassian, P. Dowben, E. H. Sargent, O. M. Bakr, The Complete In-Gap Electronic Structure of Colloidal Quantum Dot Solids and Its Correlation with Electronic Transport and Photovoltaic Performance. *Adv. Mater.* **26**, 937–942 (2014).
19. P. R. Brown, D. Kim, R. R. Lunt, N. Zhao, M. G. Bawendi, J. C. Grossman, V. Bulović, Energy level modification in lead sulfide quantum dot thin films through ligand exchange. *ACS Nano* **8**, 5863–5872 (2014).
20. B. Diaconescu, L. A. Padilha, P. Nagpal, B. S. Swartzentruber, V. I. Klimov, Measurement of electronic states of PbS nanocrystal quantum dots using scanning tunneling spectroscopy: the role of parity selection rules in optical absorption. *Phys. Rev. Lett.* **110**, 127406 (2013).
21. P. Liljeroth, K. Overgaag, A. Urbieto, B. Grandier, S. G. Hickey, D. Vanmaekelbergh, *Phys. Rev. Lett.* **95**, 086801 (2005).
22. K. Overgaag, P. Liljeroth, B. Grandier, D. Vanmaekelbergh, Scanning tunneling spectroscopy of individual PbSe quantum dots and molecular aggregates stabilized in an inert nanocrystal matrix. *ACS Nano* **2**, 600–606 (2008).
23. J. M. Luther, M. Law, M. C. Beard, Q. Song, M. O. Reese, R. J. Ellingson, A. J. Nozik, Schottky solar cells based on colloidal nanocrystal films. *Nano Lett.* **8**, 3488–3492 (2008).
24. A. R. Barkhouse, A. G. Pattantyus-Abraham, L. Levina, E. H. Sargent, Thiols passivate recombination centers in colloidal quantum dots leading to enhanced photovoltaic device efficiency. *ACS Nano* **2**, 2356–2362 (2008).
25. Y. Zhang, D. Ziegler, M. Salmeron, Charge trapping states at the SiO₂-oligothiophene monolayer interface in field effect transistors studied by Kelvin probe force microscopy. *ACS Nano* **7**, 8258–8265 (2013).
26. K. Celebi, P. J. Jadhav, K. M. Milaninia, M. Bora, M. A. Baldo, The density of states in thin film copper phthalocyanine measured by Kelvin probe force microscopy. *Appl. Phys. Lett.* **93**, 083308 (2008).
27. O. Tal, Y. Rosenwaks, Y. Preezant, N. Tessler, C. K. Chan, A. Kahn, Direct determination of the hole density of states in undoped and doped amorphous organic films with high lateral resolution. *Phys. Rev. Lett.* **95**, 256405 (2005).

28. D. V. Talapin, C. B. Murray, PbSe nanocrystal solids for n- and p-channel thin film field-effect transistors. *Science* **310**, 86–89 (2005).
29. W. Koh, A. Y. Kuposov, J. T. Stewart, B. N. Pal, I. Robel, J. M. Pietryga, V. I. Klimov, Heavily doped n-type PbSe and PbS nanocrystals using ground-state charge transfer from cobaltocene. *Sci. Rep.* **3**, 2004 (2013).
30. J. Jasieniak, M. Califano, S. E. Watkins, Size-dependent valence and conduction band-edge energies of semiconductor nanocrystals. *ACS Nano* **5**, 5888–5902 (2011).
31. J. P. Perdew, Density functional theory and the band gap problem. *Int. J. Quantum Chem.* **19**, 497–523 (1986).
32. Z. Shuxian, W. K. Hall, G. Ertl, H. Knözinger, X-ray photoemission study of oxygen and nitric oxide adsorption on MoS₂. *J. Catal.* **100**, 167–175 (1986).
33. J. Tang, L. Brzozowski, D. A. R. Barkhouse, X. Wang, R. Debnath, R. Wolowiec, E. Palmiano, L. Levina, A. G. Pattantyus-Abraham, D. Jamakosmanovic, E. H. Sargent, Quantum dot photovoltaics in the extreme quantum confinement regime: the surface-chemical origins of exceptional air- and light-stability. *ACS Nano* **4**, 869–878 (2010).
34. S. J. Oh, N. E. Berry, J.-H. Choi, E. A. Gauding, T. Paik, S.-H. Hong, C. B. Murray, C. R. Kagan, Stoichiometric control of lead chalcogenide nanocrystal solids to enhance their electronic and optoelectronic device performance. *ACS Nano* **7**, 2413–2421 (2013).
35. S. J. Oh, N. E. Berry, J.-H. Choi, E. A. Gauding, H. Lin, T. Paik, B. T. Diroll, S. Muramoto, C. B. Murray, C. R. Kagan, Designing high-performance PbS and PbSe nanocrystal electronic devices through stepwise, post-synthesis, colloidal atomic layer deposition. *Nano Lett.* **14**, 1559–1566 (2014).
36. J. Kim, S.-H. Lee, J. H. Lee, K.-H. Hong, The role of intrinsic defects in methylammonium lead iodide perovskite. *J. Phys. Chem. Lett.* **5**, 1312–1317 (2014).
37. J. Owen, The coordination chemistry of nanocrystal surfaces. *Science* **347**, 615–616 (2015).
38. I. Moreels, K. Lambert, D. De Muynck, F. Vanhaecke, D. Poelman, J. C. Martins, G. Allan, Z. Hens, Composition and size-dependent extinction coefficient of colloidal PbSe quantum dots. *Chem. Mater.* **19**, 6101–6106 (2007).
39. H. Choi, J.-H. Ko, Y.-H. Kim, S. Jeong, Steric-hindrance-driven shape transition in PbS quantum dots: Understanding size-dependent stability. *J. Am. Chem. Soc.* **135**, 5278–5281 (2013).
40. K. S. Leschkies, M. S. Kang, E. S. Aydil, D. J. Norris, Influence of atmospheric gases on the electrical properties of PbSe quantum-dot films. *J. Phys. Chem. C* **114**, 9988–9996 (2010).
41. N. Zhao, T. P. Osedach, L.-Y. Chang, S. M. Geyer, D. Wanger, M. T. Binda, A. C. Arango, M. G. Bawendi, V. Bulovic, *ACS Nano* **4**, 3743–3752 (2010).
42. M. H. Zarghami, Y. Liu, M. Gibbs, E. Gebremichael, C. Webster, M. Law, p-Type PbSe and PbS quantum dot solids prepared with short-chain acids and diacids. *ACS Nano* **4**, 2475–2485 (2010).
43. E. J. D. Klem, H. Shukla, S. Hinds, D. D. MacNeil, L. Levina, E. H. Sargent, Impact of dithiol treatment and air annealing on the conductivity, mobility, and hole density in PbS colloidal quantum dot solids. *Appl. Phys. Lett.* **92**, 212105 (2008).
44. J. Gao, J. M. Luther, O. E. Semonin, R. J. Ellingson, A. J. Nozik, M. C. Beard, Quantum dot size dependent J-V characteristics in heterojunction ZnO/PbS quantum dot solar cells. *Nano Lett.* **11**, 1002–1008 (2011).

45. M. A. Hines, G. D. Scholes, Colloidal PbS nanocrystals with size-tunable near-infrared emission: Observation of post-synthesis self-narrowing of the particle size distribution. *Adv. Mater.* **15**, 1844–1849 (2003).
46. I. Kang, F. W. Wise, Electronic structure and optical properties of PbS and PbSe quantum dots. *J. Opt. Soc. Am. B* **14**, 1632–1646 (1997).

Chapter 6: Imaging Charge Percolation Pathways in Quantum Dot Solids

Reproduced in part and adapted with permission from Nano Letters 2015, 15 (5), 3249–3253.
Copyright © 2015, American Chemical Society.

6.1 Abstract

Charge hopping and percolation in quantum dot (QD) solids has been widely studied, but the microscopic nature of the percolation process is not understood or determined. Here we present the first imaging of the charge percolation pathways in two-dimensional PbS QD arrays using Kelvin probe force microscopy (KPFM). We show that under dark conditions electrons percolate via in-gap states (IGS) instead of the conduction band, while holes percolate via valence band states. This novel transport behavior is explained by the electronic structure and energy level alignment of the individual QDs, which was measured by scanning tunneling spectroscopy (STS). Chemical treatments with hydrazine can remove the IGS, resulting in an intrinsic defect-free semiconductor, as revealed by STS and surface potential spectroscopy. The control over IGS can guide the design of novel electronic devices with impurity conduction, and photodiodes with controlled doping.

6.2 Introduction

An important goal in the design of modern materials is to create new forms of matter by combining elementary nanoscale building blocks.¹⁻⁹ One example is the artificial solids formed by placing quantum dots in arrays.⁴⁻⁹ By controlling the bandgap of the individual dots through their size, and the degree to which charges move from one dot to the next through controlled barriers, we can design and tune the transport properties of quantum dot solids. Potential applications include solution-processed field effect transistors, solar cells, photodetectors, *etc.*⁴⁻⁹ The individual QDs are themselves complex, tiny solids, comprised of hundreds to thousands of atoms. Inevitably the fabrication of these constituents is imperfect; consequently, the QDs are not identical in the number and arrangement of atoms. In addition, defects and impurities are also present that can play an important role.¹⁰⁻¹³ Therefore, it is not surprising that the microscopic mechanisms of charge hopping in QD arrays has not yet been determined.^{7,8,13-17}

Understanding the transport mechanism is also relevant to a broader class of disordered semiconductors,¹⁸ which are systems with spatial disorder and/or heterogeneity in the electronic states. Examples include amorphous silicon,¹⁹ heavily doped and highly compensated semiconductors,²⁰ and organic semiconductors.²¹ These systems exhibit spatially varying potential energy landscapes, which are determined by the microscopic disorder, the energy level alignment of individual sites, and the strength of coupling between adjacent sites. When charges are injected, they will fill the potential valleys, forming percolation pathways.²² As a model system, quantum dot solids offer a unique opportunity for local characterization of the individual building blocks, whose properties can be correlated with the mesoscale percolation and ensemble transport phenomena.

Here we combined scanning tunneling microscopy (STM), KPFM and field effect transistor (FET) techniques to characterize the states responsible for charge percolation in QD solids both

microscopically and spectroscopically. We found a phenomenon where IGS induce Fermi level pinning favoring electron transport via the conductive IGS, forming percolation pathways. Both the technical methodology and the determined transport mechanism can be generally applicable to other disordered semiconductors.

6.3 Direct Imaging of Charge Transport in PbS Quantum Dots

We chose PbS QDs as the artificial atoms from which to form artificial solids, in the form of thin films consisting of 0–2 QD layers. These QDs show strong quantum confinement due to the large Bohr radius,²³ so that the wave function of one dot can extend into neighboring dots, giving rise to an electrically active QD solid. As-synthesized PbS QDs (5.5 nm diameter, ~0.9 eV bandgap) are capped with insulating oleate ligands²⁴ that can be exchanged with shorter ligands such as 1,2-ethanedithiol (EDT), 3-mercaptopropionic acid (MPA), iodide, *etc.*, to couple the QDs and enhance conduction.^{5,6,12-15}

To resolve the spatial and energetic pathways of electron and hole transport, we used KPFM^{25,26} to quantitatively image the local surface potential (V_{sf}) distribution in a QD film deposited in the channel region of a field effect transistor (FET) (Figure 6.1A). All KPFM and FET measurements were done under dark conditions in an inert atmosphere. The QDs were treated with EDT (labeled PbS-EDT). The oxide surface in the FET channel region was passivated by a layer of octadecyltrichlorosilane (OTS) to remove charge traps at the oxide surface. The sign of V_{sf} is set such that $E = eV_{sf}$, where e is the absolute value of the elementary charge, and E is the Fermi level position relative to vacuum. To image the charge percolation pathways we functionalized the KPFM tip with PbS QDs, resulting in ~10 nm spatial resolution. To distinguish conductive from non-conductive regions we applied a high gate bias ($V_g = \pm 52 V$) to inject ~1 elementary charge per QD into the channel (with source/drain electrodes grounded). The surface potential along the percolation pathways will be pinned by the energy levels responsible for charge transport. The areas with no conductive states at the corresponding energy will exhibit higher (for electrons) or lower (for holes) surface potential due to gate field penetration. The topographic image shows the distribution of individual PbS-EDT QDs in a channel area (Figure 6.1B), while the surface potential images of the same area (Figure 6.1C, D) reveal the transport pathway structures. The electron percolation pathways, shown by the cyan/blue areas in Figure 6.1C (where the injected electrons reside), are in the form of narrow stripes surrounded by electron-insulating areas (red/white). In contrast, the hole percolation pathways, shown by the white/red areas in Figure 6.1D (where the injected holes reside), form larger domains surrounded by hole-insulating areas (blue/cyan). The hole transporting level is located at ~-5.0 eV (below vacuum level), matching the valence band edge position of the QDs.²⁷ However, the level responsible for electron transport is located at ~-4.8 eV, far below the conduction band edge (~-4.1 eV). The presence of electron-conducting IGS at ~-4.8 eV is an unexpected finding.

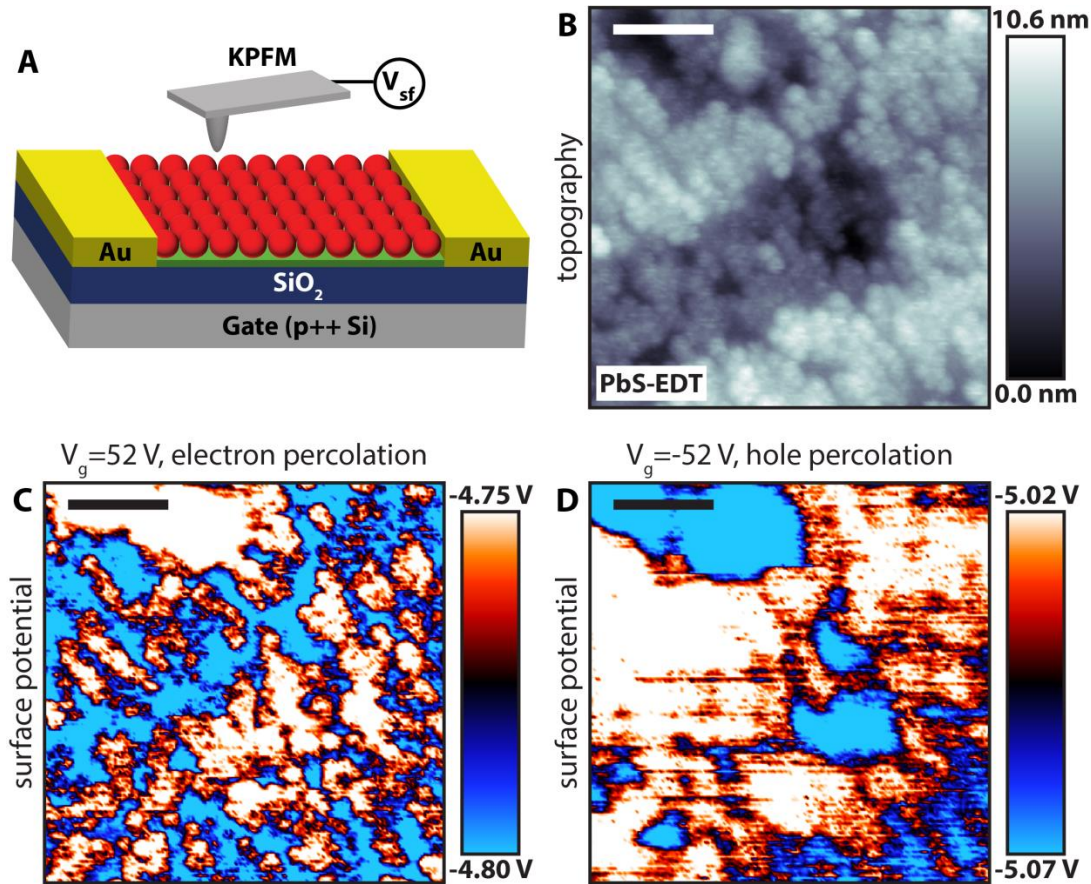


Figure 6.1. Imaging charge percolation pathways in QD solids. (A) Schematic diagram of a QD thin film FET and KPFM probe setup. Au electrodes serve as the source and drain. The FET channel length is 20 μm , and its width is 1 mm. A monolayer of OTS (green) was preadsorbed on the SiO₂ surface of the channel to passivate the oxide surface trap states. (B to D) KPFM images of the same region in the channel area of a PbS-EDT QD array FET. Scale bar: 50 nm. (B) topography showing 0–2 layers of QDs, (C) and (D) surface potential maps at $V_g = 52$ V and $V_g = -52$ V, respectively. Source and drain electrodes were grounded during measurements. The color scales of the surface potential images are saturated to enhance contrast.

Figure 6.1C, D shows surface potential images of PbS-EDT in a color saturated scale. The same images with almost full scales are shown in Figure 6.2. As can be seen, the same charge percolation pathways are present as that in Figure 6.1C, D. The actual peak-to-peak fluctuations of the surface potential in both images are ~ 100 mV. Some areas that are voids with a size of 1–2 QDs shown in the topography image (Figure 6.1B) have a low surface potential in Figure 6.1C, corresponding to electron percolation pathways. This apparent controversy can be understood by taking into account that the resolution of surface potential is ~ 10 nm. In our frequency modulation KPFM, surface potential is sensed via the phase signal which is roughly proportional to $1/d^3$, where d is the tip-sample distance. When the tip is on top of the ~ 10 nm void area of insulating substrate, the surface potential is approximately the same as that of the surrounding QDs, since the gate electrode is far away (300 nm). If the QDs at the boundary of the small void have more IGS (which is actually probable since these areas may be more sensitive to

impurity adsorption due to a smaller amount of neighboring QDs), then it is likely that these areas show low surface potential due to electron percolation in the surrounding QDs.

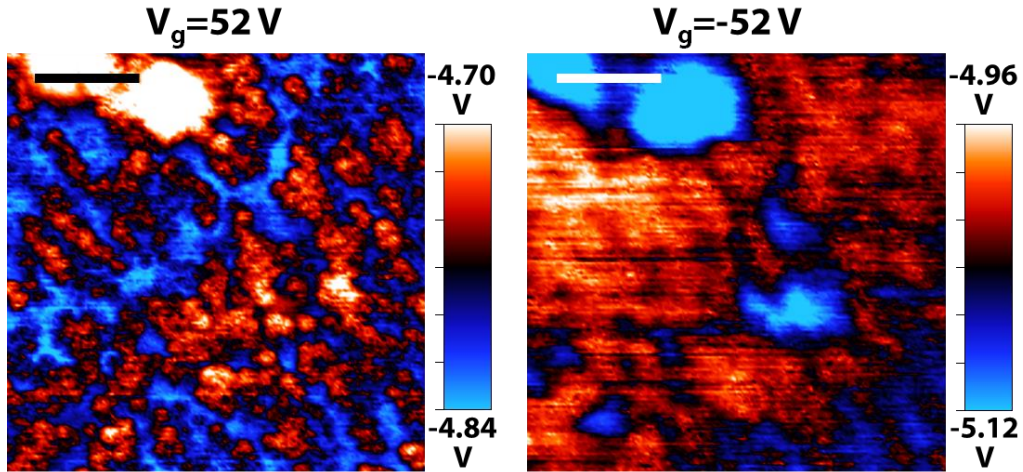


Figure 6.2. Surface potential images of PbS-EDT with $V_g = \pm 52$ V as labeled. These images are the same as those in Figure 1C, D but are displayed on a nearly full color scale and therefore have less contrast. Scale bar: 50 nm.

A back-of-the-envelope calculation quantitatively supports the observed small potential fluctuation, even though a high gate bias (~ 50 V) was applied. The surface potential of an insulating region is the average of the surrounding conductive regions (~ 10 nm away) and the gate (~ 300 nm away). Taking into account that the dielectric constant of SiO_2 is 3.9, the effective oxide thickness is $300 \text{ nm} / 3.9 \approx 80 \text{ nm}$. Thus the potential change induced on the insulating QD by the 50 V gate bias is roughly (assuming zero potential at the nearby conductive QDs): $50 \text{ V} \times (10/80)^3 \approx 100 \text{ mV}$, nearly the same as the observed potential fluctuation.

6.4 In-Gap States and Charge Percolation Mechanism

To better understand the percolation phenomena, we measured the electronic structure of individual QDs using STM and STS (Figure 6.3A, B). Measurements were done at 77 K in ultra high vacuum (base pressure $< 10^{-10}$ mbar). STS was performed to obtain density of states (DOS) spectra on 30 randomly chosen QDs deposited on an indium tin oxide (ITO) substrate. Three different kinds of spectra were observed (Figure 6.3C). About half of the spectra (type 1) show peaks due to IGS at ~ 0.05 – 0.1 eV above the Fermi level, and $1S_h$ states (valence band) at ~ 0.1 – 0.25 eV below the Fermi level. Type 2 and type 3 spectra (similar amount) show no IGS. Type 2 spectra have the $1S_h$ states in the same range as type 1 spectra, whereas type 3 spectra have $1S_h$ states at ~ 0.25 – 0.45 eV below the Fermi level. The origin of the IGS will be discussed later.

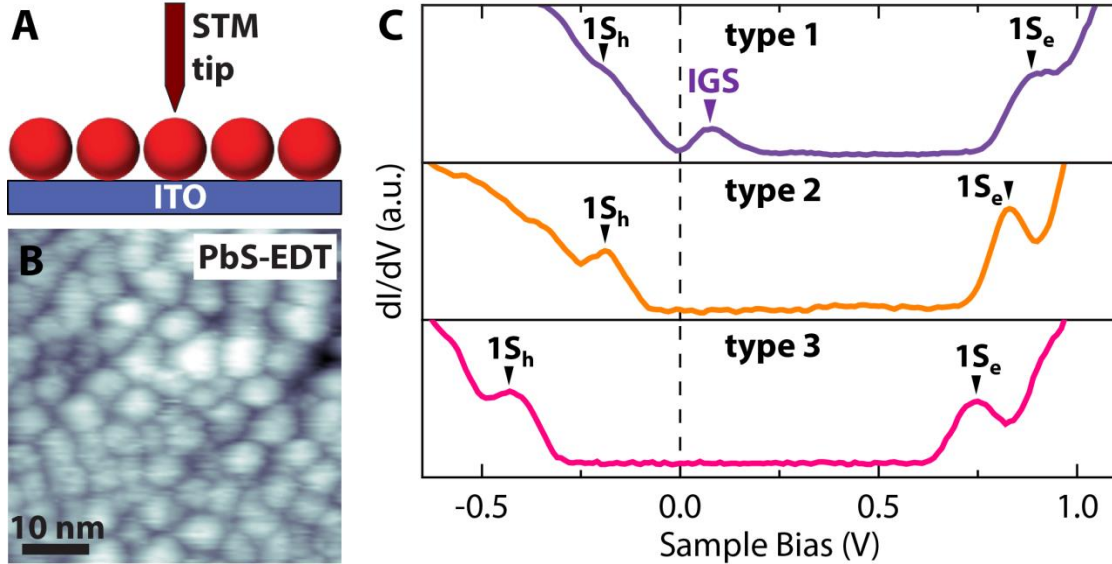


Figure 6.3. Electronic structure of individual PbS-EDT quantum dots. (A) Schematic diagram of STM and STS measurements of QDs deposited on an ITO substrate. (B) STM image with individually resolved PbS-EDT QDs. (C) STS curves of individual PbS-EDT QDs. The sample bias corresponds to the energy level position with respect to Fermi level. Three types of spectra are found, labeled according to the existence of in-gap states (IGS) and to $1S_h$ level alignment.

The observed conductivity of the IGS implies that they are partially delocalized to facilitate electron hopping from one IGS to the next. Since the IGS are empty states near the valence band, they induce p-type doping and pin the Fermi level in the ~ 0.2 eV gap between the IGS and $1S_h$ states. Since the type 2 spectra show p-type doping (Fermi level close to $1S_h$ states), they likely correspond to QDs with IGS whose wave function does not extend to the top surface and thus cannot be detected by the STM tip. The three types of STS spectra found on the QD solid indicates three types of QDs (Figure 6.4A): type 1 QDs have enough IGS to form conduction pathway; type 2 QDs have some amount of IGS so that the Fermi level is close to the valence band, but their wave functions do not overlap sufficiently to provide a conductive path; type 3 QDs have no or few IGS, and their Fermi level is farther away from the valence band. These three types of QDs are related with the three types of STS spectra, but not necessarily one-to-one correlated. When the QDs are randomly packed, electrons can hop via the IGS of type 1 QDs due to proper energy level alignment. Holes on the other hand can hop through the $1S_h$ state of most of type 1 and type 2 QDs. Type 3 QDs are electronically inactive, since they have no states near the Fermi level. The percolation pathway diagram for electrons and holes then resembles that shown schematically in Figure 6.4B, which illustrates how the Fermi level pins at $1S_h$ states or at IGS when holes or electrons are injected, respectively. It also shows that the hole percolation domains are different, and spatially larger, than those of electrons, in agreement with the experimental surface potential maps. The spatially connected patchy pathway structures resemble that of resistor networks, which have long been predicted by percolation theory.²⁸

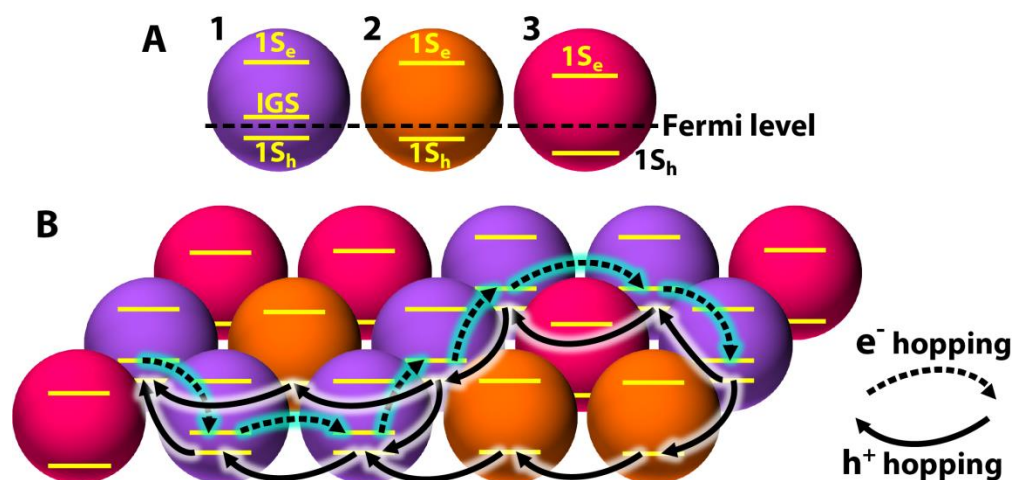


Figure 6.4. (A) Schematic diagram of the energy level alignment in the three types of QDs. (B) Schematic diagram illustrating the charge percolation pathways through 2-D arrays of PbS-EDT QDs. Electrons percolate through the IGS of type 1 QDs (dashed arrows), while holes hop via $1S_h$ states of type 1 and type 2 QDs (solid arrows).

We note that this IGS-induced Fermi level pinning is a general phenomenon occurring in all kinds of semiconductors.²⁹ Therefore percolation through IGS is energetically favored for at least one type of carriers if the defect concentration is sufficiently high to induce significant wave function overlap of adjacent IGS. QD solids, with their porous structure and larger surface area, are thus inherently suitable for engineering impurity conduction via chemical treatments.

6.5 Conduction Channel Switching and Intrinsic Quantum Dots

While a sufficient amount of IGS is beneficial for electron transport in QD solids under dark conditions, in photodiodes designed for transport of photoexcited charge carriers via valence/conduction bands, the deep IGS can act as recombination centers resulting in loss of efficiency. Previous studies showed that hydrazine (HYD) acts to increase the mobility of lead chalcogenide QDs which might be partially due to the removal of defect states.⁷ We thus performed HYD treatments to modulate the amount of IGS. We performed STS measurements on 43 individual HYD treated QDs (labeled PbS-HYD), and found that all of them have a clean bandgap with the Fermi level near the mid-gap (Figure 6.5B). This reveals that HYD is effective in removing the IGS, resulting in intrinsic QDs. The quantum confined peaks are smeared out in the dI/dV curve, but are evident after spectra renormalization (Figure 6.6).

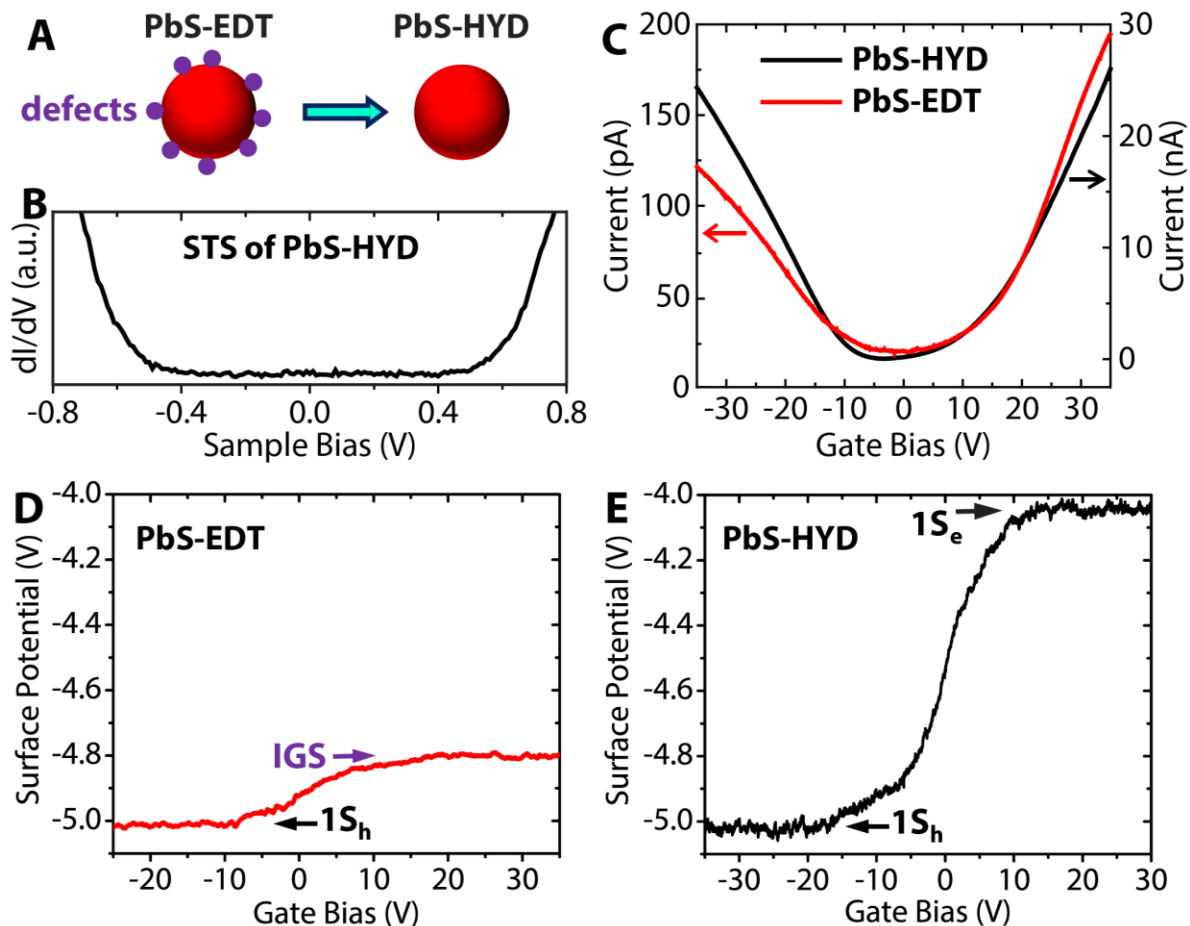


Figure 6.5. Surface defect engineering via chemical treatments. (A) Schematic diagram with surface defects present on PbS-EDT QDs but absent on PbS-HYD QDs. (B) STS curve of a PbS-HYD QD showing a clean bandgap with the Fermi level in the mid-gap. (C) Transfer curves from PbS-EDT and PbS-HYD QD thin film FETs, with a drain bias of -5 V. (D and E) Surface potential – gate bias spectra of the EDT and HYD treated samples. The surface potential is plotted in the same scale in the two figures.

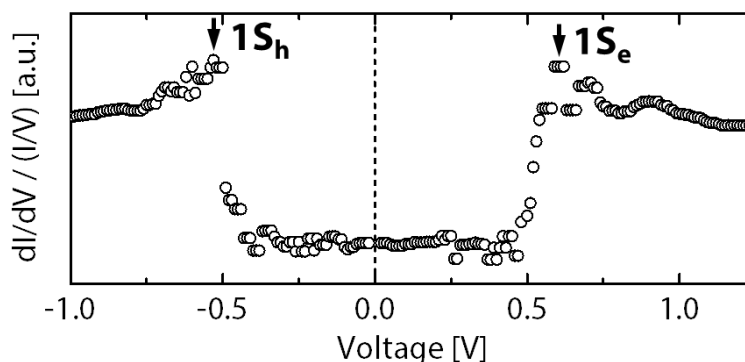


Figure 6.6. Normalized STS curve ($dI/dV/(I/V)$) of a PbS-HYD QD. The raw dI/dV curve is shown in Figure 6.5B.

To compare the charge transport properties of the QDs with and without IGS, we measured the source-drain current (I_d) versus gate bias curves (transfer curves) of PbS-EDT and PbS-HYD QD thin film FETs, with a small bias $V_d = -5 V$ applied to the drain and with the source grounded. The slope in the linear part of the curves (Figure 6.5C) is proportional to the carrier mobility in the states involved in the transport.²⁹ We can see that the EDT and HYD treated QD arrays are both ambipolar, with electron conduction at positive gate bias, and hole conduction at negative gate bias. PbS-HYD shows similar electron (μ_e) and hole mobility (μ_h), while PbS-EDT shows $\mu_e \approx 2.2\mu_h$. The electronic levels involved in charge transport can also be measured with KPFM by means of surface potential (V_{sf}) – gate bias (V_g) spectroscopy²⁵ with the tip placed above the QDs (Figure 4D, E), with source and drain electrodes grounded. The curves in Figure 6.5D show that for PbS-EDT, V_{sf} is pinned by the $1S_h$ states and by the IGS, in agreement with the proposed mechanism of hole transport via $1S_h$ state and electron transport via IGS. The larger electron mobility (compared to hole mobility) indicates good coupling of IGS between QDs. In contrast, the curves in Figure 6.5E reveal that V_{sf} is pinned by the $1S_h$ and $1S_e$ states (conduction band) at high negative/positive gate bias, respectively. The nearly linear transition of the surface potential from the $1S_h$ to $1S_e$ states also confirms the absence of IGS.²⁵ This is in agreement with the STS and transport results, confirming that hole transport occurs via $1S_h$ states while electron transport occurs via $1S_e$ states in the case of PbS-HYD. For PbS QDs the electrons in the $1S_h$ state and the holes in the $1S_e$ state have the same effective mass,²³ resulting in similar mobility. KPFM imaging of PbS-HYD at $V_g = \pm 52 V$ reveals that electron and hole follows the same pathways (Figure 6.7), further confirming the conduction/valence band transport mechanism.

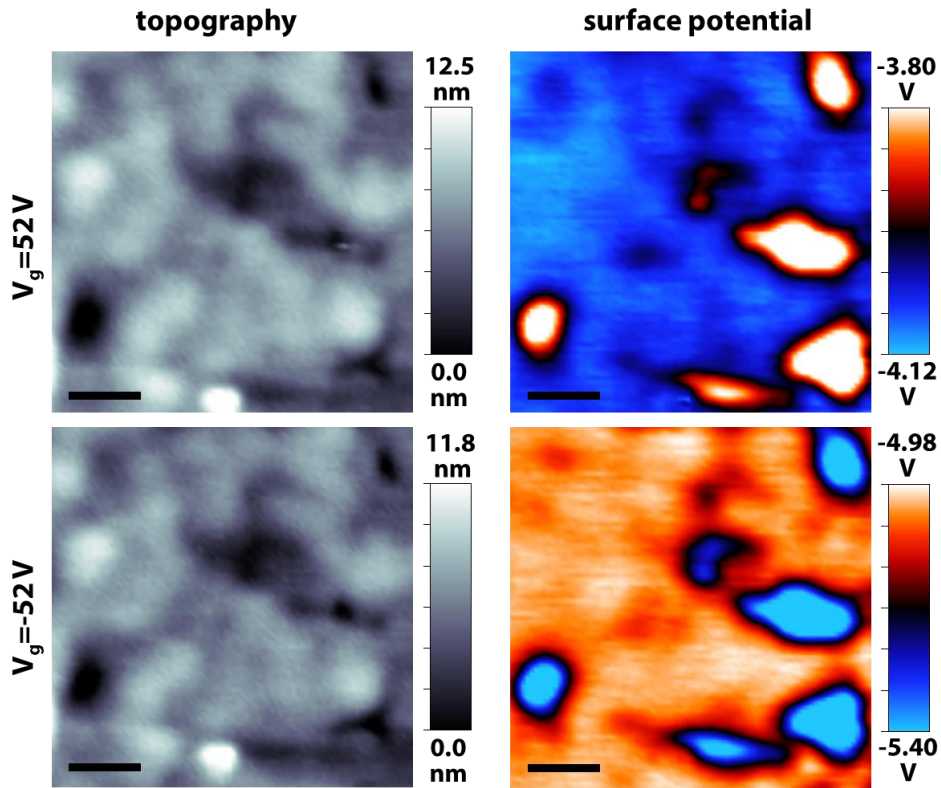


Figure 6.7. Topography (left) and surface potential (right) images of PbS-HYD with $V_g = \pm 52 V$, as labeled. Scale bar: 100 nm.

The electron/hole mobility in the localized hopping transport regime not only depends on the percolation domain size, but also on the electronic coupling of neighboring states (β), dispersion of state energy ($\Delta\alpha$), and Coulomb charging energy (E_c).^{7,30} For lead chalcogenide nanocrystals, E_c is typically small and can be neglected at room temperature.^{7,23} β depends on the localization of the transport states and the distance between neighboring states, which is hard to quantify for the IGS. As to $\Delta\alpha$, STS results show that the $1S_h$ state is more dispersed than the IGS for the PbS-EDT QDs. A smaller $\Delta\alpha$ could be responsible for the fact that $\mu_e > \mu_h$ for the 2-D PbS-EDT arrays studied here. Comparing PbS-HYD and PbS-EDT QDs, the former have a much higher surface coverage (95% vs 59%, as determined from AFM images), and a larger β due to the smaller inter-particle distance (since the PbS-HYD QD surface is almost bare, as revealed by infrared absorption measurements). These two factors are responsible for the larger measured μ_e and μ_h of PbS-HYD compared to those of PbS-EDT. The submonolayer coverage is responsible for the much smaller source-drain current compared to that of thin films (typically ~50 nm thick).

6.6 Discussion and Conclusion

There has been many postulations regarding the atomic origin of IGS in lead chalcogenide QDs, including incomplete ligand passivation,³¹ non-stoichiometry,^{32,33} and surface oxidation.³⁴⁻³⁶ Here we found that hydrazine, a strong reducing agent, can efficiently remove IGS. Our results thus indicate that oxygen-related species are likely at the origin of the conductive IGS, although we cannot rule out other possibilities. We also note that there may exist shallow trap states within thermal energy from the valence/conduction band edge, which cannot be distinguished from the $1S_h/1S_e$ states due to the resolution limit of the STM and KPFM.

The phenomenon of ambipolar transport with larger electron mobility has also been reported for PbSe QD thin films treated with EDT.^{15,36} Therefore, we expect the mechanism of electron transport through IGS to be generally applicable to lead chalcogenide QD solids with EDT treatments under dark conditions in a FET geometry.

One promising application of QD solids is in large area, flexible electronics, such as transistors, circuits, memory, and sensors.³⁷ These devices can be fabricated by room temperature, roll-to-roll solution processing, which reduces cost. However, the fabricated QD films are more prone to defects and impurities compared to traditional high-temperature, vacuum processed crystalline semiconductors. In contrast to the traditional view that defects act simply as traps hindering carrier transport, this work shows the beneficial role of impurities, and can thus serve as the starting point for engineering conductive impurities that can be controlled during solution processing. The mechanism of in-gap state induced Fermi level pinning and favorable charge percolation via IGS is likely to be relevant to other QD and organic semiconductor systems as well.

On the other hand, for QD based optoelectronic devices in diode geometries, the goal is to harness the photoexcited charge carriers that are transported via conduction/valence band states. In contrast to the (quasi-)equilibrium process of electrostatic field-controlled charge injection and transport in the linear regime in the FETs, photocarrier transport in diodes are inherently a non-equilibrium process that requires constant pumping of carriers into valence/conduction band

states. In the latter case, conduction through IGS is unlikely since electrons in IGS would quickly recombine with holes in the $1S_h$ states due to their small energy level separation (0.2 eV). But electrons in the $1S_e$ states would be able to travel (through drift and diffusion) a finite distance (100–300 nm) before recombination with IGS or $1S_h$ states.^{5,6,9,31,38,39} Solar cell measurements using our PbS-EDT QDs provides an open-circuit voltage larger than 0.2 eV (not shown here), confirming that photoexcited electron transport occurs through the conduction band.

Considering that PbS-HYD was found to be intrinsic with no deep IGS, it is likely that these QDs would have a low photocarrier recombination rate and a large carrier diffusion length. Therefore, by designing p-i-n photodiodes with PbS-HYD as the intrinsic layer, we may be able to achieve much higher efficiencies in solar cells and photodetectors.^{38,39}

References

1. Huynh, W. U.; Dittmer, J. J.; Alivisatos, A. P. *Science* **2002**, 295, 2425–2427.
2. Cui, Y.; Lieber, C. M. *Science* **2001**, 291, 851–853.
3. Tessler, N.; Medvedev, V.; Kazes, M.; Kan, S.; Banin, U. *Science* **2002**, 295, 1506–1508.
4. Graetzel, M.; Janssen, R. A. J.; Mitzi, D. B.; Sargent, E. H. *Nature* **2012**, 488, 304–312.
5. Chuang, C. M.; Brown, P. R.; Bulović, V.; Bawendi, M. G. *Nat. Mater.* **2014**, 13, 786–801.
6. Ning, Z.; Voznyy, O.; Pan, J.; Hoogland, S.; Adinolfi, V.; Xu, J.; Li, M.; Kirmani, A. R.; Sun, J.-P.; Minor, J.; Kemp, K. W.; Dong, H.; Rollny, L.; Labelle, A.; Carey, G.; Sutherland, B.; Hill, I.; Amassian, A.; Liu, H.; Tang, J.; Bakr, O. M.; Sargent, E. H. *Nat. Mater.* **2014**, 13, 822–828.
7. Talapin, D. V.; Murray, C. B. *Science* **2005**, 310, 86–89.
8. Lee, J.; Kovalenko, M. V.; Huang, J.; Chung, D. S.; Talapin, D. V. *Nat. Nanotechnol.* **2011**, 6, 348–352.
9. Clifford, J. P.; Konstantatos, G.; Johnston, K. W.; Hoogland, S.; Levina, L.; Sargent, E. H. *Nat. Nanotechnol.* **2009**, 4, 40–44.
10. Wolkin, M. V.; Jorne, J.; Fauchet, P. M.; Allan, G.; Delerue, C. *Phys. Rev. Lett.* **1999**, 82, 197–200.
11. Cordones, A. A.; Scheele, M.; Alivisatos, A. P.; Leone, S. R. *J. Am. Chem. Soc.* **2012**, 134, 18366–18373.
12. Diaconescu, B.; Padilha, L. A.; Nagpal, P.; Swartzentruber, B. S.; Klimov, V. I. *Phys. Rev. Lett.* **2013**, 110, 127406.
13. Nagpal, P.; Klimov, V. I. *Nat. Commun.* **2011**, 2, 486.
14. Jeong, K. S.; Tang, J.; Liu, H.; Kim, J.; Schaefer, A. W.; Kemp, K.; Levina, L.; Wang, X. H.; Hoogland, S.; Debnath, R.; Brzozowski, L.; Sargent, E. H.; Asbury, J. B. *ACS Nano* **2012**, 6, 89–99.
15. Liu, Y.; Gibbs, M.; Puthussery, J.; Gaik, S.; Ihly, R.; Hillhouse, H. W.; Law, M. *Nano Lett.* **2010**, 10, 1960–1969.
16. Bozyigit, D.; Volk, S.; Yarema, O.; Wood, V. *Nano Lett.* **2013**, 13, 5284–5288.
17. Drndić, M.; Markov, R.; Jarosz, M. V.; Bawendi, M. G.; Kastner, M. A.; Markovic, N.; Tinkham, M. *Appl. Phys. Lett.* **2003**, 83, 4008–4010.
18. Anderson, P. W. *Phys. Rev.* **1958**, 109, 1492–1605.
19. Le Comber, P. G.; Spear, W. E. *Phys. Rev. Lett.* **1970**, 25, 509–511.

20. Mott, N. F.; Twose, W. D. *Adv. Phys.* **1961**, 10, 107–163.
21. Coropceanu, V.; Cornil, J.; da Silva, D. A.; Olivier, Y.; Silbey, R.; Bredas, J. L. *Chem. Rev.* **2007**, 107, 926–952.
22. Elliott, R. J.; Krumhansl, J. A.; Leath, P. L. *Rev. Mod. Phys.* **1974**, 46, 465–543.
23. Kang, I.; Wise, F. W. *J. Opt. Soc. Am. B* **1997**, 14, 1632–1646.
24. Zherebetsky, D.; Scheele, M.; Zhang, Y.; Bronstein, N.; Thompson, C.; Britt, D.; Salmeron, M.; Alivisatos, P.; Wang, L.-W. *Science* **2014**, 344, 1380–1384.
25. Zhang, Y.; Ziegler, D.; Salmeron, M. *ACS Nano* **2013**, 7, 8258–8265.
26. Zhang, Y.; Pluchery, O.; Caillard, L.; Lamic-Humblot, A.-F.; Casale, S.; Chabal, Y. J.; Salmeron, M. *Nano Lett.* **2015**, 15, 51–55.
27. Jasieniak, J.; Califano, M.; Watkins, S. E. *ACS Nano* **2011**, 5, 5888–5902.
28. Kirkpatrick, S. *Rev. Mod. Phys.* **1973**, 45, 574–588.
29. Sze, S. M. *Physics of Semiconductor Devices*, 2nd Edition; Wiley: New York, 1981.
30. Remacle, F.; Levine, R. D. *ChemPhysChem* **2001**, 2, 20–36.
31. Ip, A. H.; Thon, S. M.; Hoogland, S.; Voznyy, O.; Zhitomirsky, D.; Debnath, R.; Levina, L.; Rollny, L. R.; Carey, G. H.; Fischer, A.; Kemp, K. W.; Kramer, I. J.; Ning, Z. J.; Labelle, A. J.; Chou, K. W.; Amassian, A.; Sargent, E. H. *Nat. Nanotechnol.* **2012**, 7, 577–582.
32. Kim, D.; Kim, D.-H.; Lee, J.-H.; Grossman, J. C. *Phys. Rev. Lett.* **2013**, 110, 196802.
33. Oh, S. J.; Berry, N. E.; Choi, J.-H.; Gauldin, E. A.; Paik, T.; Hong, S.-H.; Murray, C. B.; Kagan, C. R. *ACS Nano* **2013**, 7, 2413–2421.
34. Leschkies, K. S.; Kang, M. S.; Aydil, E. S.; Norris, D. J. *J. Phys. Chem. C* **2010**, 114, 9988–9996.
35. Zarghami, M. H.; Liu, Y.; Gibbs, M.; Gebremichael, E.; Webster, C.; Law, M. *ACS Nano* **2010**, 4, 2475–2485.
36. Luther, J. M.; Law, M.; Song, Q.; Perkins, C. L.; Beard, M. C.; Nozik, A. J. *ACS Nano* **2008**, 2, 271–280.
37. Kim, D. K.; Lai, Y.; Diroll, B. T.; Murray, C. B.; Kagan, C. R. *Nat. Commun.* **2012**, 3, 1216.
38. Zhitomirsky, D.; Voznyy, O.; Levina, L.; Hoogland, S.; Kemp, K. W.; Ip, A. H.; Thon, S. M.; Sargent, E. H. *Nat. Commun.* **2014**, 5, 3803.
39. Engel, J. H.; Alivisatos, A. P. *Chem. Mater.* **2014**, 26, 153–162.

Chapter 7: Time-Resolved Local Probe of Carrier Trapping Dynamics

Reproduced in part and adapted with permission from Nano Letters

DOI: 10.1021/acs.nanolett.5b01429

Copyright © 2015, American Chemical Society.

7.1 Abstract

Non-crystalline semiconductor materials often exhibit hysteresis in charge transport measurements, whose mechanism is largely unknown. Here we study the dynamics of charge injection and transport in PbS quantum dot (QD) monolayers in a field effect transistor (FET). Using Kelvin probe force microscopy, we measured the temporal response of the QDs as the channel of a FET, following step function changes of gate bias. These measurements reveal an exponential decay of mobile carrier density with time constants of 3–5 s for holes and ~10 s for electrons. Ohmic behavior with uniform carrier density was observed along the channel during the injection and transport processes. These slow, uniform carrier trapping processes are reversible, with time constants that depend critically on the gas environment. We propose that the underlying mechanism is some reversible electrochemical processes involving dissociation and diffusion of water and/or oxygen related species. These trapping processes are dynamically activated by the injected charges, in contrast with static electronic traps whose presence is independent of the charge state. Understanding and controlling these processes is important for improving the performance of electronic, optoelectronic, and memory devices based on disordered semiconductors.

7.2 Introduction

Colloidal quantum dots (QDs), with tunable band gap and electronic structure, are being explored for various electronic and optoelectronic device applications, such as field effect transistors (FETs), photodetectors, and solar cells.^{1–4} The last decade has seen tremendous progress in the optimization of QD based devices, focusing on controlling surface capping ligands for better surface passivation and enhanced carrier mobility and lifetime.⁵ Despite all these efforts, an intriguing phenomenon that still remains poorly understood is charge carrier trapping, which is observed in all kinds of QD systems.^{6–10} For individual QDs, the long standing mystery of fluorescence blinking phenomena is thought to be related to charge trapping in defect states, although the nature of the defects and trapping mechanism is not understood.^{8–10} For QD devices, deep traps assist carrier recombination (Shockley-Read-Hall recombination), limiting the optoelectronic device efficiency. Shallow traps, on the other hand, can be utilized to enhance carrier lifetime for improving the gain in photoconductors.^{2,11} In FETs that operate under dark conditions, although it has been recently observed that certain deep defect states can actually assist carrier transport,^{7,12} QD films still suffer from significant hysteresis effects where the source-drain current decays substantially in the scale of seconds after charge injection.¹³ These effects were found to be independent of the gate dielectric, and were thus attributed to the intrinsic properties of PbS QDs. However, no quantitative information of carrier density was presented and the carrier trapping mechanism is still unresolved. Traditional methods of carrier dynamics analysis (e.g. photoluminescence, transient absorption and transient photocurrent,

current-voltage, and capacitance voltage measurements) provide insights into the trapping behavior but have so far failed to uncover the underlying microscopic mechanisms.^{9,14}

In this work, we employ Kelvin probe force microscopy (KPFM) to analyze the hysteresis behavior of charge injection and transport in monolayers of PbS QDs. Previous work on the hysteresis in QD FETs only measured source-drain current which is a convolution of charge injection and transport,¹³ and possibly contact resistance. Moreover the transport current has contribution from both mobility and carrier density. Here we directly measure the transient behavior of carrier density, which we believe can clarify the mechanism of charge trapping.

7.3 Experimental Setup

The schematic of the FET and KPFM setup used in our measurements is shown in Figure 7.1a. PbS QDs with 5.5 nm diameter and 0.9 eV bandgap were deposited on the FET substrates passivated with octadecyltrichlorosilane (OTS) to remove oxide surface charge traps. The QDs were treated with 1,2-ethanedithiol (EDT) which replaces the native oleate ligands on the surface, reduces the inter-particle distance and activate charge transport^{12,15,16}. Previous work by Nagpal *et al.* indicates that in-gap states (IGS) can assist carrier transport in the EDT treated PbS QD films.⁷ Our previous results showed that under dark conditions hole transport occurs via valence band ($1S_h$) states, while electron transport takes place via IGS (Figure 7.1b) ~ 0.2 eV above the $1S_h$ states.¹²

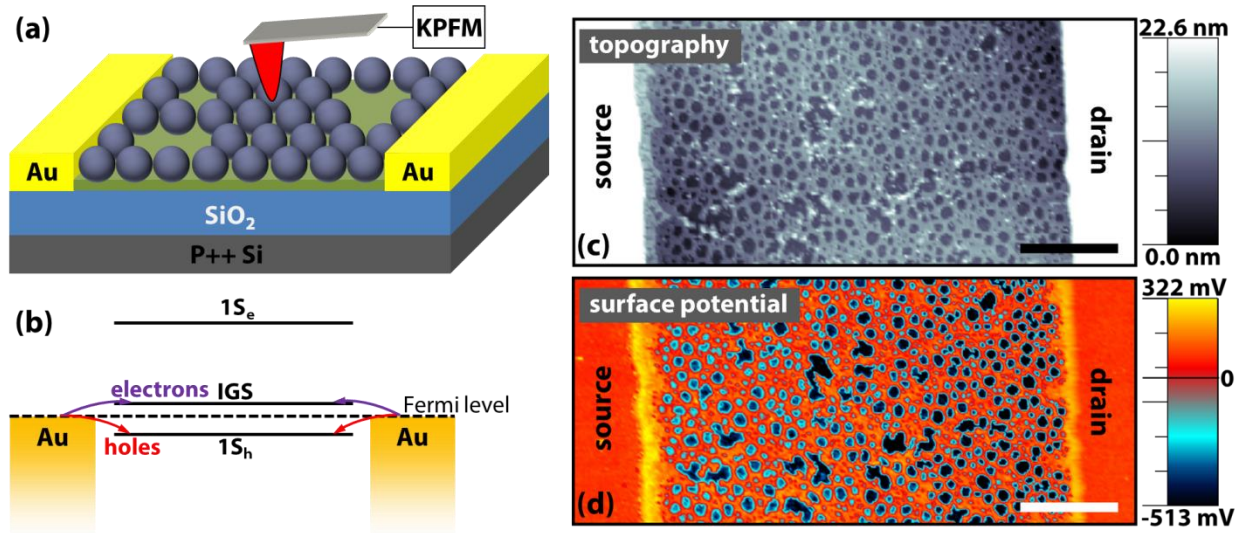


Figure 7.1. Schematic setup of the Kelvin probe force microscopy (KPFM) and FET measurement. (a) Schematic PbS QD sub-monolayer FET probed by KPFM. Channel length is $\sim 20 \mu\text{m}$, width is 1mm . Oxide thickness is 300nm . The green layer on the SiO_2 is an OTS monolayer. (b) Energy level alignment diagram of the FET. The Fermi level in the QDs is between the in-gap states (IGS) and the valence band ($1S_h$) states. The IGS are responsible for electron transport in the dark. (c) and (d) are topographic and surface potential maps of the FET. Scale bar: $4 \mu\text{m}$. The brighter parts in the channel region in (c) are the QD monolayer, corresponding to the higher surface potential regions in (d). The darker spots (with lower surface

potential) in the channel correspond to the OTS passivated oxide surface which is not covered by QDs.

A home-built single pass, frequency modulation KPFM was implemented based on an atomic force microscope (AFM), and used for surface potential measurements with a resolution around 10 mV.^{12,17} All the measurements were done in an inert nitrogen atmosphere (with a relative humidity of <0.5%, the detection limit of our hygrometer), except when specially noted. During KPFM measurements, a $V_{DC} + V_{AC}\cos\omega t$ bias is applied to the metal-coated AFM tip, with $V_{AC} = 2 V$, $\omega = 2 \text{ kHz}$. With the sample grounded, the AC tip bias yields components of the cantilever phase shift at ω and 2ω , respectively:

$$\Delta f_{\omega} \propto \frac{\partial^2 C}{\partial z^2} (CPD - V_{DC}) V_{AC}, \quad (7.1)$$

$$\Delta f_{2\omega} \propto \frac{\partial^2 C}{\partial z^2} V_{AC}^2, \quad (7.2)$$

where CPD is the tip-sample contact potential difference, C is the capacitance between AFM tip and the sample, and z is the tip-sample distance. V_{DC} is adjusted to maintain $\Delta f_{\omega} = 0$, and at the same time V_{DC} is recorded as the CPD. The surface potential (V_{sf}) signal of the sample is obtained from CPD calibrated by setting the CPD of the nearby grounded Au electrode (here the deposited QDs were scratched away) to zero. Since the work function of Au (5.1 eV) is the same as that of the gate (p++ Si substrate), the calibrated value of V_{sf} corresponds to the actual potential difference between the channel and the gate in the FET. $\Delta f_{2\omega}$ is also recorded as the $\partial^2 C / \partial z^2$ signal, providing information on the tip-sample capacitance. The spatial resolution of the V_{sf} and $\partial^2 C / \partial z^2$ signal is 20–50 nm.

The charge injected into the PbS film following a step change in gate bias can be followed by measuring V_{sf} as a function of time. The charge density can be obtained using the capacitor relation:

$$N = \frac{C_{ox}}{t_c e} |V_g - V_{sf}| \quad (7.3)$$

where C_{ox} is the capacitance per unit area of the SiO_2 , t_c is the channel thickness (~5.5 nm), and e is the absolute value of the elementary charge. Meanwhile, the capacitance signal ($\partial^2 C / \partial z^2$) is a measure of mobile carrier density N_m (density of free moving carriers in response to the tip's AC bias with $\omega = 2 \text{ kHz}$).¹⁸

The simultaneously recorded topography and surface potential images of a FET channel area is shown in Figure 7.1c,d. The images show that the QD film has submonolayer coverage, with a porous structure connecting the source and drain electrodes. At a gate bias $V_g=0$, the V_{sf} of the QDs in the channel region is 150–200 mV, 500–600 mV higher than that of the OTS passivated oxide surface (Figure 7.2).

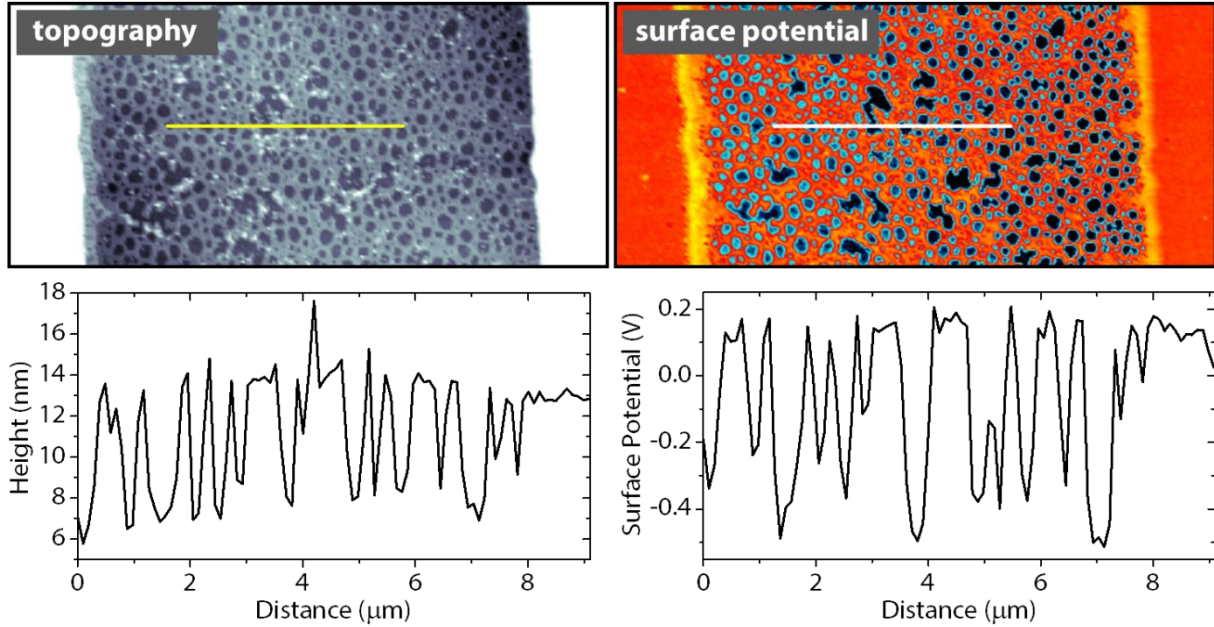


Figure 7.2. Top panels are topography and surface potential images, same as Figure 7.1c,d. Bottom panels are the cross-section profiles corresponding to the line in the top panels. The height of one layer of QDs is shown to be ~ 7 nm, as expected from the QD diameter of ~ 5.5 nm and the EDT ligand length of 0.5–1 nm.

7.4 Charge Trapping Dynamics upon Injection

With the tip placed 5–10 nm above the QD monolayer in the channel region, we probed the transient charge injection and relaxation process by simultaneously recording the source current (current flowing out of the source electrode), surface potential, and $\partial^2 C / \partial z^2$ following a step change in the gate bias (Figure 7.3). Previously we found that at steady state V_{sf} is pinned at $1S_h$ states and at IGS when $V_g < \sim -15$ V and when $V_g > \sim 15$ V.¹² We thus applied a gate bias step from 0 to ± 26 V to inject carriers into conductive states (Figure 7.3a,b), with source and drain grounded. Figure 7.3c–f show the temporal response of V_{sf} and $\partial^2 C / \partial z^2$ following the bias step. Since no source-drain bias was applied, there is no steady-state current, although we did observe transient current due to slow charge injection into the channel (Figure 7.4). The surface potential transients can be fitted with single exponential decays, with $\tau = 2.8$ s and 11.0 s for holes and electrons, respectively. The $\partial^2 C / \partial z^2$ transients also follow exponential decays, with $\tau = 3.7$ s and 9.5 s for holes and electrons, respectively. In both transients the electron relaxation time is longer than that of hole relaxation. A different gate bias of ± 39 V was applied and the time constants were found to be similar.

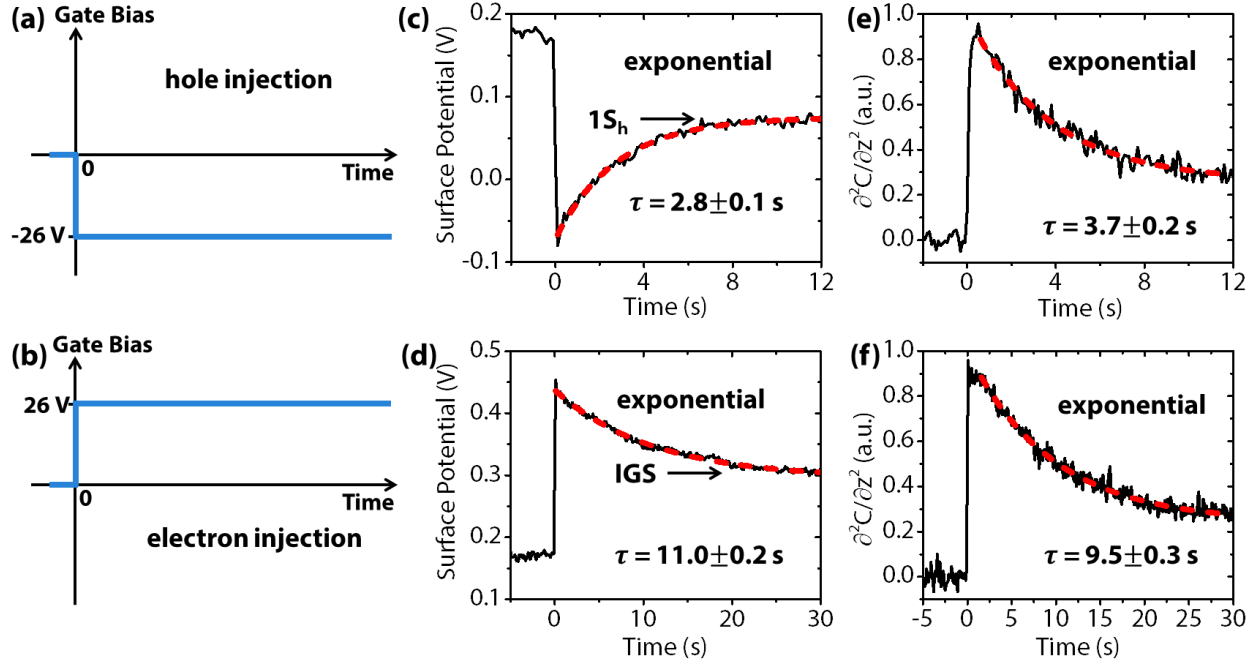


Figure 7.3. Charge injection dynamics of PbS QD FETs. (a) and (b) show the ∓ 26 V gate bias step function applied at time zero to inject holes and electrons, respectively. (c-f) Transient dynamics of surface potential and capacitance ($\partial^2 C / \partial z^2$) as labeled. Upper panels corresponds to hole injection, while lower panels correspond to electron injection. Black solid curves are raw data, while red dashed curves are fittings. The fitting parameters together with the standard errors are shown in each figure. The long-time equilibrium surface potential values correspond to the $1S_h$ states and IGS, for holes and electrons respectively, as marked in (c) and (d).

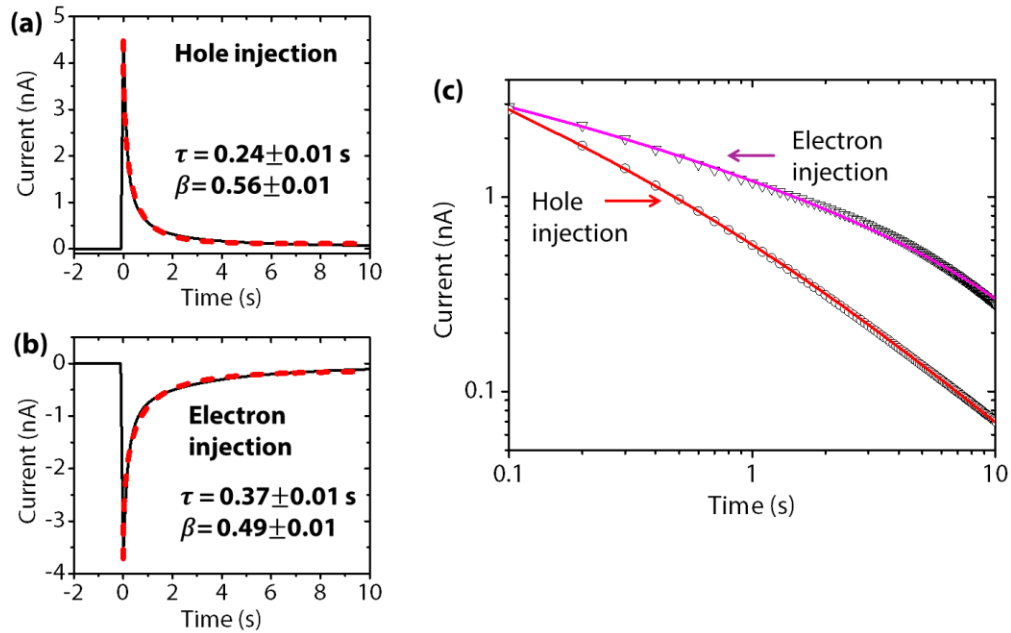


Figure 7.4. Transient injection currents (raw data and stretched exponential fits) upon the gate bias step from 0 V to -26 V (a) and from 0 V to 26 V (b). (c) shows the two transients in log-log scale (in absolute value).

The V_{sf} and $\partial^2 C / \partial z^2$ transients, measured inside the channel, were found to be independent of the distance to the source/drain electrodes, revealing that the observed transients are not due to charge diffusion inside the QDs. Upon hole injection, V_{sf} increases from -0.08 V to 0.08 V, corresponding to a slight increase of charge density from $3.39 \times 10^{18} \text{ cm}^{-3}$ to $3.41 \times 10^{18} \text{ cm}^{-3}$ (calculated using eq 7.3), as shown in Figure 7.5a. For electrons, V_{sf} decreases from 0.44 V to 0.30 V, corresponding to a minute increase of charge density from $3.34 \times 10^{18} \text{ cm}^{-3}$ to $3.36 \times 10^{18} \text{ cm}^{-3}$ (eq 7.3, Figure 7.5b). In contrast, the $\partial^2 C / \partial z^2$ signal, a measure of mobile carrier density, decreased significantly (Figure 7.3e,f). The capacitance curves are linearly normalized such that $\partial^2 C / \partial z^2$ is 0 at $t < 0$ and 1 at $t = 0$ (determined by the exponential fit). Assuming that the injected charge carriers are all mobile at $t = 0$ (with an initial density of N_0), the mobile carrier density can be written as

$$N_m = N_0 \partial^2 C / \partial z^2 \quad (7.4)$$

when $t > 0$. The trapped carrier density can thus be obtained as

$$N_t = N_0 - N_m \quad (7.5)$$

The mobile and trapped density of holes and electrons determined from eqs 4 and 5 are shown in Figure 7.5a,b. We can see that the initially injected free carriers gradually become immobile, in the time scale of 3.7 s for holes and 9.5 s for electrons. The density of mobile carriers decreases significantly during the transient trapping process, to ~30% of the initial value in 12 s for holes and in 30 s for electrons.

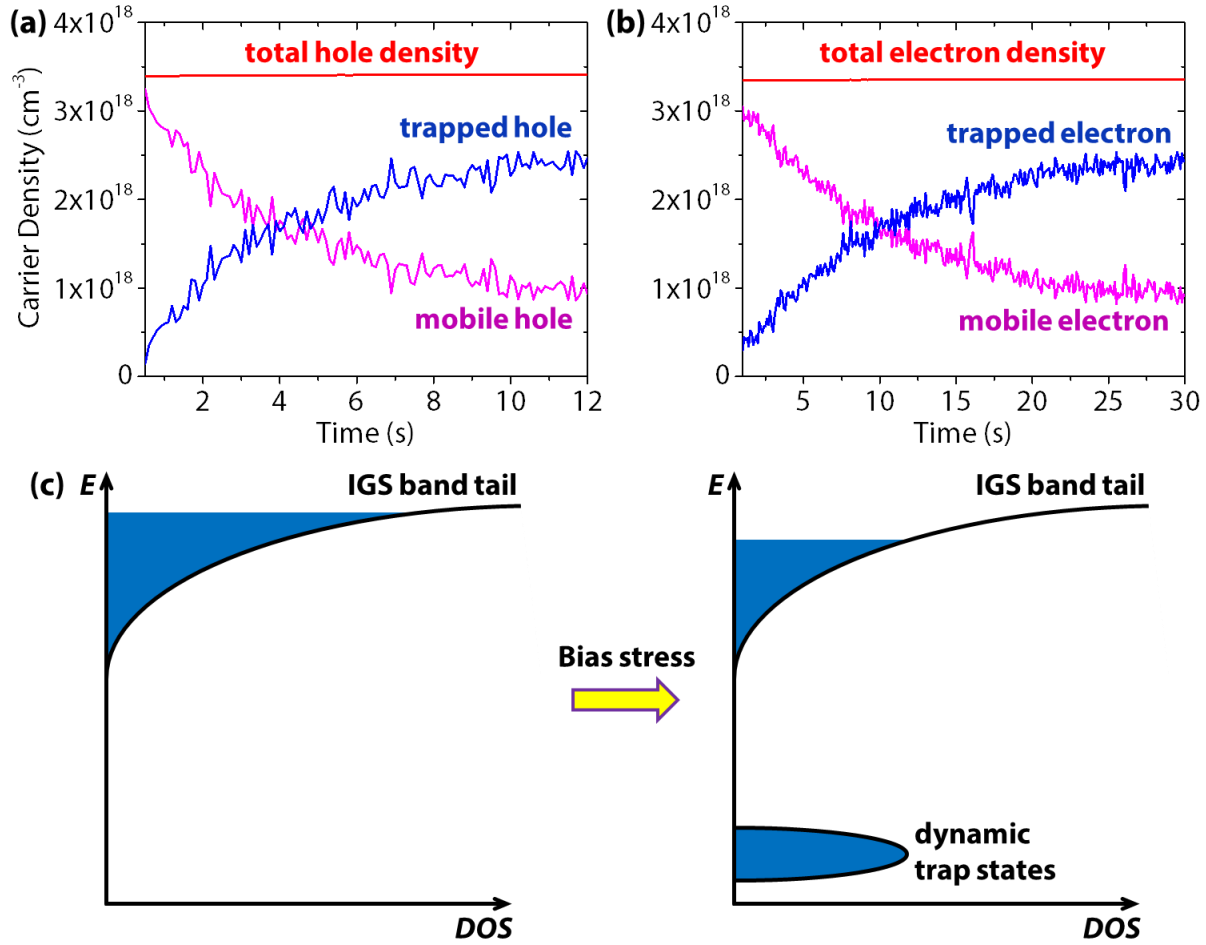


Figure 7.5. Dynamic carrier trapping mechanism. (a) and (b) show the carrier density decay of holes and electrons, respectively (after the ∓ 26 V gate bias), including the total density, mobile, and trapped carrier density. (c) Left schematic shows that the injected electrons fill part of the IGS band (blue region) right after charge injection. The right schematic shows that the trap states are created after charge injection, which capture electrons from the IGS and gradually become filled. These dynamic traps, which may not exist before charge injection, can have an energy level lower than the $1S_h$ states.

Due to insufficient screening of the gate field during charge injection,¹⁷ the actual Fermi level change can only be smaller than the change of eV_{sf} (~ 0.15 eV). Since the final V_{sf} level matches well with the IGS for electron injection and with valence band states for hole injection, we can conclude that the charges were initially injected into the IGS/ $1S_h$ states and were gradually trapped, with a slight change of Fermi level. The proposed mechanism of the carrier relaxation transients is shown in Figure 7.5c. Since the decay of carrier density is a single exponential, we expect that a single trapping process is dominant. Hole injection follows the same trend as in the case of electrons, i.e., the holes gradually falling into traps above the valence band edge.

7.5 Charge Transport Dynamics upon Injection

Having observed the transient charge trapping dynamics upon charge injection in PbS QD FETs, where source and drain electrodes were grounded all the time, we proceed to measure the transport dynamics by applying a drain bias $V_d = -5$ V (source still grounded). The same gate bias step from 0 to ± 26 V was applied.

The measured transient source currents are shown in Figure 7.6. We found that the current transients for both holes and electrons consist of an initial sharp spike followed by a long tail, which we attribute to injection current and source-drain transport current, respectively. This is evident in the electron current (Figure 7.6b) as injection and transport currents have different signs due to the reverse sign between V_g and V_d . Since $V_d \ll V_g$, we expect the injection currents to follow the same stretched exponential decays (same time constant τ and stretching exponent β parameters) as that in Figure 7.4, occurring in sub-second time scales. We can thus assign the transient currents for $t > 6$ s (when injection currents are negligible) to pure transport currents, which are best fitted with exponential decays shown in the insets of Figure 7.6a,b. For holes and electrons, we obtained $\tau = 5.0$ s and $\tau = 8.7$ s for the transport current, respectively. These time constants are similar to the capacitance transients in Figure 7.3e,f, revealing that carrier trapping is likely the major factor responsible for the decay in transport current, which is proportional to the density of mobile carriers

$$J = en\mu E \quad (7.6)$$

Here J is the current density, n is the mobile carrier density, μ is the mobility, and E is the in-plane electric field. A decrease in n results in a decrease in J , provided that μ does not change significantly.

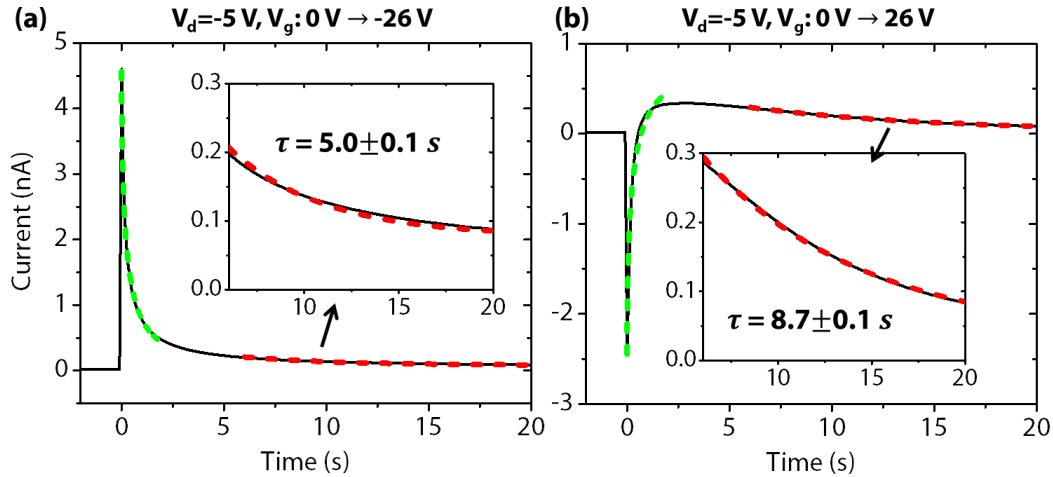


Figure 7.6. Current injection and transport dynamics at a drain bias of $V_d = -5$ V, after the application of a gate bias step from zero to ∓ 26 V, as labeled. (a) and (b) corresponds to hole and electron dynamics. Insets are expansions of the curves in the 6–20 s time window.

Under a finite drain bias, the local surface potential cross section along the channel reveals the electric field distribution ($E = \partial V_{sf} / \partial x$) from which we can infer the transport mechanism (Ohmic, space-charge-limited, contact-limited, *etc.*). We thus analyzed the transient V_{sf} distributions upon the application of gate bias, as shown in Figure 7.7a,b. We can see that V_{sf} profile remains unchanged during hole injection and transport (Figure 7.7a), with linear decrease

from source to drain characteristic of Ohmic conduction. No voltage drop is observed at the source and drain contacts, revealing that the metal-semiconductor contact is also Ohmic, as expected since the Fermi level of Au and the valence band of the PbS QDs are well aligned.¹² In contrast, the V_{sf} profile in the n-channel (electron transport) shows a transient voltage drop at the negatively biased drain electrode from which electrons were injected (Figure 7.7b), although Ohmic conduction inside the channel is still preserved (as evident by the linear V_{sf} decrease inside the channel). As shown in Figure 7.7c, the voltage drop at the drain contact follows exponential decay, decreasing from ~ 2 V at $t=0$ to ~ 0.3 V at $t=28$ s. The contact resistance is thus $2/3$ of the channel resistance in the beginning and negligible in the end. However, the time constant of the contact voltage drop (ΔV) is 11.6 s, similar with that of the electron transport current (I) (Figure 7.6b). Therefore, the contact resistance ($\Delta V/I$) is roughly constant with a value of ~ 5 G Ω , while the channel resistance increases during the nonequilibrium charge injection and transport process. The contact resistance is likely due to the ~ 0.3 eV mismatch of the IGS position with that of the Au Fermi level.¹² The fact that the contact resistance remains unchanged further supports our proposed carrier trapping mechanism (Figure 7.5c), where the Fermi level of the injected carriers only slightly changes during the charge trapping process.

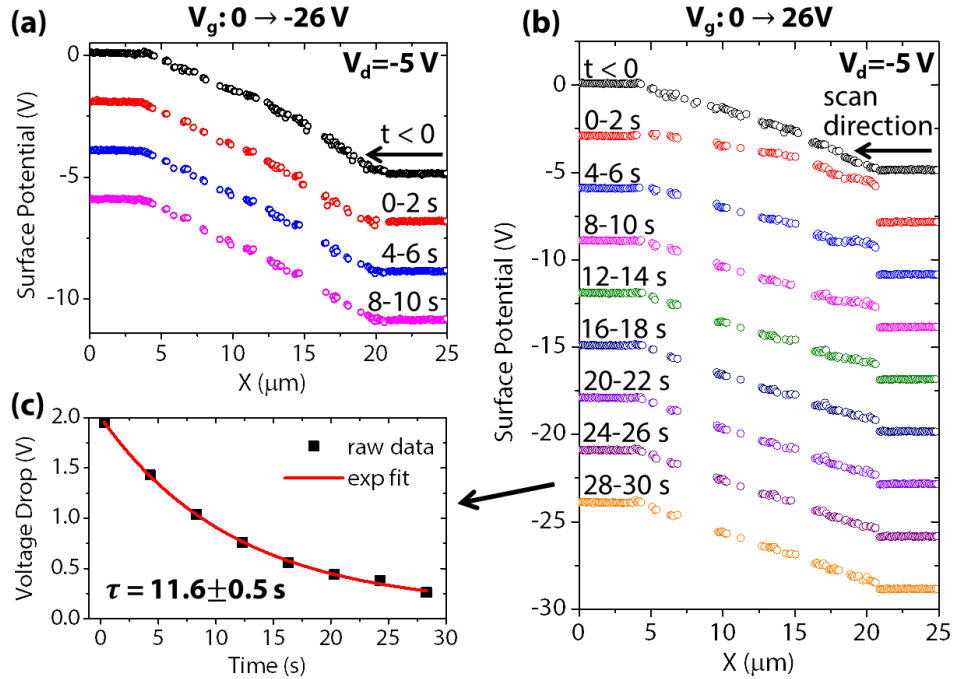


Figure 7.7. Dynamics of the surface potential profile across the channel at $V_d = -5$ V, after the application of a gate bias step of ∓ 26 V. (a) and (b) corresponds to hole and electron dynamics, and each curve corresponds to the full surface potential profile covering the source (left), channel (middle) and drain (right). The tip scanned from the right to the left within the labeled time range (2 s per line). The black curves correspond to the surface potential profiles at zero gate bias. Linear offsets were applied in subsequent curves for clarity. Only the surface potential data on the QD monolayer regions are shown (the data on the oxide regions were removed), resulting in gaps in the data lines. (c) Voltage drop vs time at the drain contact shown in (b). Red line is the exponential fit.

Besides the current and surface potential transients, the transient capacitance distribution were also recorded and shown in Figure 7.8. We can see that the capacitance is nearly the same everywhere in the channel at any given time, for both hole and electron transport, confirming that the transport of both carriers is Ohmic with uniform mobile carrier density in the channel. The average $\partial^2 C/\partial z^2$ in the p-channel decays exponentially with $\tau = 5.3$ s, nearly the same as that of the transport current, further validating the conclusion that current decay is a result of carrier trapping. In the n-channel, the average $\partial^2 C/\partial z^2$ decays also exponentially with $\tau = 14.0$ s, a little larger than that of the electron transport current. This is likely due to the large transient contact resistance that accelerates the transport current decay.

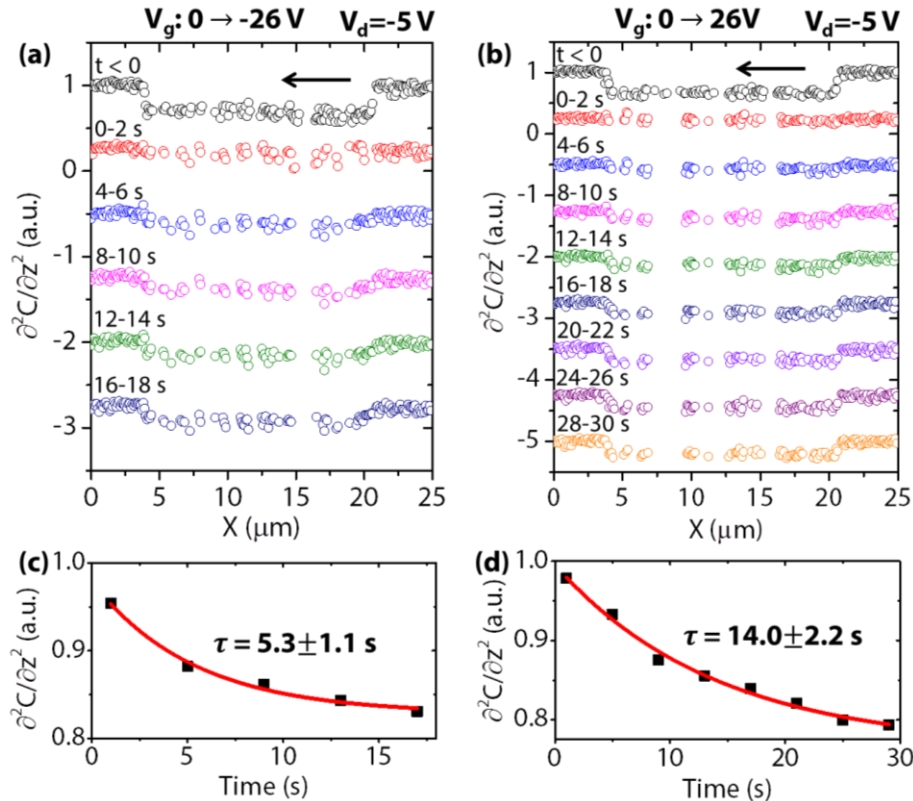


Figure 7.8. Capacitance ($\partial^2 C/\partial z^2$) dynamics at $V_d = -5$ V, following application of a gate bias step of ∓ 26 V. (a) and (b) corresponds to hole and electron dynamics, and each curve corresponds to the full surface potential profile covering the source (left), channel (middle) and drain (right). The tip scanned from the right to the left. (c) and (d) are the average $\partial^2 C/\partial z^2$ in the channel region as a function of time. Black dots are raw data and red lines are exponential fits.

7.6 Discussion and Conclusion

The time constants of the transients are summarized in Table 7.1. We can see that the time scale of the transport current, surface potential, and capacitance are of the same order for holes and for electrons, although the response time for electrons is always $\sim 2-3$ times as large as that of holes. These results agree with previously measured current hysteresis in PbS QD thin film FETs.¹³ Our results on the spatial and time resolved surface potential and capacitance dynamics allow us to

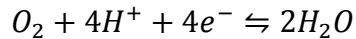
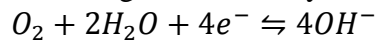
differentiate the injection and transport current which are convoluted in the source-drain current, and directly obtain the total carrier density and mobile carrier density.

Table 7.1. Time constants of various transient parameters.

Physical parameter	Hole response time (s)	Electron response time (s)
Transport current	5.0	8.7
Surface potential (@ $V_d=0$)	2.8	11.0
$\partial^2 C / \partial z^2$ (@ $V_d=0$)	3.7	9.5
$\partial^2 C / \partial z^2$ (@ $V_d=-5$ V)	5.3	14.0
ΔV at injection electrode (@ $V_d=-5$ V)	N/A	11.6
Contact resistance (@ $V_d=-5$ V)	N/A	Constant

We found that the surface potential and capacitance gradually return to their original value after setting the gate bias back to zero, revealing that the trapping behavior is reversible. These reversible trapping and detrapping behavior have been observed in many disordered semiconductor systems, such as organic semiconductors, amorphous Si, and metal oxide films.¹⁹⁻²³ We thus propose that there can be similar mechanisms governing the hysteresis behavior in different materials. In our QD system, the correlation of surface potential and capacitance transients reveals that electrons/holes are initially injected into the conductive IGS/ $1S_h$ states, and subsequently are gradually trapped into lower energy states. If these trapping states are static electronic defects, they have to lie in the ~ 0.2 eV gap between the IGS and $1S_h$ states. These shallow states (~ 0.1 eV from band edge) will likely have a fast charge trapping rate (in the scale of $fs - \mu s$). Thus pure electronic transitions involving static states may not account for the observed transient behavior. This leads us to propose that the trap states are created by some reversible chemical reactions induced by the injected charges. These dynamic traps states therefore are not necessarily located between the IGS and $1S_h$ states. For example, the dynamic electron traps shown in Figure 3c can be lower than the $1S_h$ state. Before charge injection, these traps do not exist; after injection, traps are dynamically created and filled.

One possible origin of these dynamic traps is reactions involving hydroxyl and hydrogen related species that are commonly observed impurities in these disordered systems.¹⁹⁻²³ For example, the following reactions may occur activated by the injected charges:²⁴



These reactions will turn the charge carriers into hydroxyl and hydrogen ions that are much less mobile than electrons, which can be responsible for the observed exponential decay of mobile carrier density in the time scale of seconds. For the PbS QD systems, it has been shown before that OH^- and O_2 are usually present on the QD surface.^{12,25} Therefore, the above reactions are likely to occur during charge injection. Since the $1S_h$ states are more delocalized than the IGS (induced by local defects), it is reasonable that holes in the $1S_h$ states are more easily captured by surface impurities, resulting in faster reactions compared to electrons in the IGS.

To check the validity of the proposed mechanism, we performed control measurements of current transients in an environment with higher humidity and oxygen level, and found that the

time constants are much smaller (Figure 7.9). This supports our conclusion, since higher H₂O and O₂ concentration on the QD surface is expected to induce a higher charge capture rate. Moreover, we found that these changes are reversible as long as the exposure time to higher humidity environment is short.

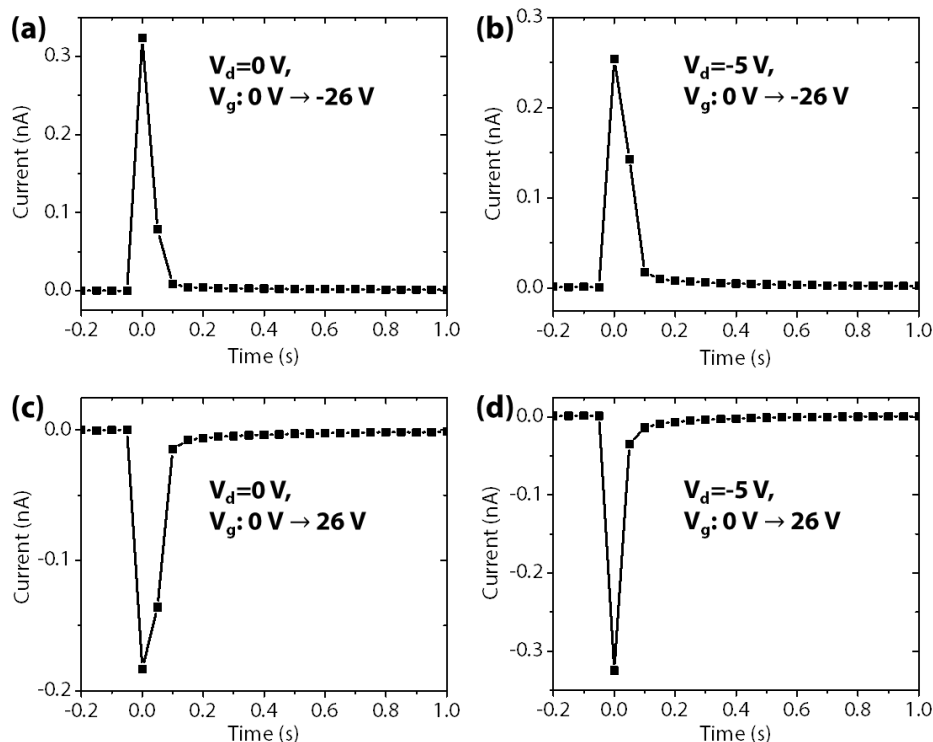


Figure 7.9. Current transients measured while keeping the relative humidity of the sample chamber at ~5%, after decreasing the N₂ purging rate and increasing the size of the gas outlet. Drain bias was fixed at 0 V (a, c) or -5 V (b, d) while a gate bias step from 0 V to ± 26 V (as labeled) was applied. In all the curves, current decays in ~ 0.1 s, limited by the filter bandwidth (10 Hz) of the current amplifier, which is required in order to measure the current accurately. The actual time constant of injection current decay is thus less than 0.1 s. The transport current either decays very fast (< 0.1 s), or has a negligible initial value ($< \sim 10$ pA). The humid environment was kept for less than 30 s when each measurement was performed, after which the chamber was purged with N₂ to reach $< 0.5\%$ relative humidity in a few seconds. The current transients were recovered (same as those shown in Figure 7.4 and Figure 7.6) when measured again in stable dry N₂ atmosphere, revealing that the QDs were chemically intact after exposing to the small amount of humid air.

Additionally, we measured the drain current – drain bias curves with a closed-loop scan in inert atmosphere, while the gate bias was set to zero (Figure 7.10). A hysteresis loop was observed, indicating that charge injection induces a reversible change in the film resistance. The results resemble that of cyclic voltammetry which is a good indication of the occurrence of electrochemical charging/discharging processes. Such hysteresis behavior was also reported in scanning tunneling spectroscopy results on WS₂ nanoparticles,²⁶ where the hysteresis in tunneling current was also explained in terms of electrochemical processes. These results are in support of our proposed dynamic, electrochemical trapping mechanism.

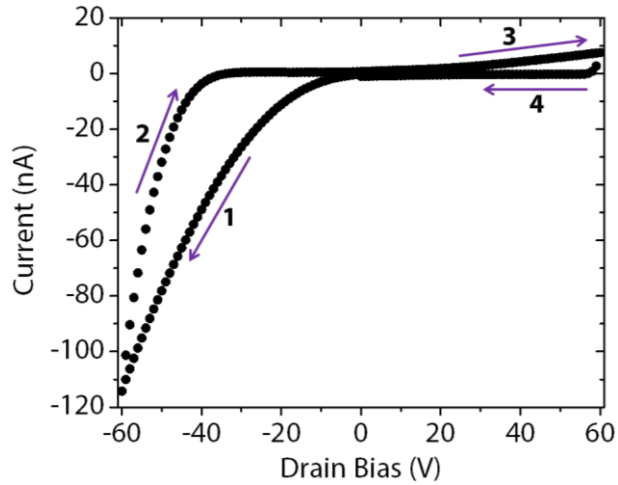


Figure 7.10. Drain current (I_d) – drain bias (V_d) curve with gate bias $V_g=0$. The channel area in this device is $10 \mu\text{m} \times 1 \text{mm}$, where the smaller channel length ($10 \mu\text{m}$) results in a higher lateral electric field at a certain V_d . The V_d scan starts from zero and follows the sequence 1–4 as labeled. The scan rate is 22 V/s.

Although we cannot completely rule out other possibilities responsible for the hysteresis in QD FETs, such as surface structural rearrangements²⁷ and ligand diffusion,²⁸ our first observation of the surface potential and capacitance dynamics in QD systems allows us to directly determine the decay of carrier density and identify the dynamic trapping mechanism. In terms of the effect of the gate dielectric on the hysteresis behavior, we do not expect the SiO_2 to play a role in the observed transients. It has been previously observed that charge trapping on the unpassivated SiO_2 surface occurs in the scale of hours upon the application of a gate bias,²³ which is also confirmed by our own measurements (not shown here). OTS passivation removes most of the SiO_2 surface traps,²³ so that longer hysteresis is expected. Moreover, previous measurements of the PbS QD FETs with different gate dielectric materials revealed that the transient current decay is independent of the choice of dielectric.¹³ Therefore our measured transient phenomena are due to the intrinsic properties of PbS QDs.

In conclusion, we found that charge carriers are dynamically trapped in the scale of seconds upon injection into PbS quantum dot films, which are likely associated with reversible chemical reactions possibly involving hydrogen and oxygen containing species. These traps, though detrimental to field effect transistors, may find applications in photoconductors where carrier trapping can lead to higher lifetime and photoconductive gain.^{2,11} Long-lived traps can also be utilized for memory devices.²⁹ By controlling the surface chemistry of QDs, we can potentially manipulate these dynamics to achieve desirable device performances.

References

1. Talapin, D. V.; Murray, C. B. *Science* **2005**, *310*, 86–89.
2. Konstantatos, G.; Sargent, E. H. *Nature Nanotech.* **2010**, *5*, 391–400.

3. Chuang, C.-H. M.; Brown, P. R.; Bulović, V.; Bawendi, M. G. *Nature Mater.* **2014**, *13*, 796–801.
4. Kim, D. K.; Lai, Y. M.; Diroll, B. T.; Murray, C. B.; Kagan, C. R. *Nat. Commun.* **2012**, *3*, 1216.
5. Zhitomirsky, D.; Voznyy, O.; Levina, L.; Hoogland, S.; Kemp, K. W.; Ip, A. H.; Thon, S. M.; Sargent, E. H. *Nat. Commun.* **2014**, *5*, 3803.
6. Wolkin, M. V.; Jorne, J.; Fauchet, P. M.; Allan, G.; Delerue, C. *Phys. Rev. Lett.* **1999**, *82*, 197–200.
7. Nagpal, P.; Klimov, V. I. *Nat. Commun.* **2011**, *2*, 486.
8. Califano, M.; Franceschetti, A.; Zunger, A. *Nano Lett.* **2005**, *5*, 2360–2364.
9. Cordones, A. A.; Scheele, M.; Alivisatos, A. P.; Leone, S. R. *J. Am. Chem. Soc.* **2012**, *134*, 18366–18373.
10. Shimizu, K. T.; Neuhauser, R. G.; Leatherdale, C. A.; Empedocles, S. A.; Woo, W. K.; Bawendi, M. G. *Phys. Rev. B* **2001**, *63*, 205316–205320.
11. Konstantatos, G.; Badioli, M.; Gaudreau, L.; Osmond, J.; Bernechea, M.; de Arquer, F. P. G.; Gatti, F.; Koppens, F. H. L. *Nature Nanotech.* **2012**, *7*, 363–368.
12. Zhang, Y.; Zherebetsky, D.; Bronstein, N. D.; Barja, S.; Lichtenstein, L.; Schuppisser, D.; Wang, L.-W.; Alivisatos, A. P.; Salmeron, M. *Nano Lett.* **2015**, *15*, 3249–3253.
13. Osedach, T. P.; Zhao, N.; Andrew, T. L.; Brown, P. R.; Wanger, D. D.; Strasfeld, D. B.; Chang, L.; Bawendi, M. G.; Bulović, V. *ACS Nano* **2012**, *6*, 3121–3127.
14. Ip, A. H.; Thon, S. M.; Hoogland, S.; Voznyy, O.; Zhitomirsky, D.; Debnath, R.; Levina, L.; Rollny, L. R.; Carey, G. H.; Fischer, A.; Kemp, K. W.; Kramer, I. J.; Ning, Z. J.; Labelle, A. J.; Chou, K. W.; Amassian, A.; Sargent, E. H. *Nature Nanotech.* **2012**, *7*, 577–582.
15. Luther, J. M.; Law, M.; Song, Q.; Perkins, C. L.; Beard, M. C.; Nozik, A. J. *ACS Nano* **2008**, *2*, 271–280.
16. Liu, Y.; Gibbs, M.; Puthussery, J.; Gaik, S.; Ihly, R.; Hillhouse, H. W.; Law, M. *Nano Lett.* **2010**, *10*, 1960–1969.
17. Zhang, Y.; Ziegler, D.; Salmeron, M. *ACS Nano* **2013**, *7*, 8258–8265.
18. Silveira W. R.; Marohn, J. A. *Phys. Rev. Lett.* **2004**, *93*, 116104.
19. Lang, D. V.; Chi, X.; Siegrist, T.; Sargent, A. M.; Ramirez, A. P. *Phys. Rev. Lett.* **2004**, *93*, 076601.
20. Gupta, D.; Yoo, S.; Lee, C.; Hong, Y. *IEEE Trans. Electron Devices* **2011**, *58*, 1995–2002.
21. Deane, S. C.; Wehrspohn, R. B.; Powell, M. J. *Phys. Rev. B* **1998**, *58*, 12625–12628.
22. Nicolai, H. T.; Kuik, M.; Wetzelaer, G. A. H.; de Boer, B.; Campbell, C.; Risko, C.; Brédas, J. L.; Blom, P. W. M. *Nature Mater.* **2012**, *11*, 882–887.
23. Chua, L. L.; Zaumseil, J.; Chang, J. F.; Ou, E. C. W.; Ho, P. K. H.; Sirringhaus, H.; Friend, R. H. *Nature* **2005**, *434*, 194–199.
24. Chakrapani, V.; Angus, J. C.; Anderson, A. B.; Wolter, S. D.; Stoner, B. R.; Sumanasekera, G. U. *Science* **2007**, *318*, 1424–1430.
25. Zherebetsky, D.; Scheele, M.; Zhang, Y.; Bronstein, N.; Thompson, C.; Britt, D.; Salmeron, M.; Alivisatos, P.; Wang, L.-W. *Science* **2014**, *344*, 1380–1384.
26. Azulay, D.; Kopnov, F.; Tenne, R.; Balberg, I.; Millo, O. *Nano Lett.* **2006**, *6*, 760–764.
27. Voznyy, O.; Thon, S. M.; Ip, A. H.; Sargent, E. H. *J. Phys. Chem. Lett.* **2013**, *4*, 987–992.
28. Voznyy, O. *J. Phys. Chem. C* **2011**, *115*, 15927–15932.

29. Busche, C.; Vilà-Nadal, L.; Yan, J.; Miras, H. N.; Long, D.-L.; Georgiev, V. P.; Asenov, A.; Pedersen, R. H.; Gadegaard, N.; Mirza, M. M.; Paul, D. J.; Poblet, J. M.; Cronin, L. *Nature* **2014**, *515*, 545–549.

Chapter 8: Ultrasensitive Photodetectors Harnessing Defect Conduction

Reproduced in part and adapted from a manuscript in preparation. Only a brief summary is presented.

8.1 Abstract

Following the discoveries of defect-assisted electronic transport and charge percolation phenomena, we are now working on engineering defects to tune carrier percolation pathways, with the goal of making high sensitivity photodetectors. It is known that high-gain photoconductors operate based on the mechanism of trapping of one-type of carriers (p or n) and transporting the other via high mobility pathways¹. Therefore, it is desirable to have a thin film consisting of spatially connected p-n junctions, where one type of junctions form topologically closed domains and the other form connected percolation domains throughout the film. In these films, photoexcited electrons and holes separate instantaneously assisted by the local built-in electric field, with one type of carriers trapped in the closed domains, and the other transported via connected percolation pathways. This is the design principle for bottom-up fabrication of a CdTe photoconductor with record-breaking photoconductive gain.

8.2 Device Fabrication, Operation Mechanism, and Performance

Using bottom up solution processing, we fabricated CdTe polycrystalline films with controlled grain size (5-200 nm) by sintering CdTe nanocrystals. As shown in the schematic diagram (Figure 8.1), we begin with CdTe nanocrystals capped with Cl ligands in toluene solution. We spin-coat the nanocrystals on a substrate, and anneal at 350 °C for 30 s – 5 min. The nanocrystals sinter and form a polycrystalline film, with Cl-rich grain boundaries as confirmed by nano-Auger measurements.

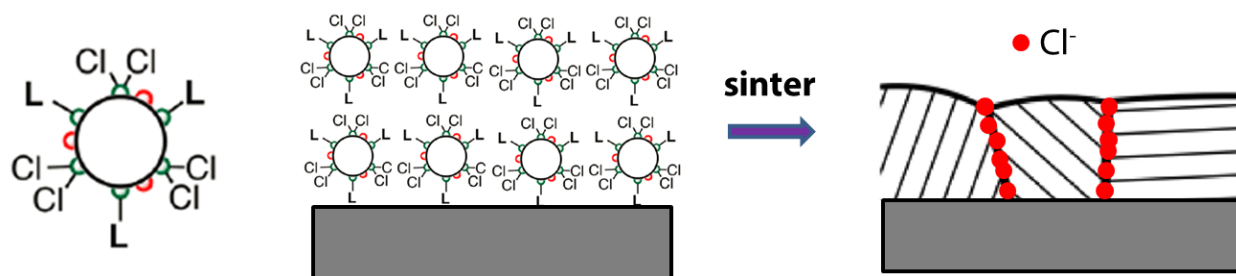


Figure 8.1. Bottom-up solution-processed fabrication of CdTe polycrystalline film. Part of the figure is adapted with permission from *ACS Nano*, **2014**, *8* (7), pp 7513–7521. Copyright © 2014, American Chemical Society.

As revealed by KPFM measurements, the grain bulk is nearly intrinsic with the Fermi level near the mid-gap (band gap is ~ 1.45 eV), while the grain boundaries are heavily n-doped with Fermi level close to the conduction band edge. Moreover the grain boundary is conductive, as revealed by Conductive AFM measurements. Therefore we have mini p-n junctions in the film with conductive grain boundaries forming percolation pathways connecting the electrodes (Indium was used as the n-type contact material). As shown in Figure 8.2, when light (with wavelength

below ~ 850 nm, the bandgap energy) is incident on the biased photodetector, electron hole pairs are created. Holes remain electrostatically trapped in the grain interior, while electrons percolate via the grain boundaries reaching the electrodes and get collected. Via FET measurements we determined an electron mobility of ~ 5 cm²/Vs. Time resolved photocurrent measurements revealed a photocarrier lifetime ranging from ~ 10 ms to ~ 10 s, depending on the incident photon flux (higher flux results in shorter lifetime). With both high mobility and ultralong lifetime, we expect an ultrahigh gain photoconductive detector.

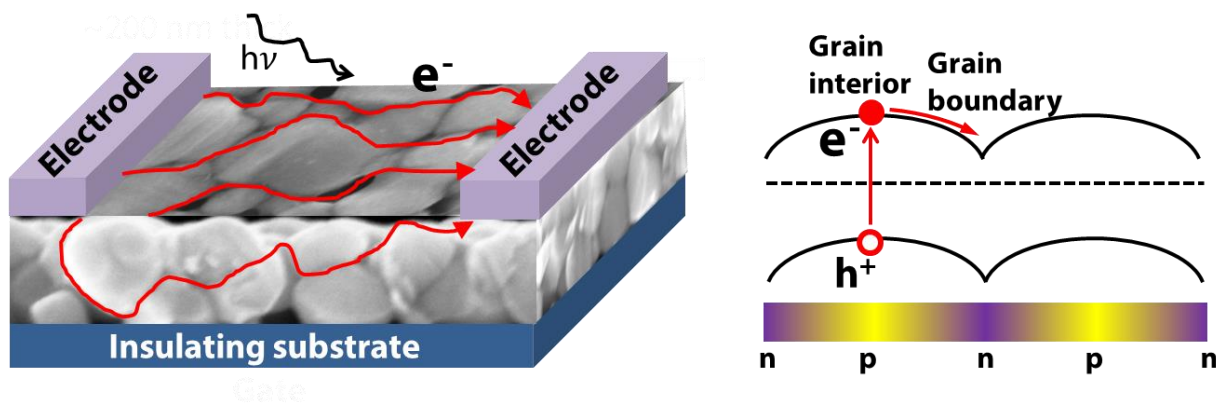


Figure 8.2. Device operation mechanism.

The photoconductive gain we measured is shown in Figure 8.3. We can see that the external gain (number of carriers collected / number of photons incident) depends on the light intensity, likely due to a series of trapping events. i.e. shallow hole traps result in short lifetime and low gain, while deep traps (dominant under low-light) results in longer lifetime and thus higher gain. At low light ($\sim 10^{-9} - 10^{-8}$ mW/cm²), we obtained external gain $\sim 10^{10}$, which is the highest gain in all types of photoconductors, as far as we know.

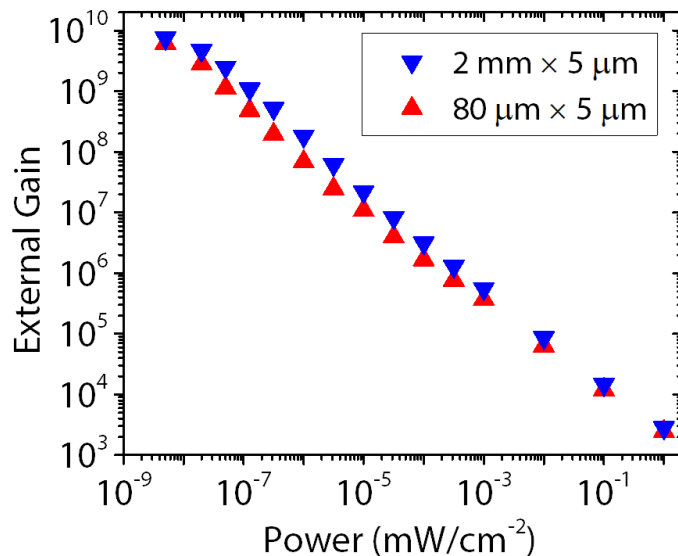


Figure 8.3. Device performance: external photoconductive gain VS incident photon power, measured at 500 nm.

We expect the device to have promising applications in detectors that requires high sensitivity and are tolerant of low speed, such as night-vision, UV smoke detector, X-ray detector, and high energy particle detector.

References

1. G. Konstantatos and E. H. Sargent, *Nat. Nanotechnol.* **5**, 391 (2010).

Chapter 9: Summary and Outlook

We have performed systematic experimental and theoretical studies of the atomic scale surface structure and electronic defects of nanoscale semiconductors, with a focus on colloidal quantum dots. We further found that random distribution of defects generally induce heterogeneity in the energy landscape of disordered semiconductor systems, by studying a model system of artificial quantum dot solid. Counterintuitively, certain defects themselves can assist charge transport, paving the way for high-mobility percolative transport in heterogeneous artificial solids. We expect the discovered defect physics, percolation transport phenomena and the invented ultrasensitive photodetectors to have significant impacts on both the fundamental understanding of nanoscale semiconductors and their large-area device applications. More importantly, we believe that the experimental methodology of combing microscopic/mesoscopic electronic imaging with device properties is generally powerful not only to reveal the internal working mechanisms of electronic/optoelectronic devices, but also to actually guide the design of better-performing devices. We can envision two ways of microscopic approach to the science and technology dealing with the behavior of electrons in materials.

First of all, we need to acknowledge that many devices do need to be “perfect”, where the best performance typically requires homogeneous, crystalline, and defect-free materials. Examples include most of the solar cells, photodiode detectors, high-mobility transistors, *etc.* In these devices, it is desirable to identify the microscopic nature of unintentional defects and electronic heterogeneities, and then eliminate these imperfections to make better devices. As an example, in Chapter 5 using scanning probe based microscopy and spectroscopy techniques we discovered that the origin of defect states (or in-gap states) in PbS quantum dots is molecular oxygen. We further found that by performing hydrazine treatment (as a reducing agent) we can eliminate O₂ impurities and make intrinsic quantum dots with no deep in-gap states. These intrinsic QDs are expected to have low photocarrier recombination rate, and are thus promising for high efficiency solar cells and photodiodes. Our preliminary results already demonstrated that hydrazine is beneficial for device efficiency, and a future direction is to make a PIN junction solar cell where the hydrazine treated QDs can act as the thick intrinsic layer that may enable long carrier diffusion length.

On the other hand, as we have demonstrated, in certain cases fine-tuned electronic heterogeneity can enable novel, high efficiency devices. Here obviously microscopic electronic imaging is essential to the characterization and control of the degree of heterogeneity. In optoelectronics, besides the high-gain photoconductors presented in Chapter 8, we can also imagine a heterogeneous semiconductor with mini p-n junctions that can achieve high electroluminescence and/or photoluminescence, and even high optical gain for laser applications. We may also go beyond optoelectronics, and reach out to other electron-based materials and devices. For example, in thermoelectronics we can envision a heterogeneous system where electronic transport and thermal transport take place via different pathways, and thus high electrical conductivity and low thermal conductivity can be achieved simultaneously, enhancing the thermoelectric figure of merit; in spintronics we can conceive a disordered system with a mixture of nanoscale nonmagnetic and ferromagnetic domains, where multiple spin-dependent scattering may collectively enhance the magnetoresistance, beneficial for memory devices.